2012

Investigation of Three-Dimensional Flow Structure on Maneuvering Finite-Span Wings

Turgut Oruc Yilmaz
Lehigh University

INVESTIGATION OF THREE-DIMENSIONAL FLOW STRUCTURE ON MANEUVERING FINITE-SPAN WINGS

by

Turgut Oruc Yilmaz

Presented to the Graduate and Research Committee
of Lehigh University
in Candidacy for the Degree of
Doctor of Philosophy

in
Mechanical Engineering

Lehigh University

January, 2012

Approved and recommended for acceptance as a dissertation in partial fulfillment of the requirements for the degree of Doctor of Philosophy.

_____

Date

_____

Dissertation Advisor

_____

Accepted Date

Committee Members:

_____

Professor D.O. Rockwell

_____

Professor J.Y. Kazakia

_____

Professor A. Oztekin

_____

Professor H.D. Ou-Yang

To My Wife and My Omer,

ACKNOWLEDGMENTS

I would like to express my sincere gratitude and grateful thanks to my research advisor, Prof. Donald Rockwell, for his extensive wisdom, great guidance and encouragement, close support, efforts and distinguished supervision throughout this study. The opportunity to work with one of the best professors in the area of fluid mechanics was a great honour and chance for me.

I would like to extend my gratitude to my committee members and instructors, Prof. Jacob Kazakia, Prof. Alparslan Oztekin, and Prof. Daniel Ou-Yang, for their evaluation of this work, their valuable time and suggestions.

I also want to mention my thanks to Dr. Michael Ol and Dr. Miguel R. Visbal for their collaborative work, and to the Air Force Office of Scientific Research for the financial aid.

I also extend my appreciation to incessant assistance of Mr. Richard Towne and Mr. James Bunderla for their extraordinary craftsmanship. Without their advices and practical solutions to the technical problems, this study could take one decade to be accomplished. I would like to send my special gratitude to Mr. Herman Baader for his valuable supervision in the student machine shop.

I am also very thankful to Mrs. JoAnn Casciano and Mrs. Jennifer R. Smith for their kindness and administrative assistance. Many thanks to my colleagues and friends, Dr. Alis Ekmekci, Dr. Tunc Goruney, Mr. Ozer Akus and his beautiful family, Mr. Cem Alper Ozen, and Mr. Egemen Tinar for their valuable contributions, moral support and friendship.

I owe my heartfelt gratitude and thanks to my parents for their moral support and motivation; my best friend Okan, who was behind me in every step I took.

Last but the most, I am grateful to my beautiful and wonderful wife Esra for her encouragement, support, patience, love and everything, who deserves all the best. And finally, to my son Omer, thanks for making our life more enjoyable. I love you both. It is to them that I dedicate this dissertation.

TABLE OF CONTENTS

Page

LIST OF FIGURES

Page

NOMENCLATURE

AR	Aspect ratio
a	Free parameter defining degree of smoothing
b	Semi span
BL^-	Negative bifurcation line
BL^+	Positive bifurcation line
C	Chord of planform
C/U	Convective time
CCD	Charge-coupled device
d_o	Distance between the object plane and the lens plane
d_i	Distance between the image plane and the lens plane
D_u	Disparity vector
f	Frequency
$f\#$	f-number of the camera
F	Focal point
h	Vertical displacement
h_{max}	Plunge amplitude
$\dot{h}$	Plunge ramp rate
k	Reduced frequency
K	Dimensionless pitch rate
LEV	Leading-edge vortex
MAV	Micro Air Vehicle
M_n	Magnification
N	Nodal point
PIV	Particle Image Velocimetry
Q	Positive second invariant of the velocity gradient tensor
r	Radius
Re	Reynolds number
S	Distance between the camera lens axes
	Saddle point
S_{ij}	Rate-of-strain tensor
SPIV	Stereoscopic Particle Image Velocimetry

t	Time Variable
	Thickness
t'	Time variable
T	Period
U	Free stream velocity
$\underline{V}$	Velocity vectors
w	Spanwise velocity component
x	Coordinate in chordwise direction
x_p	Pitch pivot point
y	Coordinate in surface normal direction
	Coordinate in orthogonal to the direction of the free stream
z	Coordinate in spanwise direction

Greek Symbols

α	Angle of attack
	Tilt angle of the lens plane
	Viewing angle of the camera
$\dot{\alpha}$	Pitch-up ramp rate
α_{max}	Pitch amplitude
α_{eq}	Equivalent angle of attack
α_{eff}	Effective angle of attack
Γ	Circulation
Δ	Displacement
θ	Stereo angle
σ	Standard deviation
Ω_{ij}	Vorticity tensor
Ω	Pitch rate
ω	Vorticity
$\omega_{x'}$	Streamwise projection of vorticity
ω_y	Surface normal vorticity
ω_z	Spanwise vorticity

∇	Vector differential operator

ABSTRACT

The three-dimensional, unsteady flow structure on low aspect ratio wings arising from plunging and pitch-up motions is addressed via a technique of stereoscopic particle image velocimetry (SPIV), which yields characterization of the three-dimensional flow structure. The time evolution of complex vortex systems is interpreted in terms of phase-referenced three-dimensional streamline patterns, volume images of iso-*Q*, stacked contours of surface-normal vorticity and spanwise velocity, and vorticity projections in orthogonal directions. In addition to quantitative imaging, a technique of flow (dye) visualization is employed to reveal the major features of the flow structure.

Unsteady plunging (heaving) of a wing in the form of a flat plate, over a period corresponding to 3.16 convective time scales *C/U*, and at a Reynolds number based on chord of 10,000, can give rise to pronounced axial flow in the small-scale leading-edge vortex during its initial stage of formation. Opposing axial flows along the vortex interact at the plane of symmetry, giving rise to large-scale patterns of streamwise-

oriented vorticity, which can dominate the tip vortices over part of the oscillation cycle.

Pitch-up (linear ramp-like) motion of wings involves flat plates of various configurations. The pitch-up maneuver is from 0° and 45° over a time span corresponding to four convective time scales, at a Reynolds number based on chord of 10,000. Four different configurations of planforms are employed to investigate the onset and development of the three-dimensionality of the flow structure. Dye visualization reveals effects of variation of the dimensionless pitch rate K on the development of the flow structure during the maneuver. Volumes of constant magnitude of the second invariant of the velocity gradient tensor are interpreted in conjunction with three-dimensional streamline patterns and vorticity projections in orthogonal directions.

During the pitch-up motion, the ordered vortical structures are a strong function of wing planform. After attainment of the maximum angle of attack, however, the vortex system has a similar form for extreme configurations of wing planforms. Near the plane of symmetry, a large-scale region of predominantly spanwise vorticity dominates. Away from the plane of symmetry, the flow is dominated by two extensive regions of surface-normal vorticity, i.e., swirl patterns parallel to the wing surface.

Finally, dye visualization is employed to reveal the formation and subsequent evolution of leading-edge vortices and related vortical structures for various configurations of pitching and plunging low aspect ratio plates, including the effects of wing geometry, Reynolds number, pitch-axis location, and ramp rate. All cases of the

rectangular planform involve a leading-edge vortex with pronounced axial flow, which leads to formation of three-dimensional flow structures, culminating in a large vortical structure centered at the plane of symmetry of the wing. Pitch is also compared to plunge, whereby the functional form of the plunging motion provides an equivalent variation of angle of attack with time that matches the pitching motion. At successively increasing values of time, represented by the convective time scale C/U, the three-dimensional patterns of the flow structure are remarkably similar for the pitching and plunging motions. The similarity of these patterns persists, though they are shifted in time, for variation of either the location of the pitching axis or the dimensionless pitch rate.

CHAPTER 1

INTRODUCTION

Investigation of the flight performance and aerodynamic characteristics of natural flyers has been of considerable interest in recent years. A wide range of investigations, reviewed by Sane (2003), Lehmann (2004), Wang (2005), Lentink and Dickinson (2009), and Shyy et al. (2008, 2010), has enhanced our understanding of unsteady aerodynamics of low Reynolds number flows for design and development of micro-aerial vehicles and small unmanned air vehicles. These studies have been motivated by the remarkable flight characteristics of insects and birds, which involve a variety of wing motions. Basic classes of these motions include flapping, revolving (rotating), pitching, plunging (heaving), and combinations of them. The flow structure and evolution of aerodynamic forces on wings undergoing these types of motion have been of major interest in recent years, primarily from a two-dimensional perspective, and substantial insight has been gained. Less attention has been devoted to the three-dimensional aspects, and most such work has focused on the wake structure. The overall aim of the present study is therefore to characterize the three-dimensional flow field along the surface of low-aspect-ratio plates subjected to various pitching and plunging motions.

1.1 Flow Structure on two-dimensional wings subjected to various unsteady motions

Pitching motion of an airfoil to high angle of attack generates a large-scale, leading-edge vortex that is associated with a process known as dynamic stall. This type of nominally two-dimensional vortex formation on a wing of large aspect ratio is described by McCroskey et al. (1976), McCroskey (1982), Carr (1988), and Ohmi et al. (1991), with emphasis on periodic oscillations. Large-scale vortex formation from the leading-edge of a wing and the occurrence of deep stall is not limited to pure pitching motion. It can occur as well for oscillations in plunging and pitching-plunging modes, as described by Ol et al. (2009). Visbal (2010) has computed the instantaneous three-dimensional flow structure associated with transition phenomena during the onset of deep stall arising from plunging motion. Irrespective of the particulars of the motion, an important concept is the phase shift between the motion of the wing and: (i) the onset and development of the large-scale vortex during one part of the oscillation cycle; and (ii) the tendency towards recovery of attached flow during the other part of the cycle. As a consequence, the flow structure and forces on the wing are dependent upon the history of its motion. Figure 1.1 shows the computed phase-averaged spanwise vorticity, and the behavior of the lift-coefficient as a function of time during the plunging cycle of a 2-D airfoil.

Visbal and Shang (1989) computed the flow structure for the case of transient (non-periodic) pitch-up to very high angle of attack, where the motion was terminated. Details of the vortical structures along the airfoil and the associated forces were related to the pitch rate and pitch axis location. Recent advances have focused

primarily on two-dimensional representations of wings undergoing controlled motion, and include the works of Eldredge et al. (2009), Baik et al. (2009, 2011), and Ol et al. (2010). Eldredge et al. (2009) computationally addressed the mechanisms of vortex shedding and force generation arising from pitching motion of a wing in a freestream, with systematic variation of the motion and wing parameters, which were verified with experiments. Baik et al. (2009) experimentally determined the quasi-two-dimensional flow structure, along with the turbulence statistics, on a contoured wing and a flat plate subjected to pitching and plunging motion. Baik et al. (2011) characterized the quasi-two-dimensional flow field and employed a momentum-based analysis to define the unsteady contributions to the overall forces. Ol et al. (2010) provided an overview of facilities, techniques, and findings, with a focus on two-dimensional aspects. The representative investigations described in the foregoing, along with works cited therein, provide a framework for investigating the flow structure and loading on low aspect ratio wings undergoing similar types of motion.

1.2 Flow Structure on low-aspect-ratio wings subjected to various unsteady motions

The flow structure on maneuvering two-dimensional wings has been extensively investigated by using various computational and experimental techniques (Kang et al, 2009), but there are few studies analyzing flow structure over finite-span wings. While the three-dimensional flow around finite span wings having an aspect ratio greater than four can be successfully derived from two-dimensional considerations (Blondeaux et al, 2005), this assumption is inadequate for a thorough understanding of the unsteady aerodynamics associated with low aspect ratio wings

operating at low Reynolds numbers (Kunihiko, 2009). Furthermore, recent computational (Taira and Colonius, 2009a; Visbal, 2011) and experimental (Yilmaz and Rockwell, 2009; Brunton et al, 2008) studies showed that three-dimensional separated flows over maneuvering low-aspect-ratio wings are considerably different from the analogous two-dimensional flows.

Experimental and computational investigations have shown that the flow structure in the wakes of low aspect ratio wings has complex three-dimensional forms, which can be fundamentally different from their two-dimensional counterparts. Qualitative visualization has led to definition of the key features of the near-wake topology. Freymuth (1989) provided an early interpretation of the three-dimensional vortex structure arising from a pitching low-aspect-ratio flat wing. As shown in Figure 1.2, his study showed that the development of the leading-edge vortex is highly three-dimensional in contrast to development of the classical two-dimensional leading-edge vortex. Von Ellenrieder et al. (2003), Parker et al. (2005), and Parker et al. (2007) characterized the topological features of the near wake from airfoils subjected to basic classes of motion. Moreover, Parker et al. (2007) acquired complementary quantitative images of the flow pattern on the plane of symmetry of a plunging-pitching airfoil. For the case of a panel subjected to pitching motion about its leading-edge, Bucholz and Smits (2006) defined the topology in the wake region using a combination of qualitative and quantitative imaging.

Onset and development of the three-dimensional flow structure along the surface of a low aspect ratio planform was addressed recently from both experimental and computational perspectives. Yilmaz and Rockwell (2009) considered unsteady

plunging of a low aspect ratio plate and, via quantitative imaging, related the axial flow in the incipient leading-edge vortex to the eventual interaction of axial flows at the plane of symmetry, followed by development of large-scale patterns of streamwise-oriented vorticity. Visbal (2011) computed this sequence of flow patterns, and developed a model of the three-dimensional flow structure, which involves the evolution of an arch-type vortex. Furthermore, this process involves occurrence of breakdown, as well as total collapse and re-formation, of the wing tip vortices. The computational visualizations of the time evolution of the three-dimensional flow structure are shown in Figure 1.3.

Computations include the works of Blondeaux et al. (2005) and Dong et al. (2006), who characterized the features of the vortical structures and their interaction in the near-wakes of an airfoil and an elliptical planform undergoing periodic motion, thereby providing a basis for comparison with selected features of the foregoing force measurements and visualization studies. Taira and Colonius (2009a, b) computed the wake structure from various configurations of impulsively translated plates and characterized the strong interaction between the tip and trailing-edge vortex systems as shown in Figure 1.4, and Brunton et al. (2008) used the same computational approach to define the wake structure from a pitching plate.

In addition, aspect-ratio and angle of attack have been found to have a large influence on the stability of the wake profile and the force experienced by the body (Taira and Colonius, 2009a). When the aspect ratio of a wing is relative small, the downward flow induced by the tip vortex and the wake vorticity contributes to the attachment of the leading-edge vortex (Birch and Dickonson, 2001). Angle-of-attack

controls the stabilization of tip vortices, and the size of the separated leading-edge vortex (Jian and Ke-Qin, 2004).

A critical feature of the aforementioned investigations is the axial flow within the leading edge vortex during its formation. It is conceptually similar to that observed in other flow configurations. Directly related to the present considerations is the occurrence of axial flow arising in the vortices shed from an oscillating airfoil between two end walls, characterized by Koochesfahani (1989). Cohn and Koochesfahani (1993) demonstrated that not only a solid boundary, but also a slip boundary could generate pronounced axial flow through the vortex. Bohl and Koochesfahani (2004) addressed the interrelationship between axial and swirl velocity, circulation, and peak vorticity of the vortex. In a combined computational-experimental study of the forced transition of a planar wall jet, Visbal et al. (1998) characterized axial flow in nominally spanwise vortices, and demonstrated that remarkably similar axial flows occurred for cases of either wall or free boundaries on either side of the wall jet. It is therefore evident, from this series of investigations, that pronounced axial flow in vortices is an inherent feature of finite aspect ratio configurations, and can serve as the genesis of larger-scale, three-dimensional flow phenomena.

The present investigation represents various generic maneuvers of nature-inspired flight, i.e., pitch-up motion of a wing to high angle of attack, and periodic plunging motion. Very little is understood of the onset and development of the three-dimensional flow structure on a wing of low aspect ratio undergoing these types of maneuvers. Characterization of the vortical patterns in terms of quantitative, volume-based representations can lead to: identification of generic elements, or features, that

extend to other classes of wing motion; and a physical basis for interpretation of the unsteady loading of the wing. The overall objective of the present study is to determine the time evolution of the quantitative flow structure.

1.3 Unresolved Issues

Unsteady three-dimensional flow structure on finite span wings: Although many studies have addressed the aerodynamic forces and flow characteristics in the wake region and along two-dimensional maneuvering wings, there are inadequate quantitative data to characterize the unsteady three-dimensional flow structure on finite span wings. Moreover, no quantitative (experimental) investigations have addressed the detailed time evolution of the unsteady three-dimensional flow structure on maneuvering low-aspect-ratio wings. In order to gain a deep understanding of the physics of the complex three-dimensional flow structure at low Reynolds numbers, advanced quantitative measurement techniques, such as stereoscopic PIV, are required.

***Spanwise axial flow in leading-edge vortices*:** Spanwise axial flow within the leading-edge vortex on a maneuvering finite-span wing, and the associated distortion of the vortex have been suggested in previous investigations using qualitative visualization. But the source of the axial flow and the three-dimensional interaction of spanwise-oriented vortices in the vicinity of the plane of symmetry of the wing have not been investigated quantitatively.

***Effects of kinematic parameters*:** The effects of the kinematic parameters of the wing motion on the flow structure and the aerodynamic forces on two-dimensional wall-to-wall plates and airfoils have been extensively investigated. Corresponding

insight is not available for the three-dimensional flow structure and associated forces on finite span wings. The kinematic parameters should include reduced frequency (or Strouhal number), phase lag between pitching and plunging during combined maneuvers, amplitudes of pitching and plunging motions, hold time at peak pitch, and location of pitch pivot points.

***Effects of wing planform*:** Nearly all recent investigations have focused on rectangular wings with sharp edges. Yet, for the practically important application of insect flight, wings have rounded edges. No investigations have addressed the three-dimensional flow structure on maneuvering wings with systematic variation of tip configuration, such as elliptical, rounded corner or semicircular.

***Equivalence of flow structure on pitching and plunging wings*:** Qualitative (dye) visualization experiments have shown that the flow structure and the evolution of the leading edge vortex on wall to wall (two-dimensional) wings subjected to equivalent pitch and plunge motions are qualitatively very similar. For wings of finite span, the flow structure will be highly three-dimensional, and the issue arises as to whether similarity of the flow structure exists for equivalent pitching and plunging motions.

1.4 Research Objectives

The overall objective of the present study is to characterize the complex unsteady three-dimensional flow structure on various maneuvering finite span wings by employing both qualitative (dye visualization) and quantitative (PIV, SPIV) measurement techniques. Throughout these investigations, the physics of the flow will be quantitatively interpreted in terms of sectional patterns of velocity vectors, velocity

components, streamlines, and vorticity, in conjunction with volume images of phase-averaged patterns of *Q*-criterion, three-dimensional streamlines, and iso-surfaces of vorticity. In addition, investigations will focus on the effects of various prescribed motions of the wing on the time evolution of the flow structure.

More specifically, the objectives of the present investigation are as follows:

Characterization of three-dimensional flow structure on maneuvering finite span wings

In order to gain a deep understanding of timewise development of the complex, unsteady three-dimensional flow patterns, it is necessary to employ whole field, quantitative measurement techniques. The classical two-dimensional PIV method is not capable of recording the out-of-plane velocity component which is a source of unrecoverable error in the measured in-plane components of the velocity field. In order to avoid the errors associated with this problem, a technique of stereoscopic particle image velocimetry (SPIV) will be introduced, thereby allowing global characterization of the flow structure. This approach provides a sequence of instantaneous three-dimensional velocity fields over the area of interest; and results in both in-plane and out-of-plane velocities everywhere on the measurement plane. Moreover, by using the SPIV technique, volume reconstruction of the three-dimensional flowfield is possible from the measurement planes.

Origin of axial flow in leading edge vortices

The results, obtained from previous dye visualization experiments, have detected the presence of spanwise distortion of leading-edge vortices and associated spanwise axial flow within the vortex. This type of flow structure can be one of the

most important consequences of end effects of a finite-span wing plate undergoing plunging and pitching motions. In order to reveal the origin of the axial flow, SPIV experiments will be performed for various types of pitching and plunging motions.

Effect of tip configuration

The effects of different wing tip configurations on the three-dimensional flow structure on maneuvering wings will be investigated via dye visualization and SPIV experiments. In addition to the rectangular wing, four different configurations will be employed in present experiments.

Effect of kinematic parameters

Formation and development of the three-dimensional flow structure on finite span wings depends on the kinematic parameters of the wing motion. The effects of the kinematic parameters on the flow structure will be investigated by performing dye visualization and PIV experiments. These parameters includes reduced frequency (or Strouhal number), phase lag between pitching and plunging during combined maneuvers, amplitudes of pitching and plunging motions, hold time at peak pitch, and location of pitch pivot points. Moreover, previous studies have shown that the flow structure and the evolution of the leading edge vortex on two-dimensional wings subjected to equivalent pitch and plunge motions are qualitatively very similar. It is important to clarify whether this similarity of the flow structure for equivalent pitching and plunging motions still persists on finite span wings. Furthermore, the effect of Reynolds number variation on the flow structure will be investigated via PIV experiments.

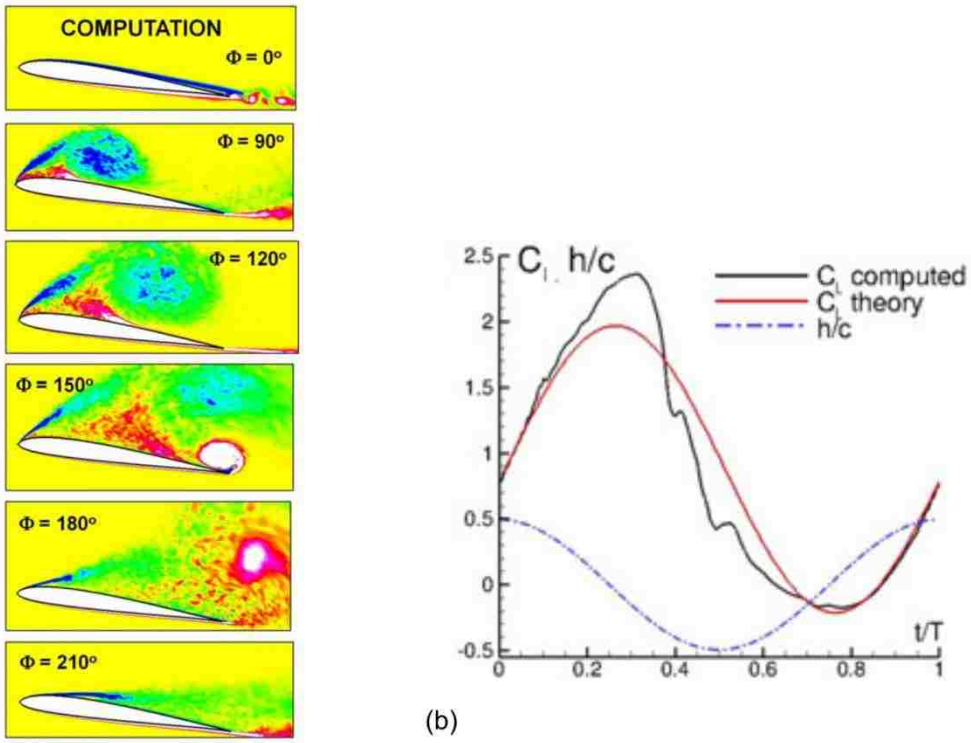

Figure 1.1 : (a) Computed phase-averaged spanwise vorticity at various phases of the plunging motion, (b) lift coefficient variation on a 2-D plate during the plunging cycle (Visbal, 2010).

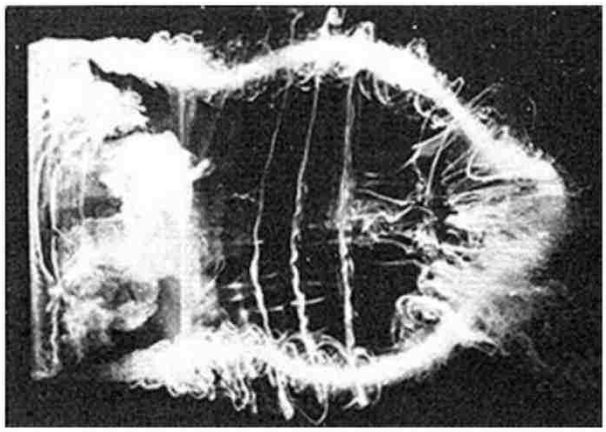

Figure 1.2 : Three-dimensional vortex development on a rectangular low-aspect ratio plate subjected to pitch up maneuver (Freymuth, 1989).

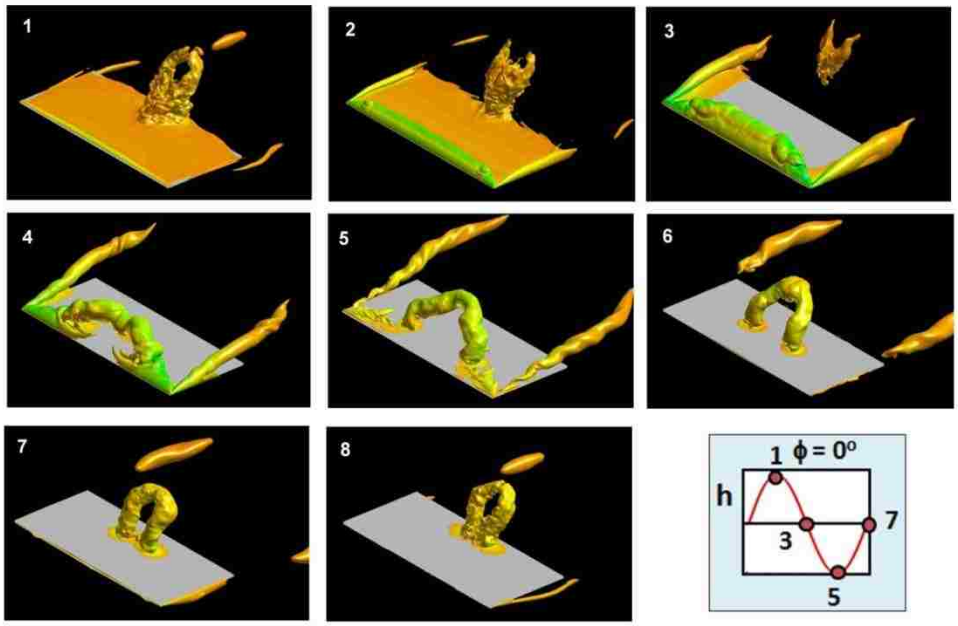

Figure 1.3 : Iso-surface of computed phase-averaged total pressure on a low-aspect-ratio at selected phases plate of the plunging motion (Visbal, 2011).

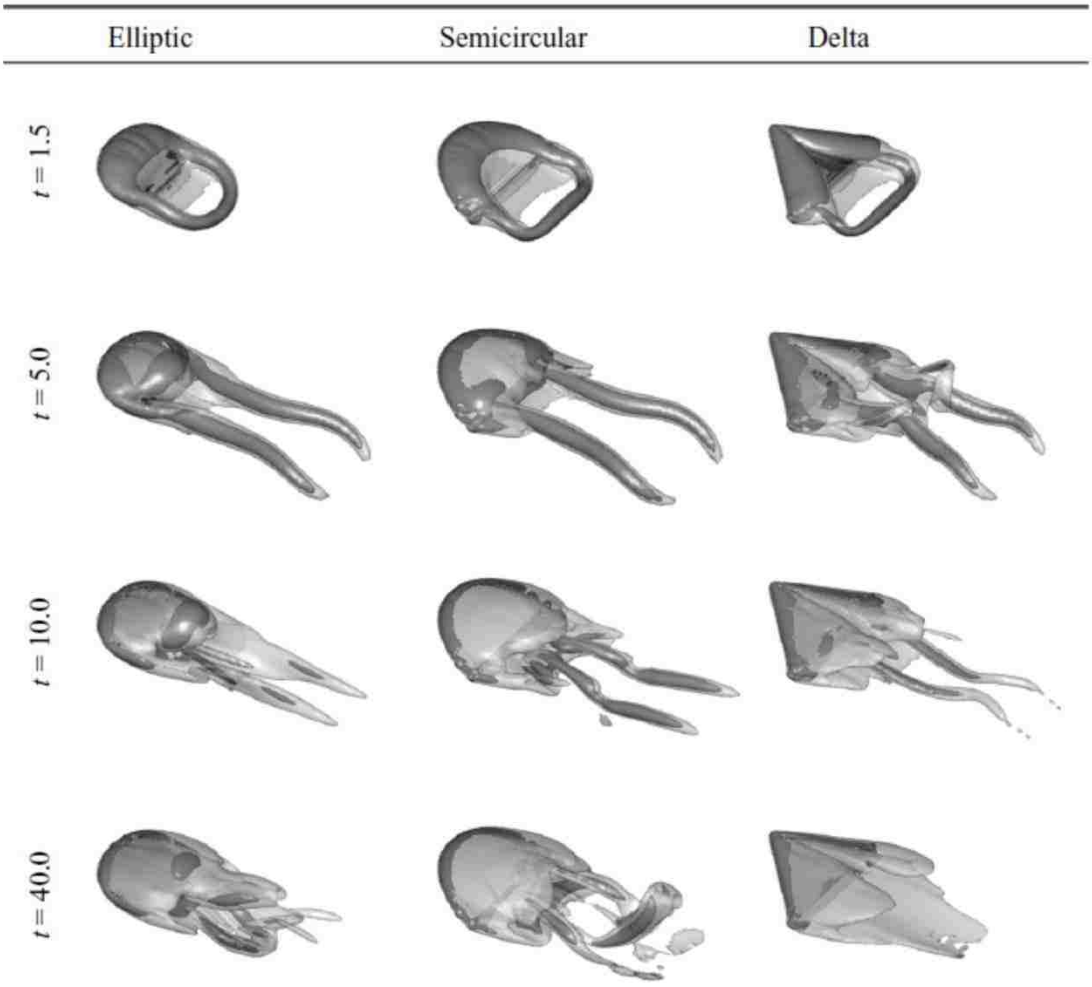

Figure 1.4 : Top-port views of the wake vortices behind different planform geometries at $\alpha = 30^{o}$ and $Re = 300$ with the iso-surface of $||\omega||_2 = 3$ in light grey with vortex cores highlighted by the iso-surface of $Q = 3$ in dark grey (Taira and Colonius, 2009).

CHAPTER 2

EXPERIMENTAL SYSTEM AND TECHNIQUES

Experiments were performed in a large-scale, low-turbulence water channel located in the Fluid Mechanics Laboratory at Lehigh University. These investigations involved characterization of the time evolution of the unsteady three-dimensional flow structurearising from various maneuvers of finite-span wings.

In this chapter, the experimental system and techniques used in this research are described in detail. The water channel system is introduced in section 2.1. The wing planforms, kinematics of motion, and motion control mechanism are described in section 2.2. A detailed explanation of the qualitative and quantitative flow visualization techniques including dye visualization, digital particle image velocimetry (PIV), and stereoscopic particle image velocimetry (SPIV) is given in section 2.3. Section 2.4 provides an explanation of the reconstruction technique for volume images of the flow structure. Section 2.5 describes the method of circulation calculation from experimental data.

2.1 CHANNEL SYSTEM

A schematic of the water channel is shown in Figure 2.1. It has a main test section of 613 mm width, 594 mm depth and 5435 mm length. An arrangement of honeycomb and a sequence of five screens are located at the entrance and the exit to attain low turbulence intensities of approximately 0.3% over the test section. The walls of the channel are composed of Plexiglas which provides optical transparency of the test section. The free-stream velocity in the test section is maintained by pumping the water from the downstream reservoir to the upstream reservoir, then through the honeycomb-screen arrangement and the contraction. The speed of the axial flow pump is controlled by a control unit that adjusts the RPM of the pump motor. During the experiments, the freestream velocity was maintained at 45 mm/sec, 90 mm/sec, and 180 mm/sec and the Reynolds number, *Re*, based on root chord *C* was 5,000, 10,000, and 20,000 respectively. For all experiments, the water temperature was maintained at 24^{o}C.

2.2 TYPES OF WING PLANFORM AND MOTION CONTROL MECHANISM

2.2.1 Types of Wing Planform

In order to investigate the effects of different tip configurations on the three-dimensional flow structure on maneuvering wings, five wing planforms, as shown in Figure 2.2, were employed in the experiments. These planforms include a rectangular flat plate, three plates with different tip configurations, which are rounded at the leading-edge corners with a radius of 10, 20 and 50 percent of the chord length, and an elliptical flat plate. Each wing configuration had the form of thin brass plate, with a chord C = 101.6 mm and a total span $2b$ = 203.2 mm, giving an aspect ratio of 2. The

thickness of the plates was t = 1.59 mm, corresponding to t/C = 0.016. The leading- and trailing edges of the plates, as well as the edges of the tips of the plates, were rounded in such a way that they had a semicircular contour. However, wing configurations with sharp and squared-off (not beveled) edges were also employed in specific experiments.

Each plate was designed to be rigid enough to avoid deflections during the maneuver. In order to measure the detectable deflections of the plate, raw quantitative images were continuously monitored by tracking the line of intersection of the laser sheet with the plate boundary. The deflection was smaller than 0.005b, which was the limiting resolution of the measurement technique.

2.2.2 Kinematics of Motion

Periodic Pure Plunging Motion. The three-dimensional flow structure on the finite-span wing configurations described in the foregoing was investigated for two different types of motion; pitching and plunging. For the case of periodic plunging, two different forms of pure plunging motion were employed; a triangular form, involving successive positive and negative linear ramps, and a sinusoidal form, as illustrated in Figure 2.3a. The effective smoothing at the corners of the triangular function had a duration $\Delta t/T \sim 0.005$, where T is the period of the function. For both types of motion, the frequency and reduced frequency were respectively f = 0.28 Hz and $k = \pi fC/U = 1.0$. The amplitude was $h = 0.25C$, corresponding to a peak-to-peak amplitude of 0.5C. The angle-of-attack of the plate was maintained at $\alpha = 8°$. Three

different values of Reynolds number were employed in these experiments, i.e., *Re* = 5,000, 10,000, and 20,000.

Linear Plunge-up Ramp Motion. In addition to periodical plunging experiments, a plunge-up linear ramp and hold maneuver of the wing, as shown in Figure 2.3b, was employed for the dye visualization experiments. The amplitude of the plunge-up maneuver was $h = 0.5C$, and the angle-of-attack of the plate was $\alpha = 8°$. In terms of dimensionless time scale *C/U*, the plunge-up maneuvers occurred over 1, 2, and 4.0 *C/U*. The corresponding plunge-up ramp rates, $\dot{h}(t)$, were 45 mm/sec, 22.5 mm/sec, and 11.25 mm/sec respectively. For this series of experiments, the freestream velocity was maintained at 90 mm/sec, and the Reynolds number based on root chord *C* was 10,000.

Linear Pitch-up Ramp Motion. The other type of motion considered in the present research was the pitch-up ramp maneuver of the wing from an angle of attack $\alpha = 0°$ to a selected value. One form of the pitch-up maneuver was the linear pitch-up and hold motion from $\alpha = 0°$ to 45°, about the quarter-chord of the wing, $x_p/C = 0.25$, which is represented in Figure 2.3c. The experiments were performed for three different values of time scale 1.0, 2.0, and 4.0 *C*/*U* in order to investigate the pitch rate effect on the evolution of the flowfield. The corresponding pitch-up ramp rates were $\dot{\alpha}$ = 0.696, 0.348, and 0.174 rad/sec, and reduced pitch rates, based on chord *C* were $K = \dot{\alpha}C/2U$ = 0.393, 0.196, and 0.098 respectively. The value of Reynolds number based on root chord *C* was 10,000.

Pitch-up – Hold – Return Motion. The other form of the pitch-up maneuver, represented in Figure 2.3d, was the linear pitch-up of the wing from α = 0 to 45°, hold at the pitch amplitude α_{max} = 45°, and return to α = 0. In these experiments, the pitching axis of the wing was selected at various pivot point locations, i.e. x_p/C = 0 (leading edge), 0.25, and 1.00 (trailing edge). The trapezoidal motion had upward and downward linear ramps, at a non-dimensinal rate of $K = \dot{\alpha}C/2U$ = 0.2. These experiments were performed for two different values of Reynolds number based on root chord, i.e., *Re* = 5,000 and 10,000. For each Reynolds number, the hold time of the wing at the maximum angle of attack was 1.0 *C/U*, corresponding to 2.26 sec for the case of *Re* = 5,000, and 1.13 sec for *Re* = 10,000.

In order to avoid structural excitation during linear ramp maneuvers, including pitch- and plunge-up cases, a ten percent sinusoidal smoothing was employed at the extrema of the motion. The maneuver and the smoothing were calculated according to following equation, which was developed by Eldredge et. al. (2009):

$$G(t) = \ln\left[\frac{\cosh(aU_\infty(t-t_1)/C)\cosh(aU_\infty(t-t_4)/C)}{\cosh(aU_\infty(t-t_2)/C)\cosh(aU_\infty(t-t_3)/C)}\right]$$

where a is a free parameter defining the degree of smoothing, C is the root chord, and the times t_1 through t_4 are defined as:

t_1 = time from the reference time t = 0 until start of the sharp corner of the unsmoothed ramp.

$t_2 = t_1$ + the duration of the pitch or plunge upstroke, until the sharp corner where the hold begins.

$t_3 = t_2$ + the unsmoothed hold time at maximum angle of attack α_{max}, or at maximum plunge amplitude h_{max}.

$t_4 = t_3$ + the unsmoothed pitch or plunge duration the downstroke.

Then the smoothed motion of the wing is defined as:

$$\alpha(t) = \alpha_{\max} \frac{G(t)}{\max(G(t))} \qquad \text{for the pitching maneuver}$$

$$h(t) = h_{\max} \frac{G(t)}{\max(G(t))} \qquad \text{for the plunging maneuver.}$$

Equivalent Pitch and Plunge Motion. In addition to the types of motion described in previous sections, an "equivalent" plunge motion, which matches a trapezoidal linear pitch motion in a quasi-steady sense, was employed to compare the three-dimensional flow structure arising from these maneuvers. For the plunging motion, the functional form of the vertical displacement h of the wing was formulated such that the equivalent angle of attack α_{eq} during plunging corresponded to the geometrical angle of attack α during the pitching motion. The equation giving this relationship is:

$$\arctan\left(\frac{\dot{h}(t)}{U}\right) = \alpha_{eq}(t)$$

Therefore, at a given value of time $t = C/U$ in the schematic of Figure 2.3e, $\alpha_{eq} = \alpha$.

The wing was pitched about $x_p/C = 0.25$ from $\alpha = 0$ to 40° according to the formula given in Eq. 2.2. The reduced pitch rate was $K = \dot{\alpha}C/2U = 0.35$, and the

corresponding amplitude of the equivalent plunge-up maneuver was $h = 0.81C$. These experiments were performed at $Re = 5{,}000$.

2.2.3 Motion Control System

In order to provide different types of motions of the wing described in the previous section, a unique motion control mechanism, was designed in-house. Figure 2.4 shows an overview of this wing motion control mechanism, including a zoomed-in view of the stepping motor-traverse table arrangement, and zoomed-in side and end views of the sting-plate junction. The system includes three stepping motors, designated as A, B, and C in Figure 2.4, which can be simultaneously controlled by a computer.

The plate was held in position by a thin vertical sting with a chain; its maximum width was $0.032b$, and its streamwise length was $0.25C$. The sting was attached at a location corresponding to the mid-span and mid-chord of the plate. In order to ensure that this arrangement was not interfering with the flow along the plate, the sting was attached at quarter-span and midchord, and the flow structure was found indistinguishable from the case where it was attached a mid-span. Pitching motion of the plate was achieved by the chain about the periphery of the sting; it was connected to the stepping motor C at the top of the sting. Depending on the pivot point location, horizontal and vertical traverse tables were simultaneously controlled by the stepping motors A and B. Therefore, an arbitrary streamwise location of the pitch pivot point could be prescribed during the pitch up motion. For the plunging wing experiments, only the vertical traverse and stepping motor B were employed.

With this unique design of the motion control system, different types of motion and various severe maneuvers of the plate were accurately achieved during the experiments.

2.3 *FLOW VISUALIZATION TECHNIQUES*

In the present investigation, the flow structure was visualized using both qualitative and quantitative imaging techniques. In order to qualitatively interpret the flow patterns, a technique of dye marker visualization was employed. A technique of high-image-density particle image velocimetry was employed to characterize the quantitative flow patterns.

2.3.1 Dye Visualization

The aim of the dye visualization experiments was to gain an overall understanding of the flow structure, and to reveal the main characteristics of the flowfield evolution. Due to its easy and fast implementation, the dye visualization technique was used to identify the most critical parameters, which were used in advanced quantitative measurements.

Dye was composed of 35% food coloring and 65% water. It was gravity-fed from a single plastic tube connected to the wing surface, then through multiple channels within the wing. Dye ports of diameter 1 mm were drilled into the leeward side of the wing at various spanwise locations depending on the wing geometry. Side and plan views of the visualized patterns of the flow were recorded simultaneously using two CCD cameras.

2.3.2 Digital Particle Image Velocimetry (DPIV)

A technique of high-image-density particle image velocimetry was employed to characterize the quantitative flow patterns. The overview of the DPIV system and the orientation of the laser sheet, and the camera are shown in Figure 2.5.

A Solo-III double pulsed Nd:YAG laser, having a maximum output of 120 mJ, was mounted on a traverse system under the channel. During the PIV experiments, the laser sheet was oriented orthogonal to the direction of the free stream. By using an array of spherical and cylindrical lens, the laser beam was converted to a laser sheet. The laser sheet had a thickness between 1 mm to 2 mm in the field of view. The pulse rate of the laser system was 29 Hz, which corresponded to acquisition of 14.5 image pairs per second. During the course of the experiments, acquisition of images at various chordwise locations along the chord of the wing required repositioning of the wing in the streamwise direction. The wing was precisely repositioned by the horizontal traverse table described in section 2.2.3.

Images were captured using a CCD camera with an array of 1600 pixels × 1200 pixels. The effective magnification of the camera provided a resolution in the plane of the laser sheet between 4.94 and 5.59 pixels/mm. Processing of the patterns of particle images yielded a maximum of approximately 7,227 velocity vectors within the field of view.

The water was seeded with 12 micron diameter metallic-coated, neutrally-buoyant plastic spheres. The seeding density was sufficiently high, such that more than 15 particle images were typically attained within the interrogation window of 32

pixels × 32 pixels. Moreover, the seeding density of these particles was sufficiently large, such that the high image density criterion was satisfied.

Insight 3G software from TSI was employed in pre-processing, processing and post-processing of images. Processing of the patterns of particle images involved a frame-to-frame cross-correlation technique. A 32 × 32 pixel interrogation window was used, with a 50% overlap. During the interrogation process, the Nyquist criterion was satisfied, and the Hart correlation algorithm was used. The Hart correlation is a direct correlation method that processes only the most significant pixels to improve processing speed. A bilinear peak method was employed, which is the recommended peak method for the Hart correlation. This method works by locating the correlation peak with sub-pixel accuracy, through fitting a set of linear functions to the highest correlation peak pixel and its four nearest neighbors. For the post-processing of the data, the median test method was applied for vector validation and elimination of bad vectors in the image of the flow field. The median test eliminates invalid vectors by comparing the difference between each velocity vector and its local median velocity with a given tolerance. In order to fill the removed data, a recursive filling method was employed. Finally, by using Gaussian low-pass filtering, smoothing was performed after filling the holes. The Gaussian low-pass filter uses a rotationally symmetric kernel of size n (filter size), which was 5x5, and standard deviation σ, which was taken as 0.8. The Tecplot 360 program was used to prepare the final forms of the data showing the patterns of velocity, vorticity, and streamlines. The final layout of the images was prepared by utilizing CorelDraw program.

2.3.3 Stereoscopic Particle Image Velocimetry (SPIV)

Conventional two-dimensional particle image velocimetry (DPIV) is a widely used measurement technique providing only the projection of the velocity vector into a planar region illuminated by a laser light sheet. The classical PIV method is not capable of recording the out-of-plane velocity component, which is a source of unrecoverable error in the measured in-plane components of the velocity field due to the perspective transformation. There are a variety of approaches and three-dimensional techniques of particle image velocimetry capable of recovering all velocity components. One of the most straightforward and widespread methods is stereoscopic PIV (SPIV) which provides sufficient information to obtain all three components of the velocity in the plane illuminated by a laser light sheet, as well as to eliminate the errors in the in-plane components.

SPIV provides a sequence of instantaneous three-dimensional velocity fields over the area of interest. In this technique, two simultaneous, but different, views of the same area of interest are recorded. Each view is individually interrogated by means of a correlation analysis resulting in velocity data. In order to obtain the three-dimensional velocity data, the displacements from each image plane are mapped onto the object plane. Then, they are combined based on a mapping function generated from a 3-D calibration method, and therefore all three components of the velocity are determined.

2.3.3.1 Translation vs. Angular Displacement SPIV systems

There are two primary configurations of SPIV systems: the translation method, and the angular-displacement method (Prasad, 2000), as shown schematically in

Figures 2.6a and 2.6b. In the translation method, both the cameras and the lenses are positioned in such a way that their axes are oriented parallel to each other and orthogonal to the laser sheet, thereby providing uniform magnification and well-focused images over the entire observation area. Because the invariant magnification provides identical spatial resolution between the combined field and the two individual views, the combined vector field over the common image area can be readily obtained by correlating the vector field resulting from each view without additional processing (Prasad and Kirk, 1995). In spite of its simplicity, the translational method has some difficulties and restrictions. One serious difficulty arises from geometric positioning of the cameras. Due to the parallel oriented camera and lens axes, the "common area" viewed by each camera is small. The common area can be increased by increasing the distance between the camera and the lens plane; or by enlarging the field angle θ shown in Figure 2.6a, but there is an upper bound of θ as well as of distance, d_i, between the camera and the lens plane due to the limitations and performance of the lens. While the use of larger field angle increases the sensitivity to the out-of-plane displacement, it causes perspective distortion in the image plane (Prasad, 2000). Another problem in the translation imaging approach arises from a strong decrease in the modulation transfer function (MTF) toward the edges of the field of view causing a blurry image field (Willert, 1997). Moreover, when the translational configuration is used for imaging of a liquid flow, the liquid-air interface causes a change in the refractive index, which is the source of two problems: lack of a planar surface of least confusion, and blurred non-circular particle images caused by radial distortions (Prasad and Kirk, 1995). Most of the shortcomings of the translational method,

including the small size of the common area and the restriction of the upper bound to off-axis angle θ, can be eliminated by introducing the alternative angular displacement method shown in Figure 2.6b.

In the angular displacement method, both the cameras and the lenses are positioned in such a way that their optical axes are no longer parallel to each other and no longer orthogonal to the laser sheet, but make a fixed angle θ with the laser sheet as shown in Figure 2.6b. In contrast to the translational method imposing upper bound restriction on θ due to lens performance, the angular-displacement method offers freedom of increasing the angle θ, which allows greater accuracy in the out-of-plane component (Prasad, 2000). However, non-uniform magnification is not avoidable, which introduces systematic bias errors into the measurement and the locations of the velocity vectors (Soloff et al, 1997). Furthermore, with the angular displacement method, the required depth of field to obtain particle images with good focus is much larger than in the transitional method. For a specific magnification, M_n, the depth of field can be increased by increasing the f-number, f#, which causes a higher random error component in the PIV interrogation (Prasad and Adrian, 1993).

With the increasing of f#, the image sensor of the camera captures a smaller fraction of the light scattered by the particles. The error arising from the use of large f-numbers can be eliminated, if the Scheimpflug criterion is satisfied which requires that the image plane will be additionally tilted with respect to the lens plane by an angle α, where the image plane, lens plane and object plane intersect on a common line (Willert, 1997). The required tilt angle α is given by;

$$\alpha = tan^{-1}\left[\frac{d_i tan\theta}{d_0}\right]$$

The relationship between the view angle θ, and the error in stereoscopic PIV measurements is shown in Figure 2.7 (Alkislar et al, 2000). The minimum error is obtained when the view angle is 45^o. Due to varying magnification, the angular displacement method with the use of Scheimpflug condition yields stronger perspective distortion in the image field, which transforms a square view into a trapezoid, as shown in Figure 2.8. The error analysis and performance evaluation of a Scheimpflug angular displacement system were performed in detail by Zang and Prasad (1997). Their computational error analysis showed that the system accuracy is strongly dependent on the off-axis angle θ. The results also showed that ratio of out-of-plane error to in-plane error (relative error) in the Scheimpflug angular displacement method is smaller compared to the error observed in the translation system. The relative errors arising purely from the interrogation of PIV photograph can be approximated as:

$$\sigma_{\Delta z} \approx \sqrt{2}\left[\frac{d_o}{MS}\right]\sigma_{\Delta X}$$

$$\sigma_{\Delta x} \approx \frac{1}{\sqrt{2}}\left[\frac{1}{M}\right]\sigma_{\Delta X} \qquad \text{(for } x = 0\text{)}$$

$$\sigma_{\Delta y} \approx \frac{1}{\sqrt{2}}\left[\frac{1}{M}\right]\sigma_{\Delta X} \qquad \text{(for } y = 0\text{)}$$

and the relative out-of-plane error yields (Prasad and Adrian, 1993),

$$\frac{\sigma_{\Delta z}}{\sigma_{\Delta x}} = \frac{\sigma_{\Delta z}}{\sigma_{\Delta y}} = 2\frac{d_o}{S} = \frac{1}{tan\theta}$$

where M is the magnification of the camera, S is the distance between the camera lens axes, and d_o is the distance between the object the lens plane..

2.3.3.2 Calibration and Reconstruction of Velocity Field

In order to obtain three-component planar velocity data from distorted images, the data from each image plane is back-projected (mapped) to the object plane, which is called reconstruction. There are two reconstruction methods classified by Prasad (2000); geometric reconstruction and calibration-based reconstruction. Nowadays, the calibration-based method is commonly preferred to the geometric method, because geometric reconstruction has limited accuracy, and higher sensitivity to minor flaws such as camera misalignment, and it requires knowledge of the complete system geometry (Scarano et al, 2005).

However, the calibration-based methods do not require any additional information about the system geometry. There are two distinct calibration-based techniques categorized as 2D and 3D calibration methods (Prasad, 2000). In the 2D calibration method, only the viewing angle of the cameras must be known. Compared to the 2D calibration, the 3D calibration method proposed by Soloff et al (1997) is easier to implement, and does not require knowledge of the system geometry. However, it gives non-uniform and non-isotropic spatial resolution.

One of the most critical drawbacks of SPIV, using the calibration-based method, is the unavoidable misalignment error due to the impossibility of setting the laser sheet exactly in the same position of the calibration plane as shown in Figure 2.9. If this misalignment error is not considered, the following errors exist (Giordano and Astarita, 2009):

1. The trapezoidal images obtained from each camera are back-projected in wrong positions which cause a fictitious additional displacement field.
2. The local viewing angles are miscalculated resulting erroneous evaluation of 3D displacement vector.
3. The 2D vectors used in 3D reconstruction are no longer at the same positions.

If there is a misalignment between calibration and measurement plane, it is possible to compute the disparity map of the misalignment by cross-correlating the de-warped images recorded simultaneously on each camera (Coudert et al, 2001). If the local viewing angle of each camera, designated as α_1 and α_2 in Figure 2.9, is known, the local misalignment can be computed with the following equation by means of regression method;

$$\Delta z = z_{meas} - z_{calib} = \frac{D_u}{tan\alpha_1 + tan\alpha_2}$$

where D_u is the disparity vector.

Giordano and Astarita (2009) proposed a new method which can compute the local viewing angles α_1 and α_2, as well as disparity vector, by correlating two calibration images recorded from different perspectives. The scheme of this procedure is shown in Figure 2.10.

2.3.3.3 SPIV in Liquid Flows

The particle images recorded by a single camera are mostly free of radial distortion. On the other hand, in a stereoscopic arrangement with large off-axis angles, the radial distortions on the particle images can become noticeably large, which result

in an adverse effect on the accuracy of measurements (Prasad, 2000). For an accurate measurement, all sources causing distortion such as inaccurate optical alignment, lens nonlinearity, refraction by optical windows or liquid-air interfaces should be taken into consideration. The liquid-air interface causes two main problems: no planar surface of least confusion, and blurred non-circular particle images caused by radial distortions (Prasad and Kirk, 1995). In order to minimize the radial distortion due to larger off-axis angles and liquid-air interface, a thin-walled liquid prism filled with the same liquid can be attached to test section as shown in Figure 2.11.

Because of the radial distortion due to the liquid-air interface, the colinearity of the object, lens and image planes (the Scheimpflug criterion) cannot yield optimal, well-focused images. In this case, the image plane should be adjusted to catch an optimal focus. Prasad and Kirk (1995) developed a computer model to optimize the location of the image plane such that particle images were obtained in good focus.

In the present SPIV system, the angular displacement configuration was used. A schematic of this configuration is shown in Figure 12. The laser sheet was oriented orthogonal to the direction of the free stream. Two identical CCD cameras were located on each side of the channel. In order to satisfy Scheimpflug condition, the lens plane was tilted with an angle α relative to the image plane. In order to obtain a large, common field of view, the cameras were adjusted with an off-axis angle $\theta = 50^{o}$. Two liquid prisms filled with distilled water were employed, in order to avoid uncertainties arising from mismatch of refractive indexes of air and water. For the calibration of present SPIV system, a dual-plane dual-sided calibration target was used, which yielded 3D calibration of the system. Furthermore, a disparity mapping method was

employed during the calibration process, in order to correct the error arising from misalignment between the calibration target and the measurement plane. For this stereo configuration, the rms residual pixel displacement error generated during the interpolation phase of the stereo reconstruction was calculated as 0.103 pixels. The same pre-processing, processing and post-processing methods of DPIV, described in section 2.3.2, were employed.

Figure 2.13 shows an overview of the experimental components including wing planform, SPIV arrangement, and motion control system employed in the present investigation.

2.4 *VOLUME RECONSTRUCTION*

In order to obtain volumetric representations of the three-dimensional flowfield, a volume reconstruction method was employed. Using the three-dimensional phase-averaged velocities on multiple cross-flow planes, volume images of the flow structure were determined. The plotting and interpolation were performed using the *Tecplot* software package. In order to assess the uncertainty involving in the interpolation and volume construction technique, in-house developed software was used. This software simulates the known theoretical solution for Hill's spherical vortex, as described by Robinson and Rockwell (1993), in a user-defined volume with a specific grid size and number. This approach allows variation of the scale of the three-dimensional domain of vorticity, over the volume of interest. Planar cuts through the known field of vorticity, at arbitrary spacing and orientation, allowed simulation of the acquired experimental data, thereby leading to volume construction of the velocity

and vorticity fields. For the parameters employed in the present investigation, the representative uncertainty of the reconstructed velocity was 0.4%.

2.5 *CALCULATION TECHNIQUE FOR CIRCULATION*

In addition to the characterization of flow patterns, a circulation calculation was performed on selected planes, in order to gain further insight into the distinctive features of the vortical structures in the flowfield. The circulation was computed from the velocity data at a point (*i, j*) according to Stokes theorem, which provides the circulation estimate around the neighboring eight points (Raffel et al, 2007). Stokes theorem defines the relationship between the velocity and the circulation as;

$$\Gamma = \oint \mathbf{U} \cdot \mathrm{d}\mathbf{l} = \int (\nabla \times \mathbf{U}) \cdot \mathrm{d}\mathbf{S}$$

at a point (*i, j*), circulation $\Gamma_{i,j}$ is defined as;

$$\Gamma_{i,j} = \frac{1}{2}\Delta X\left(U_{i-1,j-1} + 2U_{i,j-1} + U_{i+1,j-1}\right)$$

$$+\frac{1}{2}\Delta Y\left(V_{i+1,j-1} + 2V_{i+1,j} + V_{i+1,j+1}\right)$$

$$-\frac{1}{2}\Delta X\left(U_{i+1,j+1} + 2U_{i,j+1} + U_{i-1,j+1}\right)$$

$$-\frac{1}{2}\Delta Y\left(V_{i-1,j+1} + 2V_{i-1,j} + V_{i-1,j-1}\right)$$

The enclosed area that is used for circulation calculations was chosen as a rectangular area which only covers the selected vortical structure.

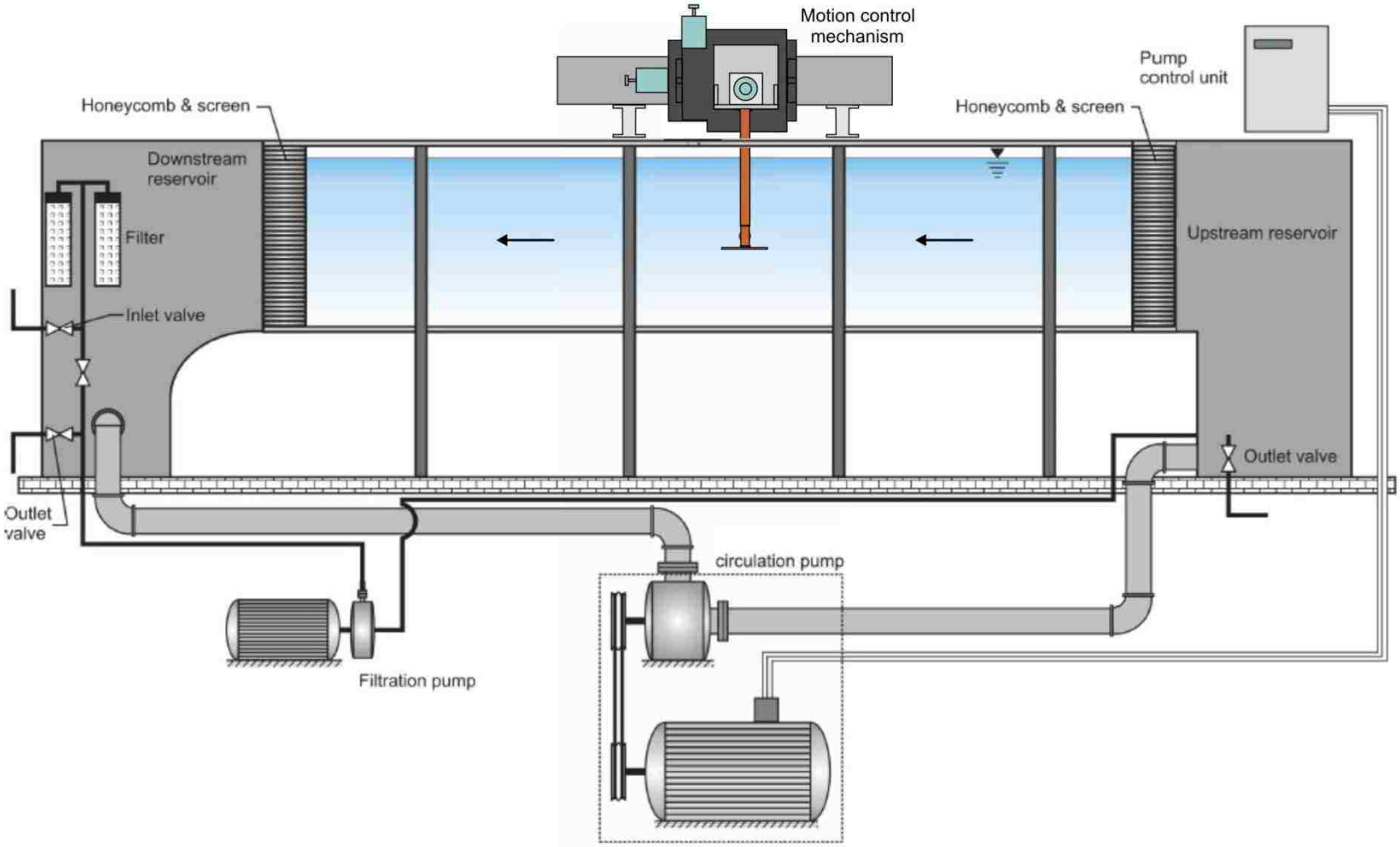

Figure 2.1 : Overview of the recirculating, free-surface water channel facility with the motion control mechanism.

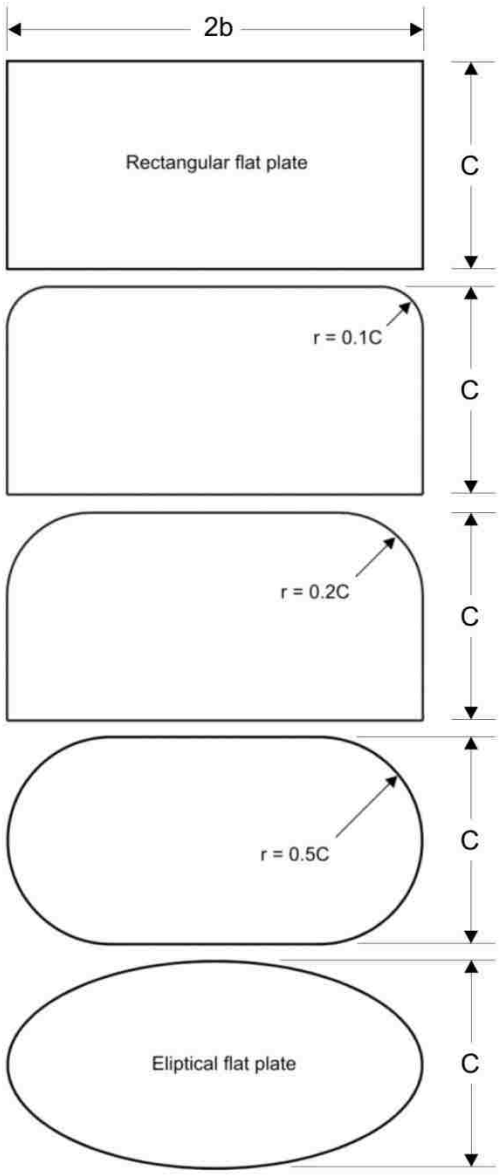

Figure 2.2 : Types of wing configurations

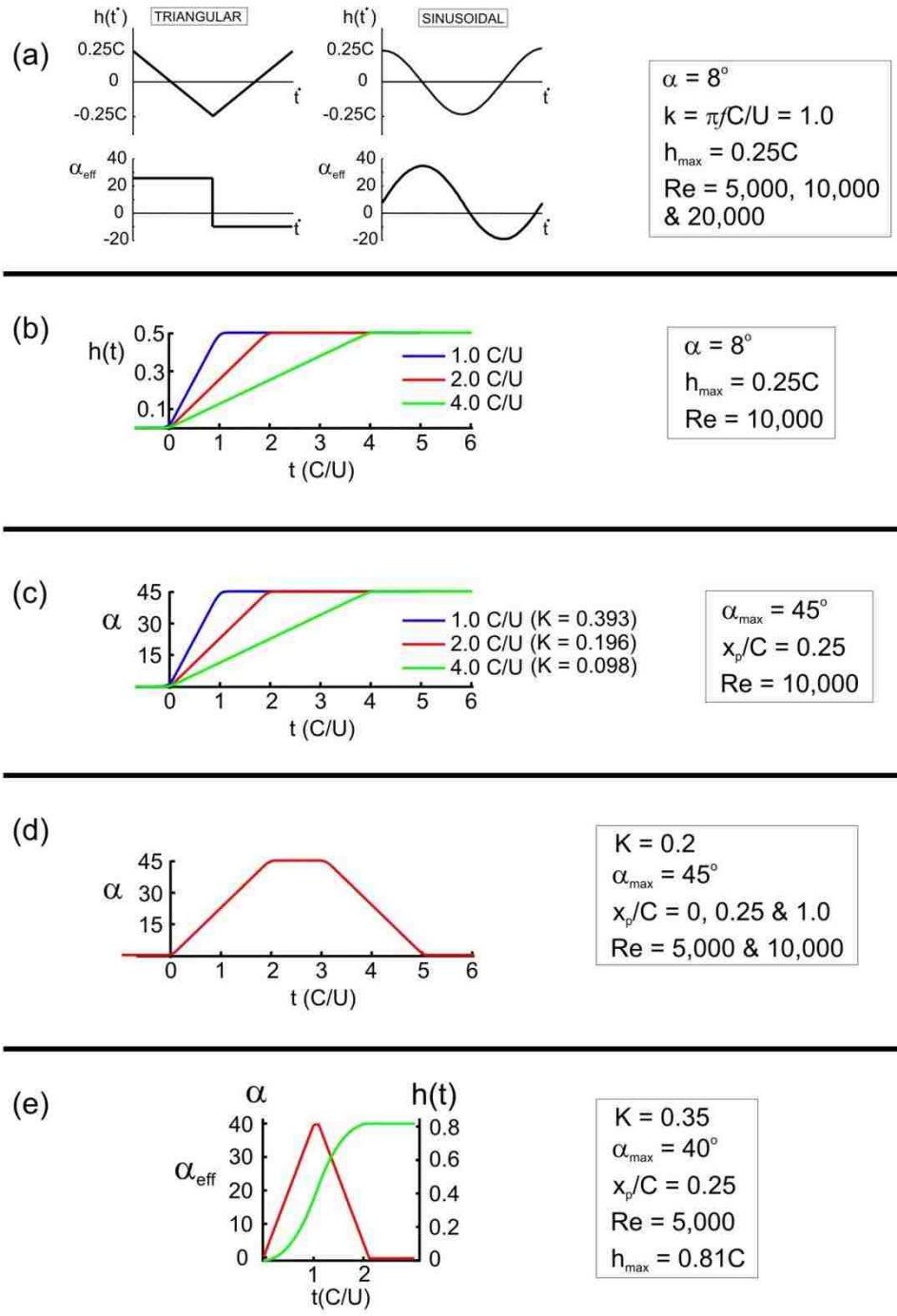

Figure 2.3 : Overview of kinematics of motion; **(a)** periodic pure plunging motion, **(b)** linear plunge-up ramp motion, **(c)** linear pitch-up ramp motion, **(d)** pitch-up - hold - return motion, **(e)** equivalent pitch and plunge motion.

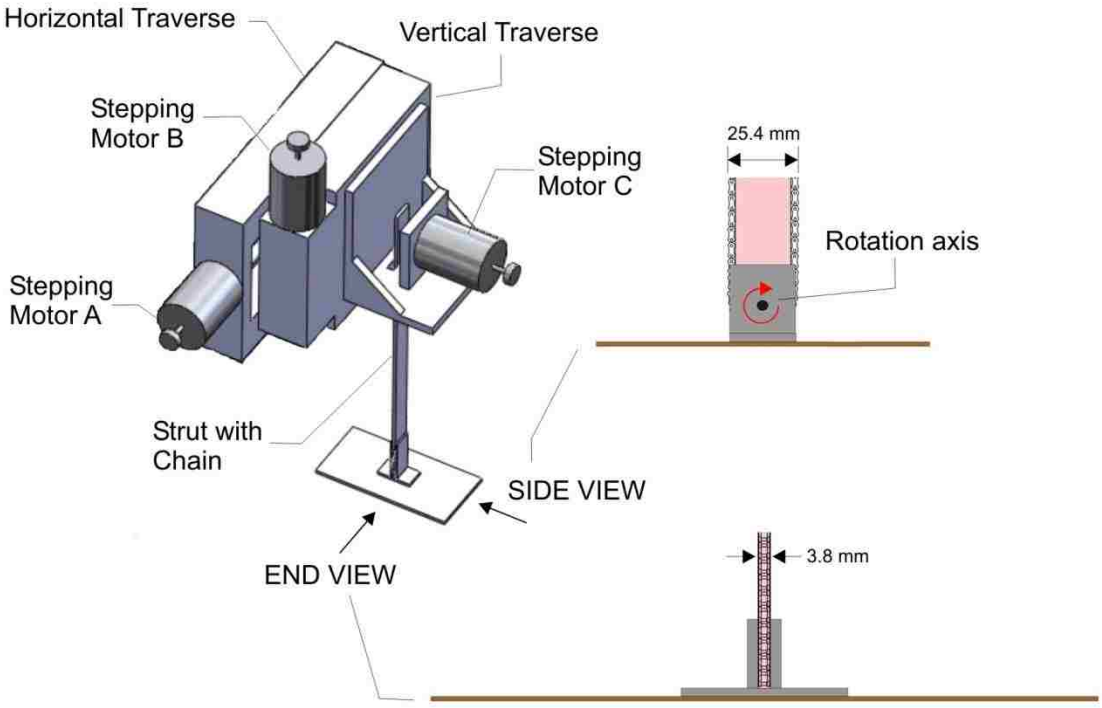

Figure 2.4 : Overview of the wing motion control system.

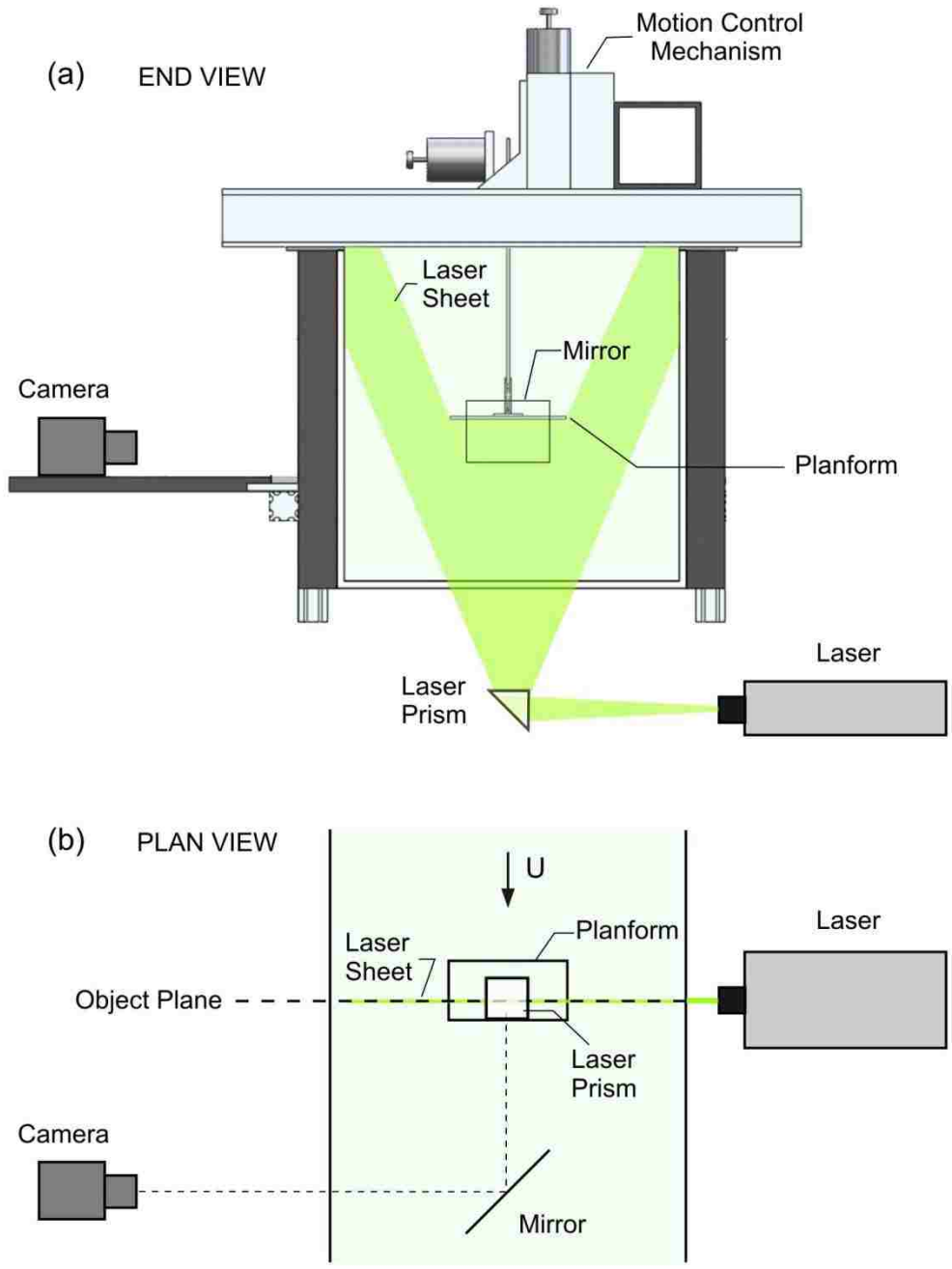

Figure 2.5 : Overview of single camera DPIV system for acquiring images in cross-flow plane. **(a)** End view of the system, **(b)** Plan view of the system.

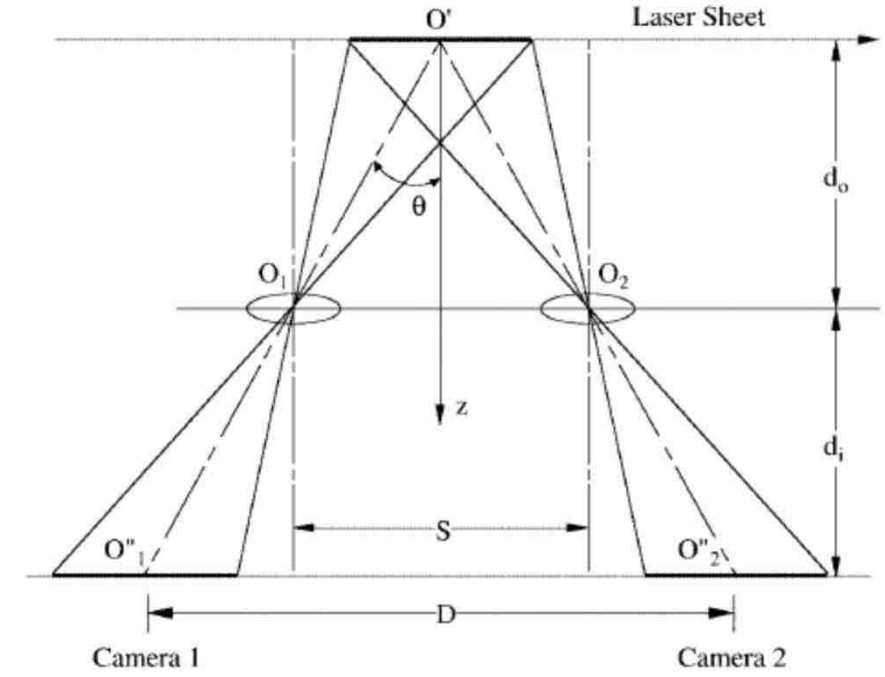

(a) Translation system

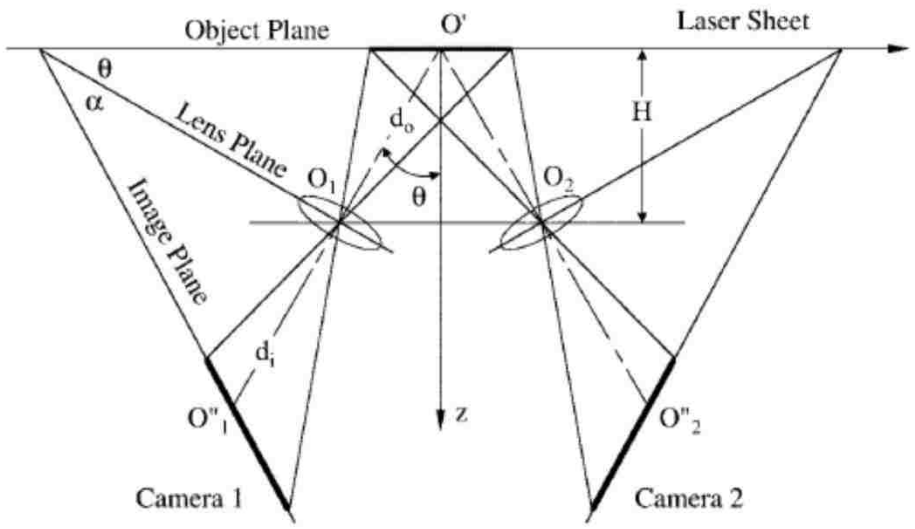

(b) Angular displacement system

Figure 2.6 : Two primary configurations for SPIV systems: **(a)** Translation method, **(b)** Angular displacement method (Prasad, 2000).

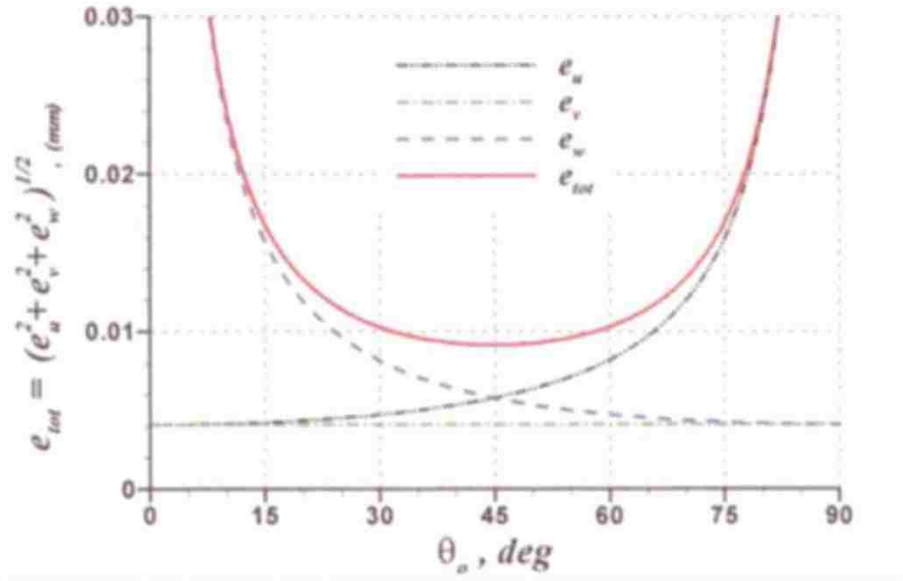

Figure 2.7 : Error analysis for stereoscopic PIV with Scheimpflug condition (Alkislar et al, 2000).

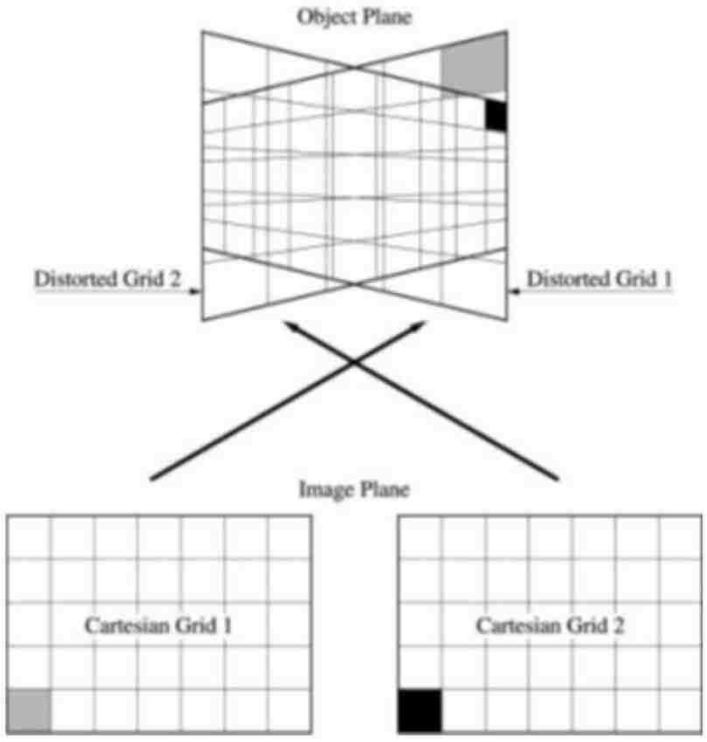

Figure 2.8 : Opposite stretching of a cartesian grid on the image plane (Prasad, 2000).

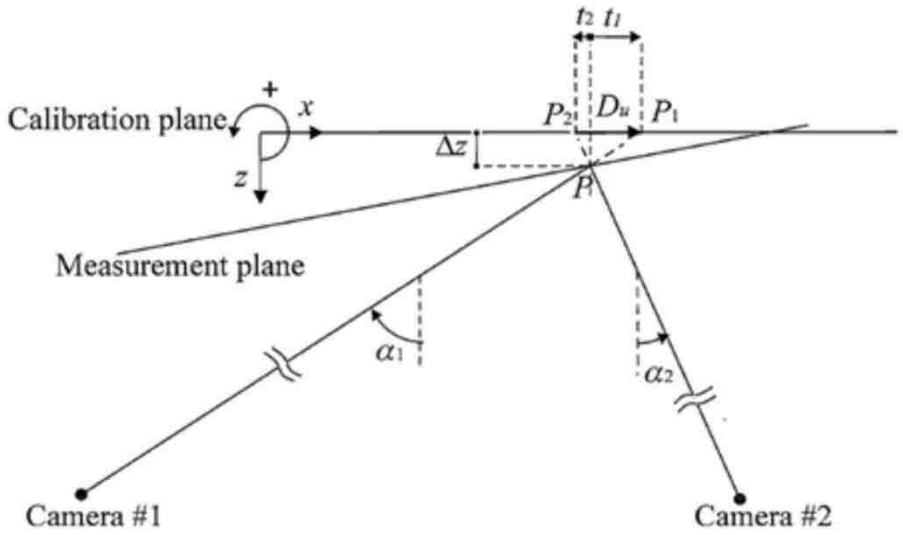

Figure 2.9 : Sketch of generic misalignment error between calibration and measurement planes (Giordano and Astarita, 2009).

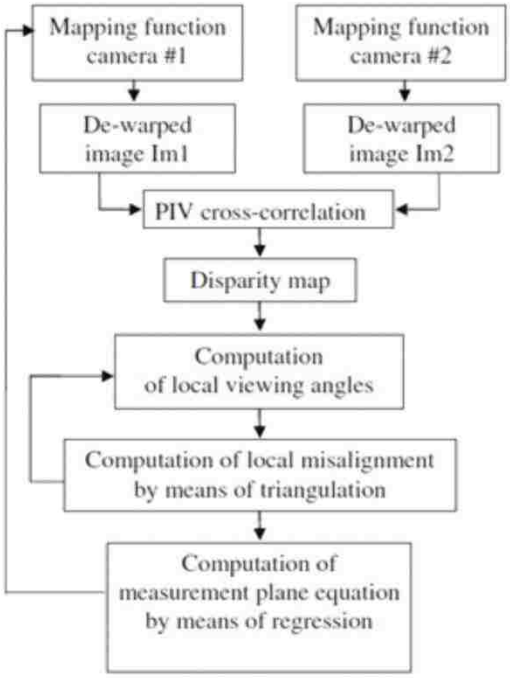

Figure 2.10 : Scheme of the procedure used to correct the misalignment error between calibration and measurement planes (Giordano and Astarita, 2009)

.

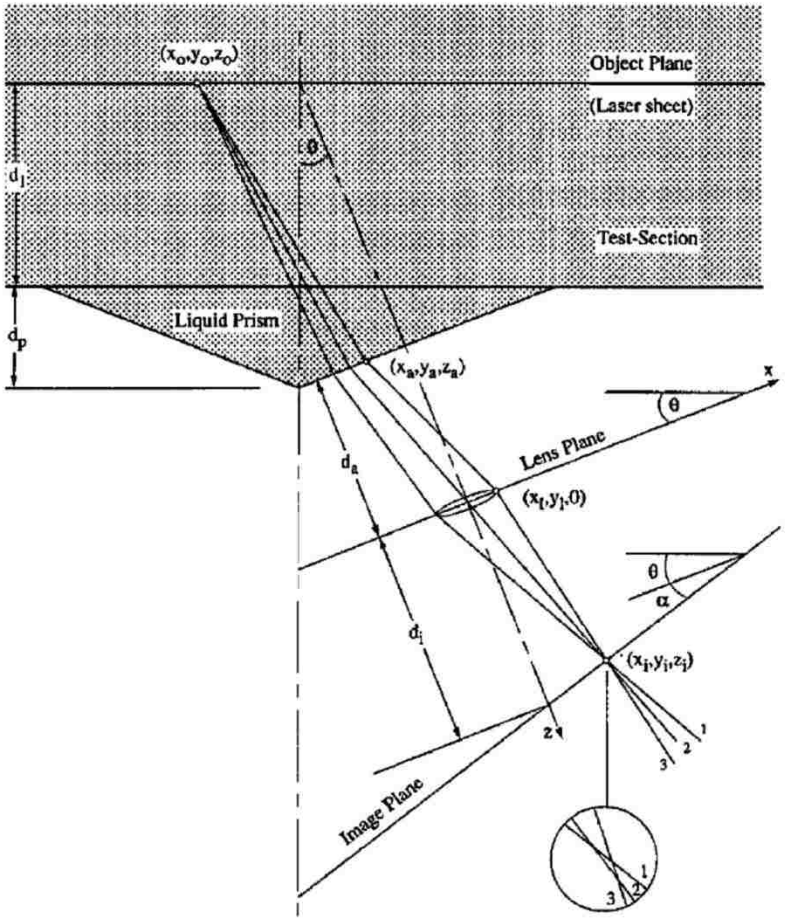

Figure 2.11 : Scheimpflug SPIV with liquid prism (Prasad and Kirk, 1995).

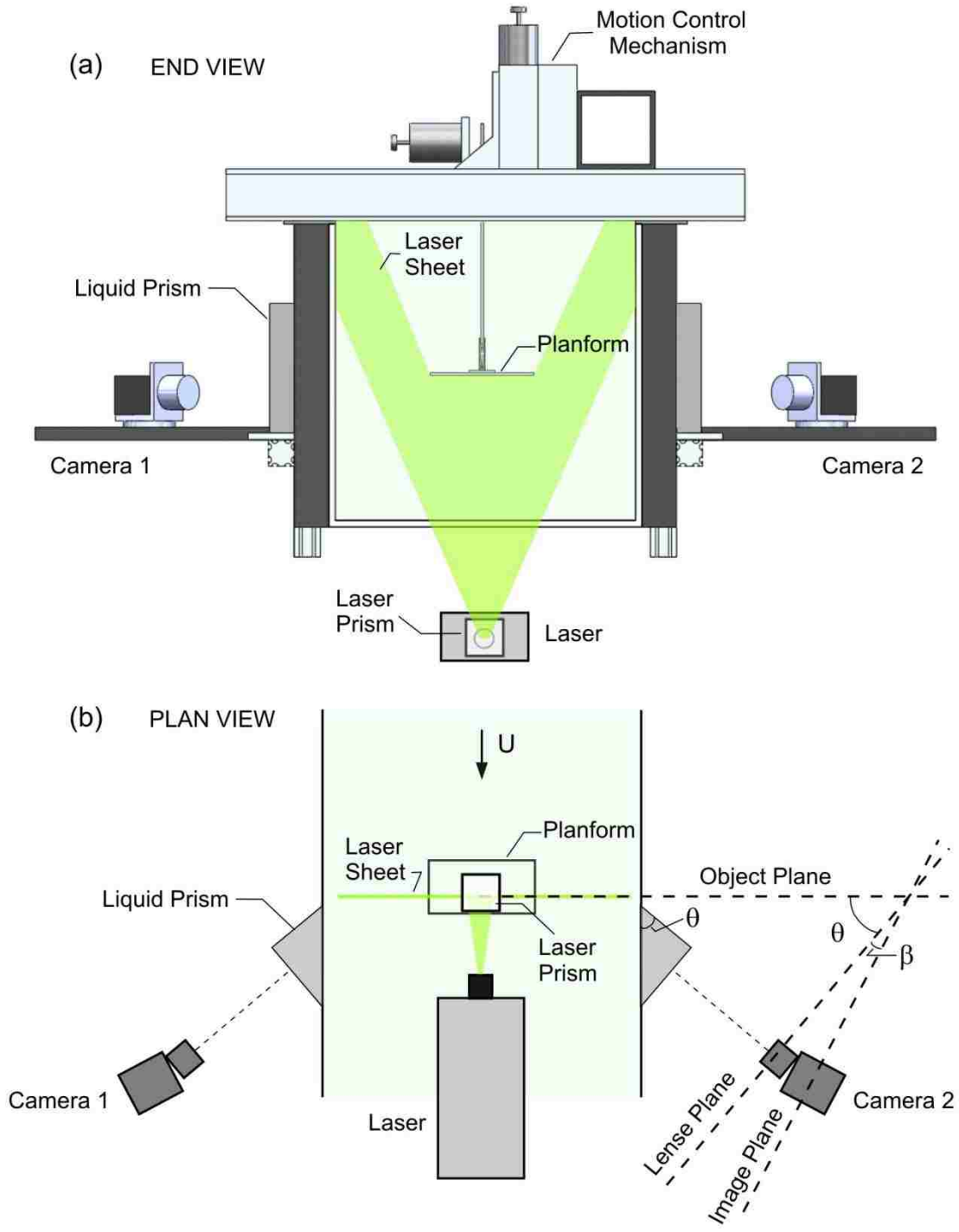

Figure 2.12 : Overview of stereo imaging system for acquiring images in cross-flow planes. **(a)** End view of the system, **(b)** Plan view of the system.

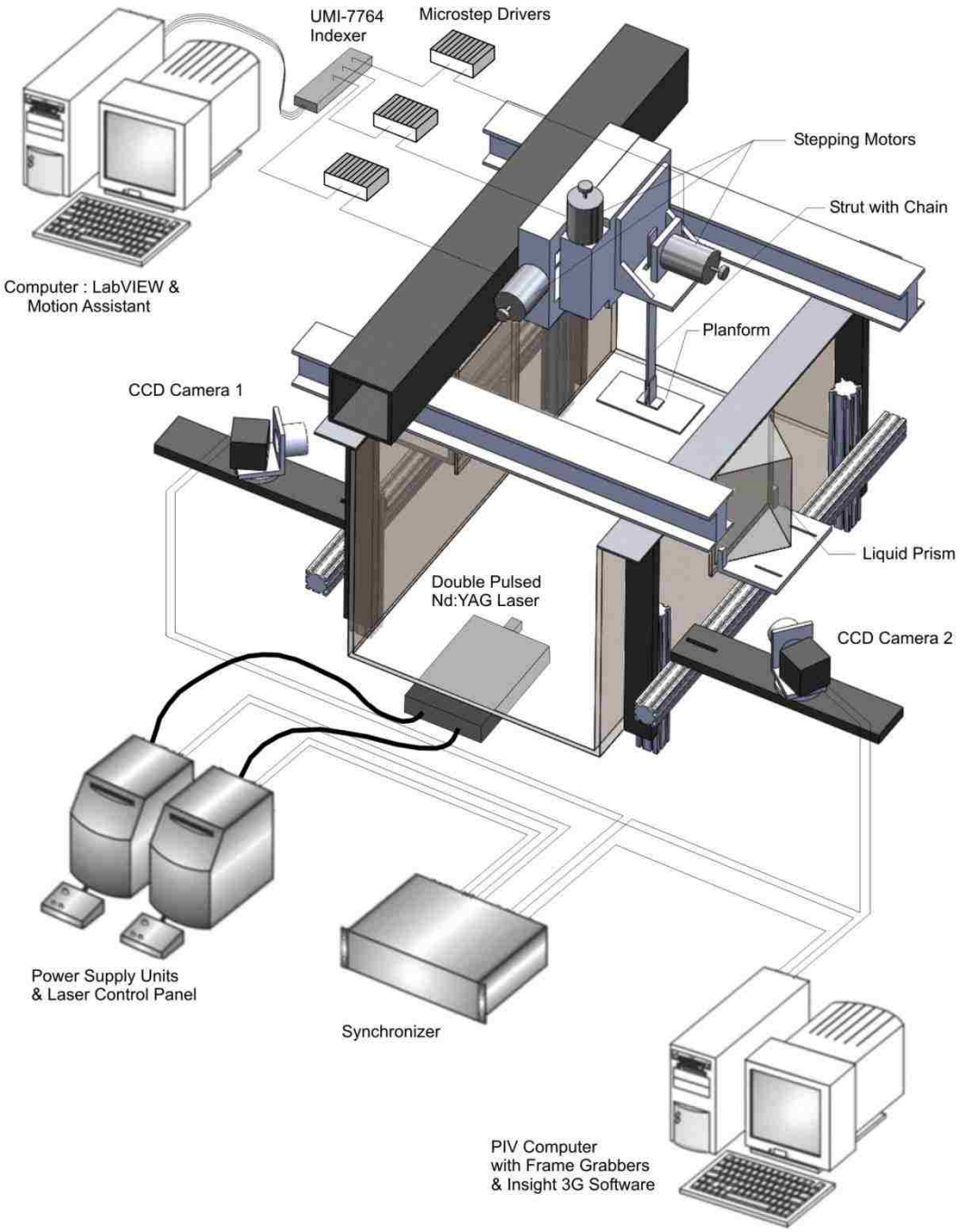

Figure 2.13 : Overview of experimental components, including wing planform, motion control mechanism and SPIV system

CHAPTER 3

FLOW STRUCTURE ON A LOW ASPECT RATIO PLUNGING WING

In this chapter, a technique of high-image-density particle image velocimetry is employed to characterize the time evolution of the three-dimensional flow structure on a low aspect ratio rectangular wing, which is subjected to two types of pure periodical plunging motion: triangular; and sinusoidal. In addition to quantitative imaging, a technique of flow (dye) visualization is employed to demonstrate the major features of the flow structure during an oscillation cycle.

In section 3.1, the experimental setup and the motion kinematics are briefly described. Then, the timewise development of the flow patterns is shown in section 3.2, in conjunction with cross-comparison of flow visualization and PIV measurements at selected cross-flow planes. In section 3.3, the measurement of circulation during an oscillation cycle is performed in order to determine the strength of vortical structures at various spanwise locations. The time-evolution of the flow-field and the three-dimensional vortical structure is addressed in section 3.4 in terms of phase-averaged vorticity and spanwise velocity, as well as space-time representations of instantaneous vorticity patterns in the cross-flow direction. Furthermore, the effect of Reynolds number on the flow structure is addressed in section 3.5. Finally, concluding remarks are given in section 3.6.

3.1 EXPERIMENTAL SYSTEM AND METHODOLOGY

3.1.1 Overview of Experimental Setup and Motion Kinematics

An overview of the experimental setup is given in Figure 3.1. A rectangular wing configuration was employed, which had the form of thin brass plate, with a chord C = 101.6 mm and a total span $2b$ = 203.2 mm, giving an aspect ratio of 2. The thickness of the plate was t = 1.59 mm, corresponding to t/C = 0.016. The leading- and trailing edges of the plate, as well as the edges of the tips of the plate were sharp and squared-off (not beveled). The plate was held in position by a thin sting mounted at mid-chord and mid-span. The maximum width of the sting was $0.032b$, and its streamwise length was $0.25C$; a cross-sectional view of the sting is given in the plan-view of the schematic at the bottom of Figure 3.1a. A complementary experiment was performed with the sting at mid-chord and quarter span; quantitative images of the flow structure across the entire span of the wing were essentially indistinguishable, within experimental uncertainty, from those associated with the mid-span location of the sting. The sting was attached to a vertically-oriented traverse table, which was driven by a high resolution stepping motor. The angle-of-attack of the plate was maintained at $\alpha = 8°$.

The pure plunging motion had two different forms; a triangular form, involving successive positive and negative linear ramps, and a sinusoidal form, as illustrated in Figure 3.1b. The corresponding effective angle attack values $\alpha_{eff} = 8° + tan^{-1}(\dot{h}/U)$, are represented in the schematic of α_{eff} vs. t'. The effective smoothing at the corners of the triangular function had a duration $\Delta t/T \sim 0.005$, where T is the period of

the function. Zoomed-in views of the PIV imaging as well as the dye visualization showed no irregularities of the flow structure at the sensitive region of the leading-edge, e.g., generation of small-scale instabilities or vortices was not detectable, when the motion passed through a corner of the triangular function. The effects of this triangular motion are briefly compared with the corresponding sinusoidal motion. For both types of motion, the frequency and reduced frequency were respectively f = 0.28 Hz and $k = \pi fC/U = 1.0$. The amplitude was $h_{max} = 0.25C$, corresponding to a peak-to-peak amplitude of $0.5C$. The freestream velocity was maintained at 90 mm/sec, and the Reynolds number based on chord C was 10,000.

3.1.2 Particle Image Velocimetry and Dye Visualization

For the PIV experiments, the laser sheet was oriented vertically at a given value of streamwise location x/C along the plate as shown in Figure 3.1c. Independent dye marker visualization was accomplished by dye injection. Dye ports of diameter 1 mm were drilled into the leeward side of the wing at spanwise locations corresponding to distances from the plane of symmetry of 23%, 47%, 70%, and 94% of the semi-span b. These holes were a distance of $0.0098C$ from the leading-edge, and $0.12b$ and $0.24b$ from the plane of symmetry of the plate. Two cameras were employed simultaneously for recording dye visualization, one in the plan view (y direction) and the other in the side view (- z direction).

Quantitative features of the flow structure were determined using a technique of particle image velocimetry. The location of the laser sheet is indicated in the schematics of Figure 3.1c. The one-micron filtered water was seeded with metallic-coated hollow plastic spheres having a diameter of 12 microns, with sufficiently high

density such that the interrogation window of 32 pixels × 32 pixels typically contained a minimum of 20 particle images. The laser sheet of 1 mm thickness was generated by a dual pulsed Yag laser system having a maximum output of 90 mJ. The pulse rate of the lasers was such that image pairs were acquired at a rate of 15 Hz. Images were captured using a camera with an array of 1600 pixels × 1200 pixels. The effective magnification of the camera provided a resolution in the plane of the laser sheet between 4.94 and 5.59 pixels/mm. The patterns of particle images were processed using a frame-to-frame cross-correlation technique, and a standard overlap of 50% was employed, in accord with the Nyquist criterion As a consequence, the spatial sampling separation of the velocity data was 3.2 to 2.8 mm, yielding a maximum of approximately 7,227 velocity vectors within the field of view. The bias error of the peak vorticity of the major vorticity concentrations of interest herein, due to the spatial sampling separation, was between 0.1 to 0.4% prior to smoothing and 4 to 5% when an adaptive Gaussian window was employed, based on the assessment of Fouras and Soria (1998).

3.1.3 Phase-averaged Images

In order to determine the phase-averaged patterns shown herein, a total of twenty instantaneous images were averaged. Two cycles of the plate motion elapsed before the start of image acquisition, so these initial cycles were not included in the averaging of images. Since the flow patterns arose from a large-amplitude, controlled forcing, the instantaneous patterns were found to be relatively repetitive from cycle to cycle. As shown in Figure 3.1d, the plot of vorticity magnitude versus the number of

images averaged, evaluated at selected locations in the flow field, indicates that an average of ten images provides a value of phase-averaged vorticity within 0.4% of the asymptotic value.

3.2 VISUALIZATION AND QUANTITATIVE IMAGES OF FLOW STRUCTURE

3.2.1 Dye Visualization and Flowfield Evolution

Dye visualization was employed to illustrate the major features of the flow structure during the oscillation cycle. Figure 3.2.1 compares side and plan views of dye images at successive times $t'/T = 0$ through 0.58 for both type of plunging motion studied herein. Side views of the dye visualization are rotated, so that the plate is vertical, as illustrated in the schematic. The first row of images, at $t'/T = 0$, corresponds to attainment of the maximum positive displacement $h(t')$. Shortly thereafter, at $t'/T = 0.08$, corresponding to the second row images, the occurrence of pronounced axial flow during the initial formation of the small-scale leading-edge vortex is evident for the triangular motion. However, only a small-scale leading-edge vortex formation appears for the sinusoidal plunging case at this instant of time. At successively larger instants of time, the fronts of the dye marker move towards the plane of the symmetry. At $t'/T = 0.17$, and at $t'/T = 0.25$, the collision of the dye fronts is evident in the vicinity of the plane of symmetry for both cases. After this collision, at $t'/T = 0.42$ and 0.58, severe distortion of the visualized structures yields the occurrence of large-scale, elongated dye clusters; as will be demonstrated, these clusters represent streamwise-oriented, as well as surface-parallel-oriented vortical structures. At values of $t'/T = 0.67$ to 1.0, dye visualization (not shown herein) indicates that the pattern of streamwise vortical structures moves towards, and

eventually past, the trailing-edge of the wing. At t'/T = 1.0, only a fraction of the originally marked dye pattern remains upstream of the trailing-edge. The occurrence of these features can be related to the effective angle of attack α_{eff}. For the triangular plunging case, at t'/T = 0 through 0.42, α_{eff} = 26.4°, and at t'/T = 0.58 through 1.0, α_{eff} = -10.4°. The effective angle of attack profile for the sinusoidal plunging motion ranges between 34.7° and -16.1°, and its maximum and minimum appear at t'/T = 0.25 and 0.75 respectively as shown in Figure 3.1b.

From the overall examination of the dye images in Figure 3.2.1, it can be concluded that the formation process, scale, and downstream progression of the leading-edge vortex do not differ significantly between triangular and sinusoidal plunging motions. Furthermore, the occurrence of pronounced axial flow through the leading-edge vortex is evident for both cases during the earlier states of downstroke. However, after the aforementioned collision of the dye clusters in the vicinity of the plane of symmetry, the side-view images indicate that the leading-edge vortex on the wing, subjected to the sinusoidal motion broadens relatively further away from the wing surface. The other distinguishing feature of the sinusoidal plunge case, relative to the triangular plunge, is the presence of a well-organized, highly concentrated leading-edge vortex. For the case of triangular plunge, the leading edge vortex shows a substantial distortion at the end of downstroke due to the sharp deceleration and acceleration of the wing.

3.2.2 Phase-averaged Quantitative Images of Flow Structure

Figure 3.2.2 directly compares patterns of quantitative images and dye visualization images in selected cross-flow planes for both triangular and sinusoidal

plunge cases. The top set of images of Figure 3.2.2 is on the plane at x/C = 0.2, at the instant t'/T = 0.17 for the triangular case, and at t'/T = 0.25 for the sinusoidal case. Contours of constant transverse velocity w are normalized by the freestream velocity U, i.e. w/U. The maximum value of w/U = 0.73 and 0.78 for the triangular and sinusoidal motions respectively. The strength of the pronounced axial flow through the leading-edge vortex is slightly higher for the sinusoidal case. The middle and bottom sets of images of Figure 3.2.2 are on the plane at x/C = 0.7, at the instant t'/T = 0.58. The contours of normalized transverse velocity w/U exhibit maxima located closer to the plane of symmetry of the wing, relative to the maxima at x/C = 0.2. In addition to the predominant contours of w/U adjacent to the surface of the plate, for which the maximum value of w/U = 0.67 and 0.75 for the triangular and sinusoidal cases respectively, secondary contours appear above them, due to the rotational motion of the streamwise-oriented vortices. The contours of high magnitude transverse velocity, designated by the colors of dark blue and dark red for the sinusoidal case occupy a larger region relative to the triangular case. Corresponding contours of constant vorticity $\omega C/U$ are also shown in the bottom set of images. At this instant, the scale and circulation of these larger-scale concentrations dominate the tip vortices for both cases.

The very rapid evolution with time of the streamwise-oriented vortical structures near the plane of symmetry is shown in the images of Figure 3.2.3. These images correspond to the relatively close instants of time t'/T = 0.5 and 0.67, located on the plane at x/C = 0.7. The abrupt change of the flow structure involves, first of all, a reduction to zero of the scale and strength of the tip vortices, which is evident in the

patterns of velocity vectors $\underline{V}$, contours of constant w/U, and contours of constant vorticity $\omega C/U$ at t'/T = 0.67. Moreover, the scale and strength of the counter-rotating vortex system located at the plane of symmetry rapidly increases in going from t'/T = 0.5 to 0.67, as indicated by the contours of $\omega C/U$. As shown in the patterns of velocity vectors $\underline{V}$, the associated swirl increases as well. The bottom row of images indicates that, at a downstream location where the streamwise vortices have developed, the form and location of the pronounced concentrations of streamwise vorticity $\omega C/U$ are similar; sinusoidal motion results in even larger circulation. For the triangular motion, at t'/T = 0.17 and 0.67, the effective angle attack $\alpha_{eff} = 8° + tan^{-1}(\dot{h}/U)$ is 26.4°, and -10.4° respectively, and for the sinusoidal motion at t'/T = 0.25 and 0.67, α_{eff} = 34.7°, and -16.1°.

3.3 EFFECT OF MID-PLANE VORTICES ON CIRCULATION

In addition to the characterization of flow patterns described in previous sections, a circulation calculation is performed at x/C = 1.1, in order to understand the effect of large-scale, streamwise-oriented, mid-plane vortical structures, and the effect of tip vortices on the total circulation. Figure 3.3 shows a graph of normalized circulation $\Gamma/2bU$ of the sinusoidal motion during one period t'/T = 0 to 1.0, the patterns of streamwise vorticity $\omega C/U$, and the spanwise distribution of the circulation at selected instants of time. In this graph, total normalized circulation, indicated with the black line, represents the sum of the circulation, contributed by the tip vortices (blue dashed line) and the mid-plane vortices (red dashed line). Values of circulation are computed from the velocity data with the methodology described in section 2.5.

Therefore, distinctive stages of the flowfield development can be analyzed in terms of the circulation strength of the tip and mid-plane vortices.

The graph indicates that the total circulation increases during the downstroke t'/T = 0 to 0.5, and decreases during the upstoke t'/T = 0.5 to 1.0. It should be stated that foregoing distribution of the total circulation with the time t'/T is specific to the selected spanwise plane, where x/C = 1.1. At this point, one can expect that the circulation distribution will change on a spanwise plane at a different location. But, the strength of the tip and mid-plane vortices, and their effect on the circulation can be still revealed from the circulation graph at x/C = 1.1 in Figure 3.3.

The normalized total circulation values vary in the range of $\Gamma/2bU$ = -0.35 to 0.375 during the cycle. As seen on the graph, it is evident that the tip vortices have a larger positive contribution to the total circulation, relative to the contribution of the mid-plane vortices. But, there is also a positive contribution of the mid-plane vortices to the circulation at the instants between t'/T = 0.2 and 0.8. The circulation reaches its maximum towards the end of the downstroke at t'/T = 0.42. The graphs, which show the spanwise distributions of circulation at various instants of time, and the corresponding patterns of streamwise vorticity contours, reveal how the mid-plane and the tip vortices contribute to the circulation. During the final states of the upstroke and the earlier states of the downstoke, it is evident that large-scale concentrations of the mid-plane vortices dominate the tip vortices. Moreover, the circulation strength of the mid-plane vortices is substantially higher than the circulation strength of the tip vortices.

3.4 TIME EVOLUTION OF FLOW STRUCTURE

3.4.1 Phase-averaged Patterns of Spanwise Velocity

In this section, the time evolution of the flow structure is presented for both of the aforementioned plunging motions, in terms of the patterns of spanwise velocityand streamwise vorticity contours. In Figure 3.4.1, the space-time images of the phase-averaged transverse velocity contours w/U are shown in the cross-flow plane at x/C = 0.7 during an oscillation cycle. For both cases, a pronounced transverse flow, which is directed from the wing tips toward the plane of symmetry, first occurs at the instant of t/T = 0.17, and it reaches to the plane of symmetry at the end of downstroke at t/T = 0.25. After the interaction of the opposing flows at t/T = 0.33, the patterns of velocity contours indicate that the flow towards the plane of symmetry starts to decay, and disappears at t/T = 0.58. During this time period, a transverse flow pointing away from the plane of symmetry originates on the centerline. It strengthens during the upstroke, and reaches its maxima at t/T = 0.58. However, during the initial states of the downstroke, from t/T = 0.75 to 0.08, no significant spanwise flow is evident for both types of plunging motion.

Comparing the space-time images of the phase-averaged patterns of velocity contours in Figure 3.4.1, it can be concluded that there is an overall similarity between the sinusoidal and triangular cases in terms of formation, decay and reversal of the spanwise flow. However, the patterns of velocity contours on the wing corresponding to the sinusoidal case indicate relatively larger transverse flow at any instant of the plunge cycle.

3.4.2 Phase-averaged Patterns of Streamwise Vorticity

The space-time images of the phase-averaged streamwise vorticity $\omega C/U$ contours in the cross-flow plane x/C = 0.7 are shown in Figure 3.4.2. The corresponding instantaneous patterns of streamwise vorticity $\omega C/U$contours are also shown in Figure 3.4.3. The red colored contour levels represent the clockwise, and the blue colored contours represent the counter-clockwise rotating vortices. The patterns of vorticity contours indicate two types of primary vortex formation during the plunging cycle; the tip, and the mid-plane vortex formation. The tip vortices on the upper surface of the wing start forming at t/T = 0.75, where the downstroke motion begins. They keep growing in size, and become stronger during the downstroke. At t/T = 0.33, right after the beginning of upstroke motion, the tip vortices on the upper side of the wing decay, and finally disappear at t/T = 0.42. However, during the later stages of the motion, tip vortices are generated on the other side of the wing. The initial formation of these vortices is evident at t/T = 0.42, and t/T = 0.5, on the lower side of the wing subjected to sinusoidal and triangular plunge motion respectively. From the overall examination of the patterns of the tip vortices, it is evident that the tip vortices, forming during the downstroke, are larger and stronger compared to the tip vortices, which form during the upstroke. This distinctive feature is expected to be seen because the wing is maintained at a value of angle-of-attack α = 8°.

3.4.3 Instantaneous Patterns of Streamwise Vorticity

In addition to tip vortex formation, large-scale, distinct patterns of the counter-rotating mid-plane vortices are also evident in the vicinity of the plane of symmetry

during half of the plunge cycle. As seen in Figure 3.4.3, the initial formation of these structures appears at t/T = 0.2, and t/T = 0.14 for the sinusoidal and triangular cases respectively. Following the interaction of the transverse flows at the plane of symmetry, abrupt changes of the three-dimensional flow structure occur. These changes include extension and strengthening of the counter-rotating mid-plane vortices until the instant t/T = 0.42 for the sinusoidal, and t/T = 0.36 for the triangular case. At later times, these vortices start decaying, and finally disappear at t/T = 0.67 for the sinusoidal, and t/T = 0.6 for the triangular case.

Considering the entire set of images in Figure 4.3.1 through Figure 4.3.3, and cross-comparing the patterns of the space-time images of the sinusoidal and triangular cases, it can be concluded that the time evolution of the flow structure is very similar in terms of the formation, decay, and the reversal of the wing tip vortices, and the formation of the mid-plane vortices. However, the initiation and evolution of the mid-plane vortices for the triangular plunging case occur at an earlier instant of the cycle, i.e.at t/T = 0.06, relative to the sinusoidal case.

3.4.4 Flow Patterns in Various Cross-Flow Planes

In this section, the three-dimensional flow structure on the wing, subjected to triangular plunging motion, is addressed with the interpretation of phase-averaged patterns of spanwise velocity, velocity vectors, and streamwise vorticity. Figure 3.4.4 shows these patterns at a selected instant, t/T = 0.25, on seven different cross-flow planes, between x/C = 0.1 and x/C = 1.1. In the top image, the patterns of the transverse velocity contours indicate an axial flow away from the plane of symmetry in the vicinity of leading-edge, as previously addressed in section 3.2. However, in the

cross-flow planes, at x/C = 0.3 and 0.5, the velocity contours evince a pronounced axial flow adjacent to the surface of the wing, which is directed from the wing tips toward the plane of symmetry. Furthermore, secondary contours appear above them, due to the rotational motion of the streamwise-oriented vortices, which are represented in the bottom image. The streamwise-oriented vortices, as well as the tip vortices, are also evident in the patterns of velocity vectors, shown in the middle image of Figure 3.4.4. At the mid-chord plane, x/C = 0.5, the scale and the circulation of the mid-plane structures dominate the tip vortices.

At x/C = 0.7, the spanwise velocity contours display a large region of transverse flow, towards the plane of symmetry, which can be also observed in the patterns of the velocity vectors, colored by the velocity magnitude. At a location further downstream, i.e., x/C = 0.9, both the spanwise flow, and the streamwise-oriented vortical structures decrease in size and magnitude, and they vanish in the wake region, where x/C = 1.1.

3.5 EFFECT OF REYNOLDS NUMBER

In this section, the Reynolds number effect on the unsteady flow structure over the plunging wing is investigated by considering three different values of Reynolds number ranging from 5,000 to 20,000. Figures 3.5.1 and 3.5.2 show the patterns of phase-averaged spanwise velocity and streamwise vorticity contours respectively in the cross-flow plane x/C = 0.7. Both the patterns of velocity and vorticity contours indicate that the overall flow structure is remarkably similar over the Reynolds number range studied herein. The main features of the flow structure and the sequence of events, including pronounced transverse flow towards the plane of symmetry,

occurrence of large-scale, streamwise-oriented vortices at the mid-plane, and evolution of the tip vortices, are indistinguishable for all Reynolds number values.

3.6 CONCLUDING REMARKS

The time evolution of the unsteady flow patterns on various cross-flow planes along a plunging rectangular wing of aspect ratio two at an angle of attack $\alpha = 8°$ is investigated via techniques of particle image velocimetry and dye visualization. Two types of periodic plunging motion, at a reduced frequency $k = \pi fC/U = 1.0$ and amplitude $h = 0.25C$, are employed in order to clarify how the flow structure is affected by the type of motion, i.e. ramp-like motion with constant velocity and sinusoidal motion with accelerating/decelerating velocity. The time sequences of the cross-flow images are interpreted with instantaneous and phase-averaged contours of spanwise velocity, streamwise vorticity, and velocity vectors. In order to gain a deeper understanding of the evolution of the three-dimensional flow structure, the circulation is calculated at various instants of time during the plunge cycle.

In summary, the timewise development of the patterns of dye given in Figure 3.2.1 show the transformation from pronounced axial flow in the nascent leading-edge vortex to well-defined, streamwise-oriented vortical structures located near the plane of symmetry of the wing, clarified by the quantitative images of Figure 3.2.2. Moreover, the images of Figure 3.2.3 emphasize that abrupt changes of the three-dimensional flow structure can occur over a small time scale, i.e., a fraction of the oscillation cycle. Figure 3.3 indicates that the effect of the mid-plane vortices on the total circulation should be accounted for, even though the tip vortices yield the largest positive contribution to the total circulation. The time sequence of instantaneous and

phase-averaged images given in Figure 3.4.1 through Figure 3.4.4 show that the existence and form of the principal features of the flow structure are preserved for two basic types of motion: successive positive-negative ramps; and sinusoidal motion. This type of three-dimensional vortex formation is expected to be a generic feature of wings undergoing unsteady maneuvers in various modes, where significant accelerations of the leading-edge lead to generation of a pronounced leading-edge vortex. Finally, for both types of plunging motion employed in this study, the overall flow features are found to be indistinguishable over the Reynolds number range from 5,000 to 20,000.

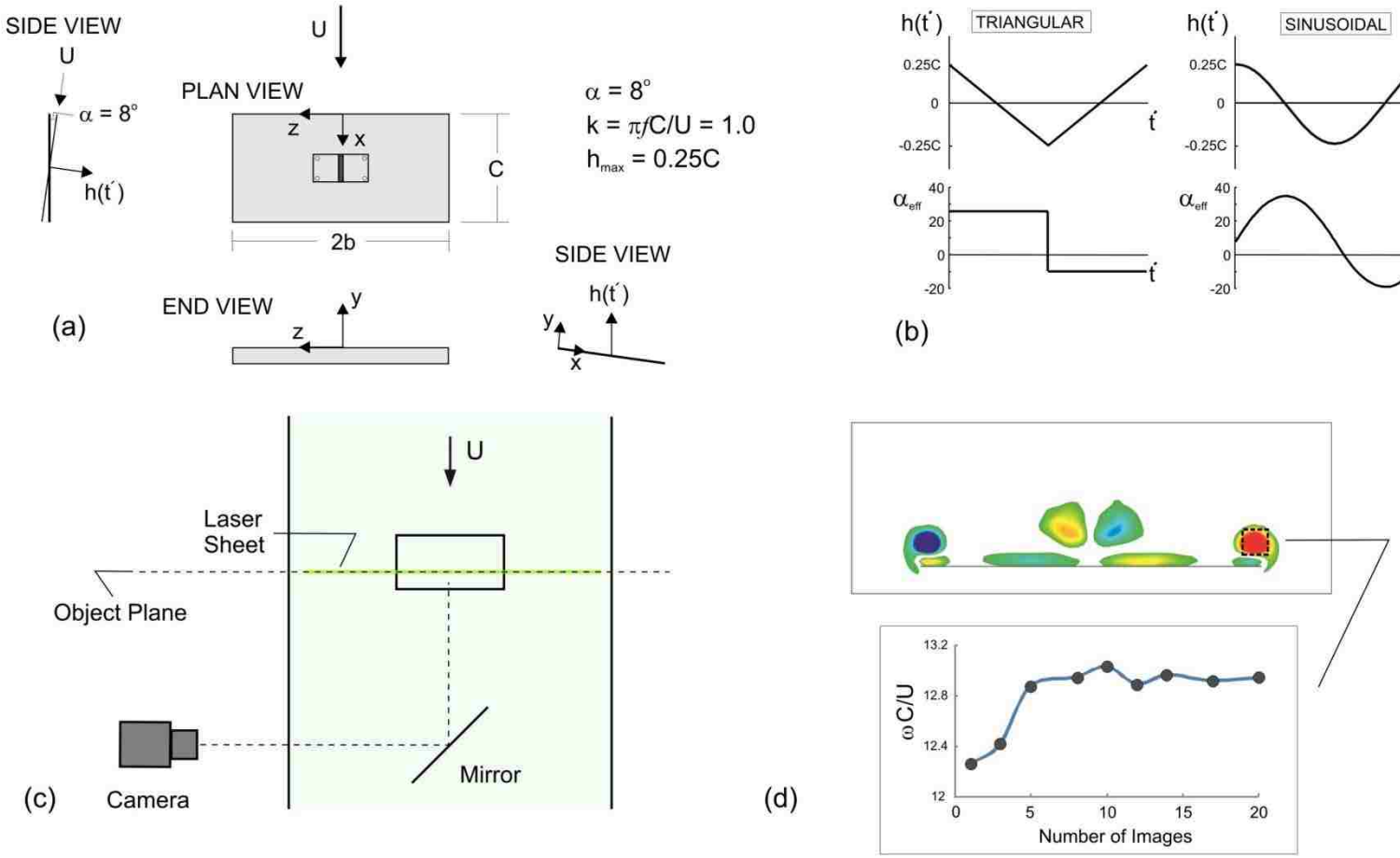

Figure 3.1: (a) Overview of wing configuration; **(b)** plunging schedule of wing motion; **(c)** quantitative imaging system; **(d)** phase-averaging.

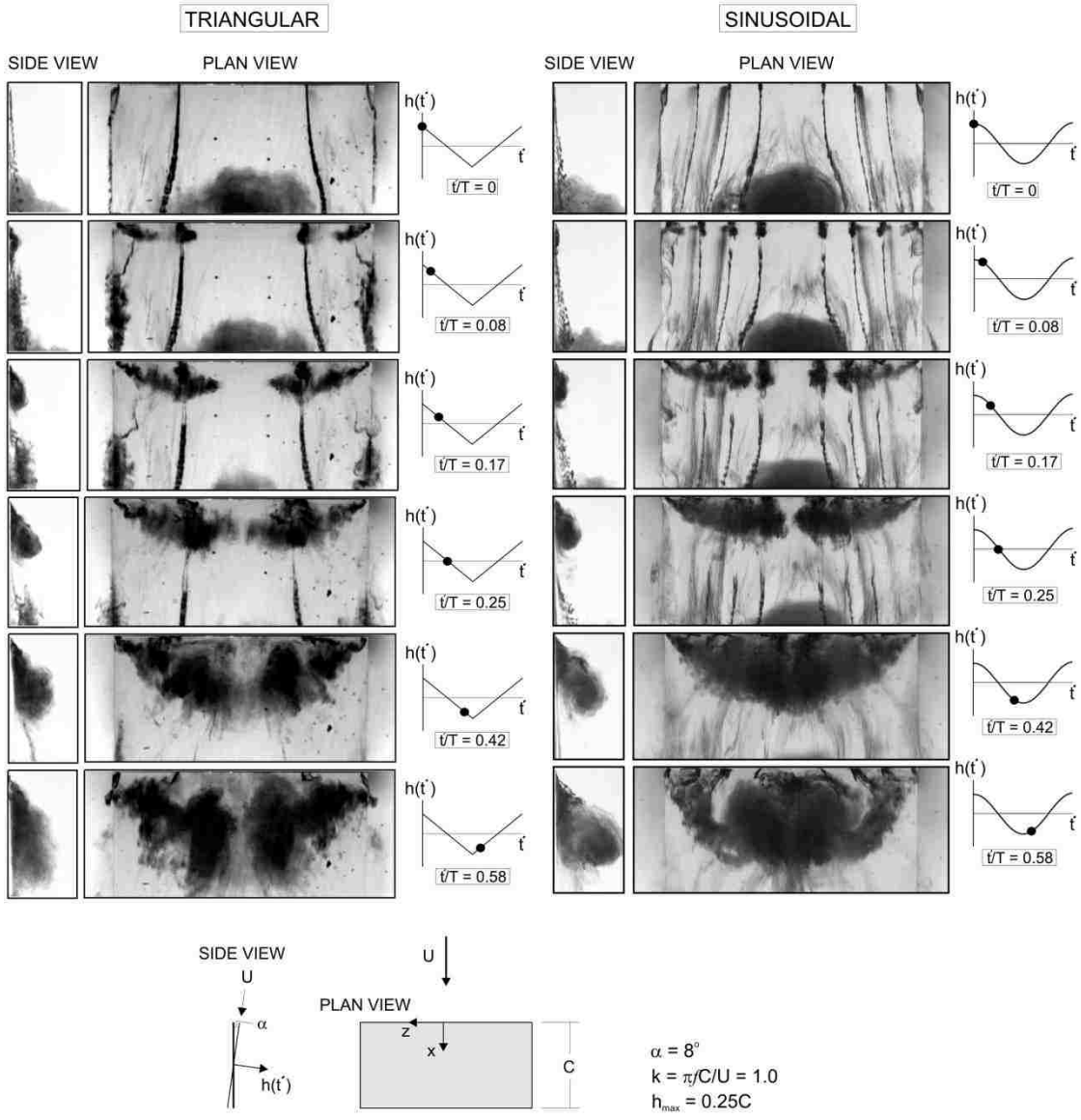

Figure 3.2.1: Onset and development of vortex structure during periodic triangular (left column) and sinusoidal (right column) plunging motion using dye visualization.

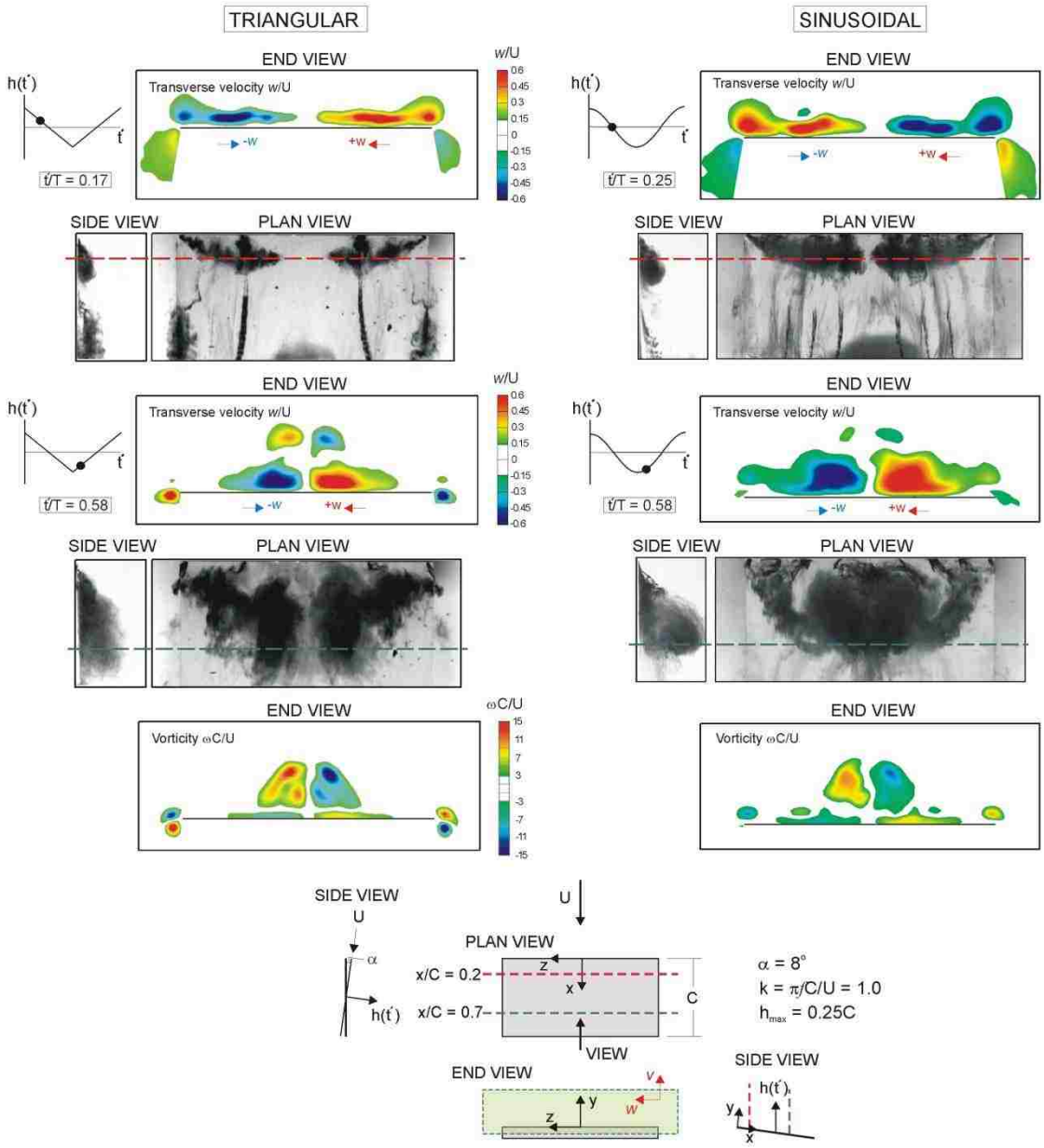

Figure 3.2.2: Dye visualization of three-dimensional vortex formation for triangular (left column) and sinusoidal (right column) plunging motion in relation to images in cross-flow planes.

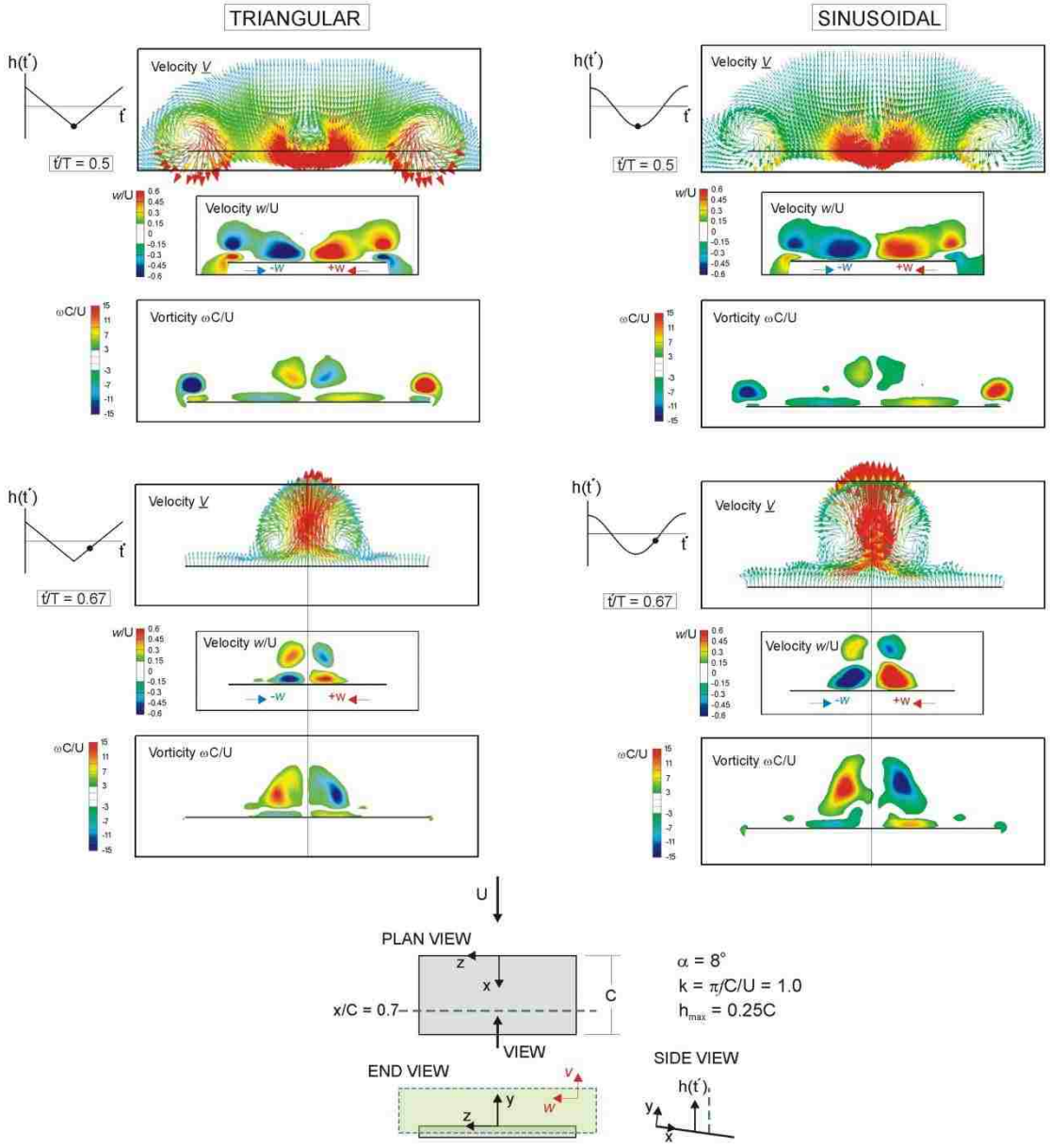

Figure 3.2.3: Quantitative images in cross-flow plane at successive instants of times for triangular (left column) and sinusoidal (right column) plunging motion.

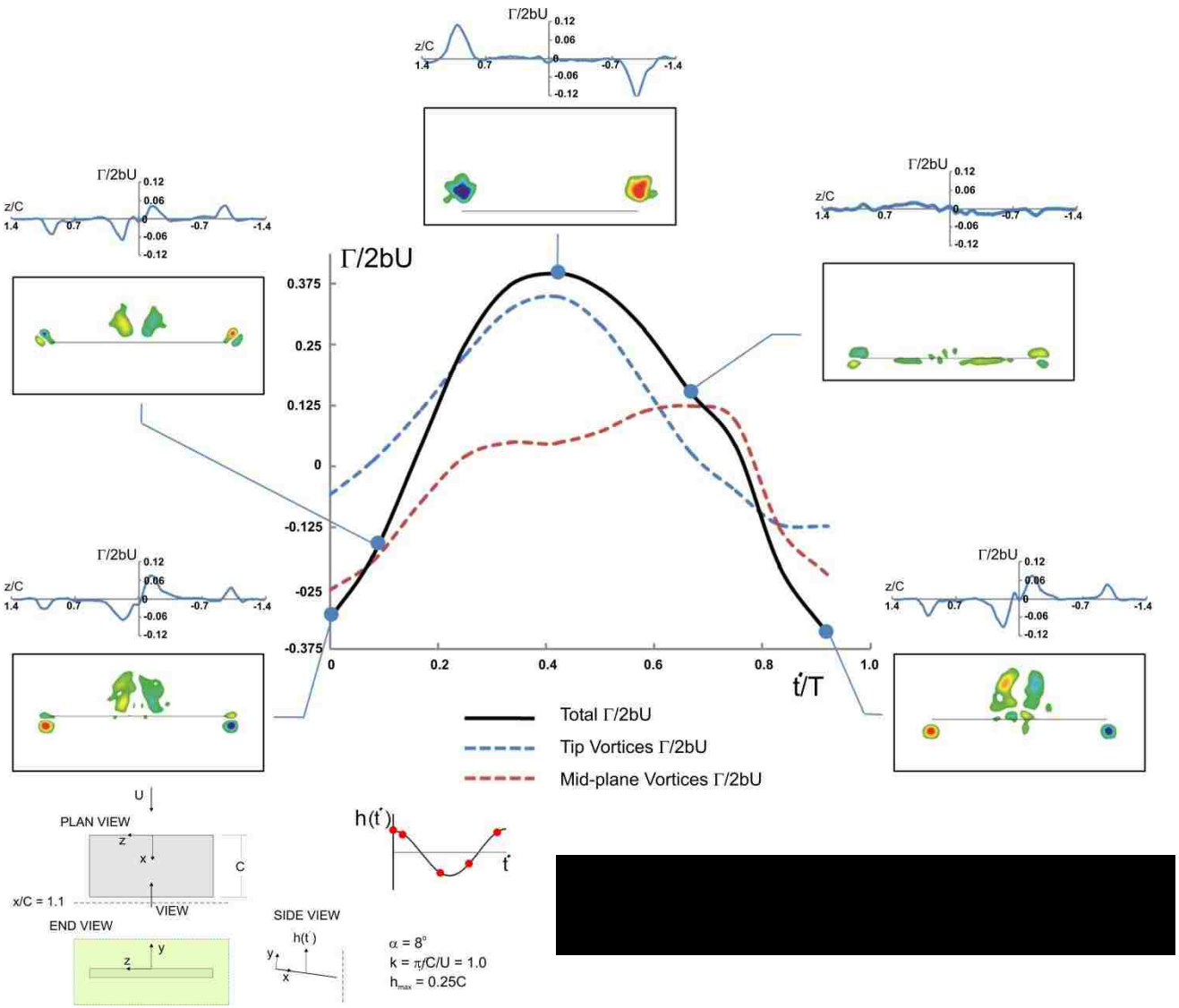
Γ/2bU
z/C
0.12
0.06
0
-0.06
-0.12
1.4
0.7
-0.7
-1.4
Γ/2bU
0.375
0.25
0.125
0
-0.125
-025
-0.375
0
0.2
0.4
0.6
0.8
1.0
t*/T
Total Γ/2bU
Tip Vortices Γ/2bU
Mid-plane Vortices Γ/2bU
U
PLAN VIEW
z
x
C
x/C = 1.1
VIEW
END VIEW
y
z
SIDE VIEW
h(t*)
y
x
h(t*)
t*
α = 8°
k = π/C/U = 1.0
h_max = 0.25C

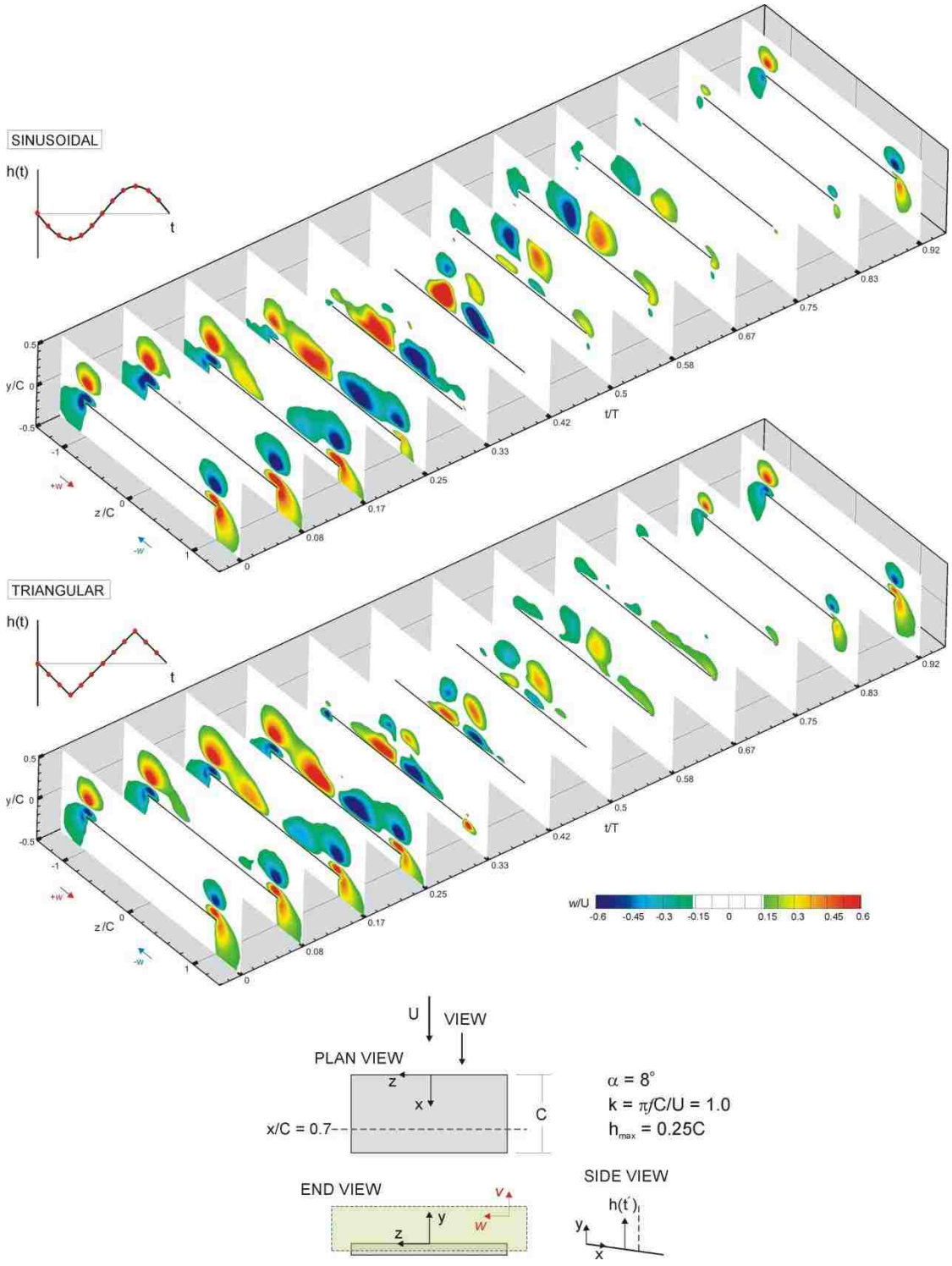

Figure 3.4.1: Space-time images of phase-averaged transverse velocity contours in cross-flow plane during an oscillation cycle of sinusoidal (top image) and triangular (bottom image) plunging motion.

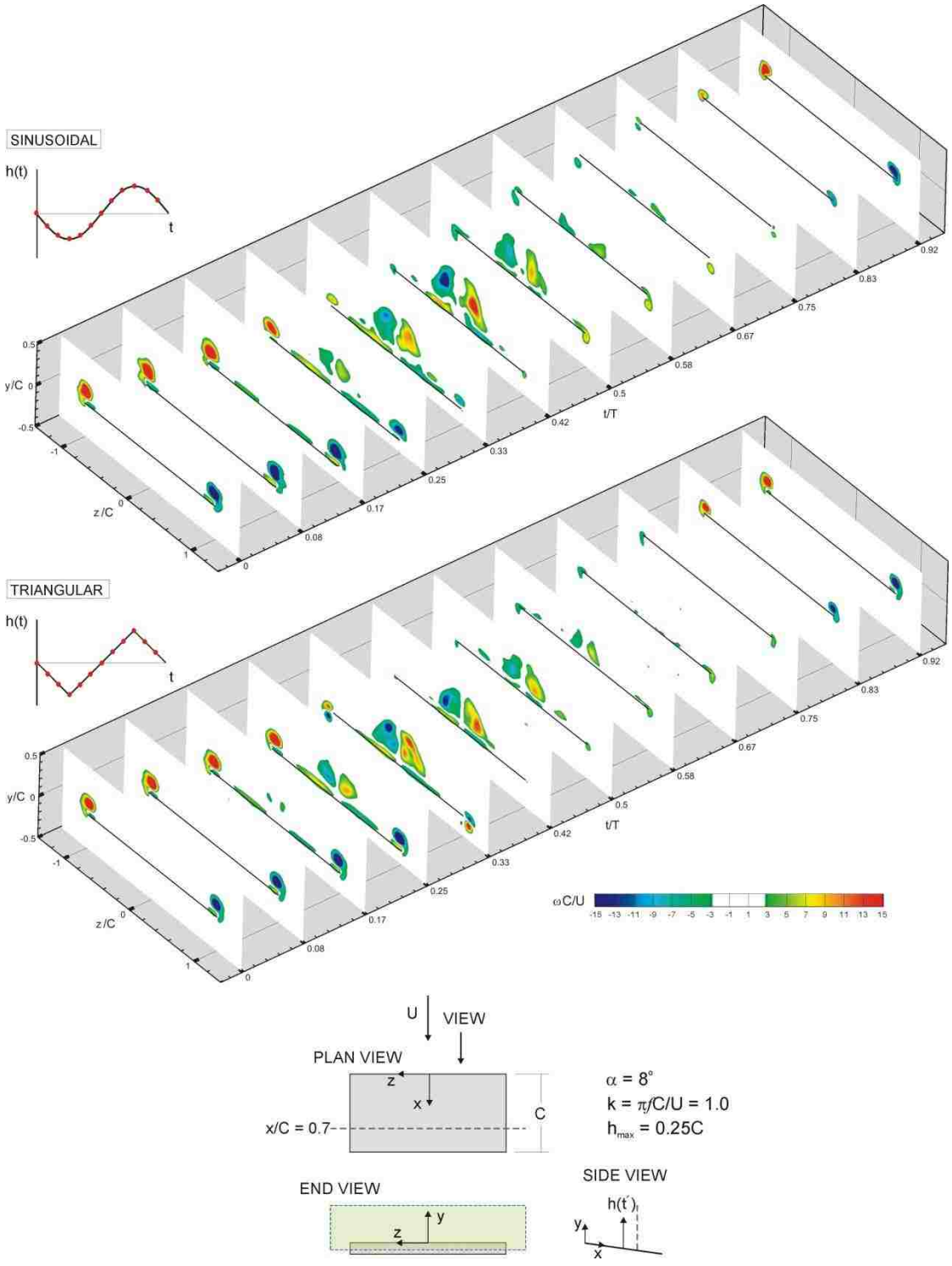

Figure 3.4.2: Space-time images of phase-averaged patterns of streamwise vorticity in cross-flow plane during an oscillation cycle of sinusoidal (top image) and triangular (bottom image) plunging motion.

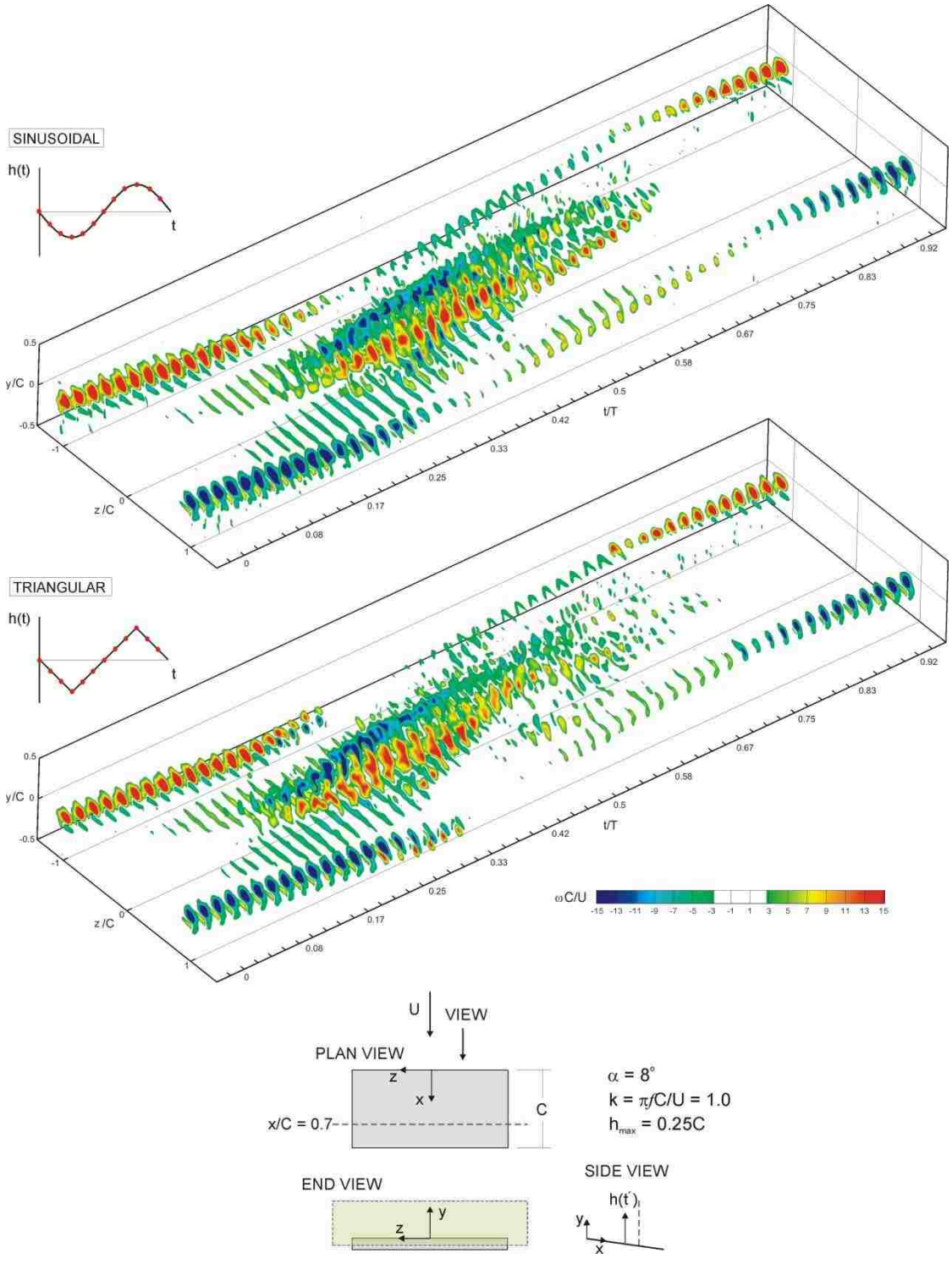

Figure 3.4.3: Space-time images of instantaneous patterns of streamwise vorticity in cross-flow plane during an oscillation cycle of sinusoidal (top image) and triangular (bottom image) plunging motion.

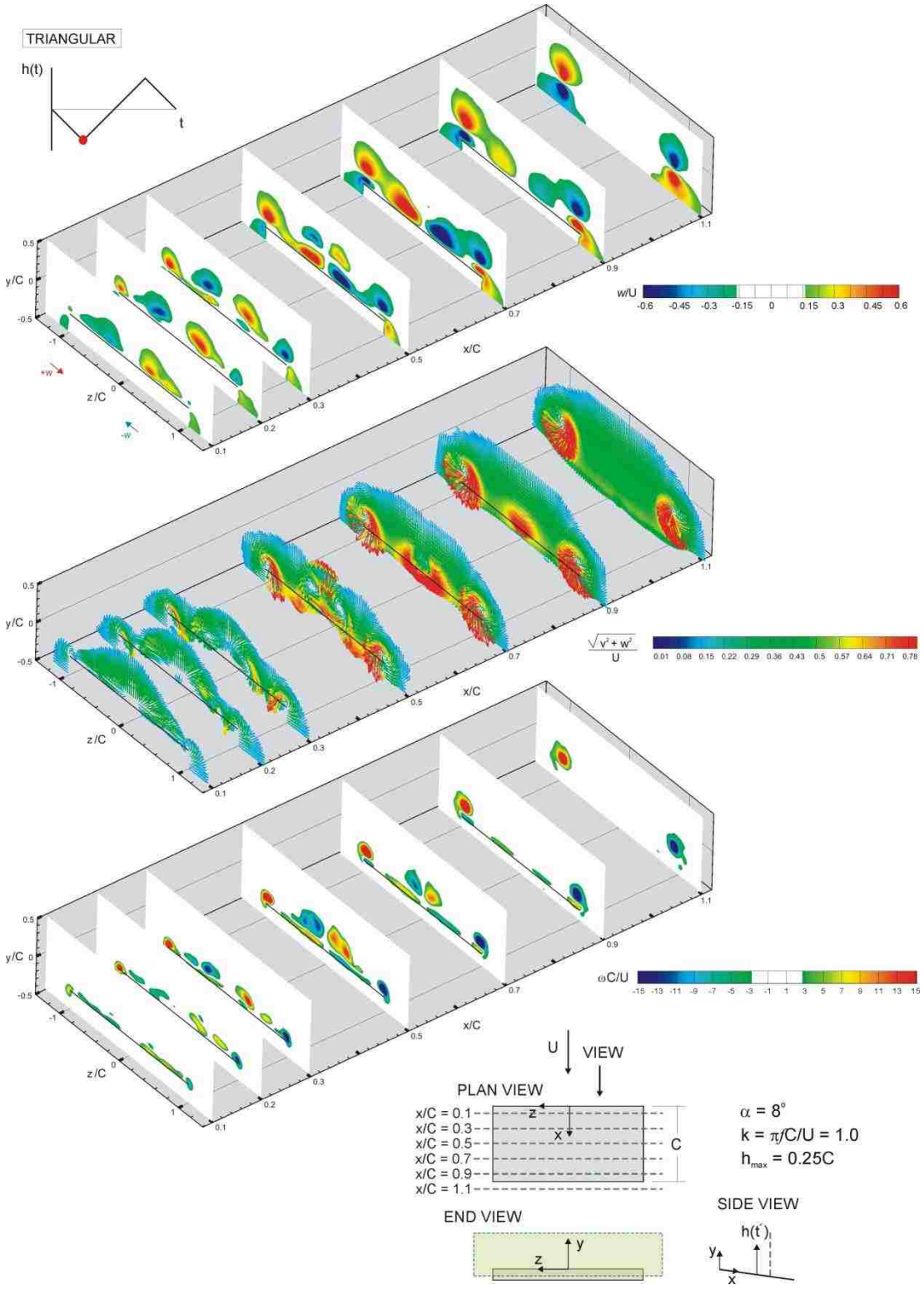

Figure 3.4.4: Phase-averaged patterns of transverse velocity (top image), velocity vectors (middle image), and streamwise vorticity (bottom image) at different cross-flow planes.

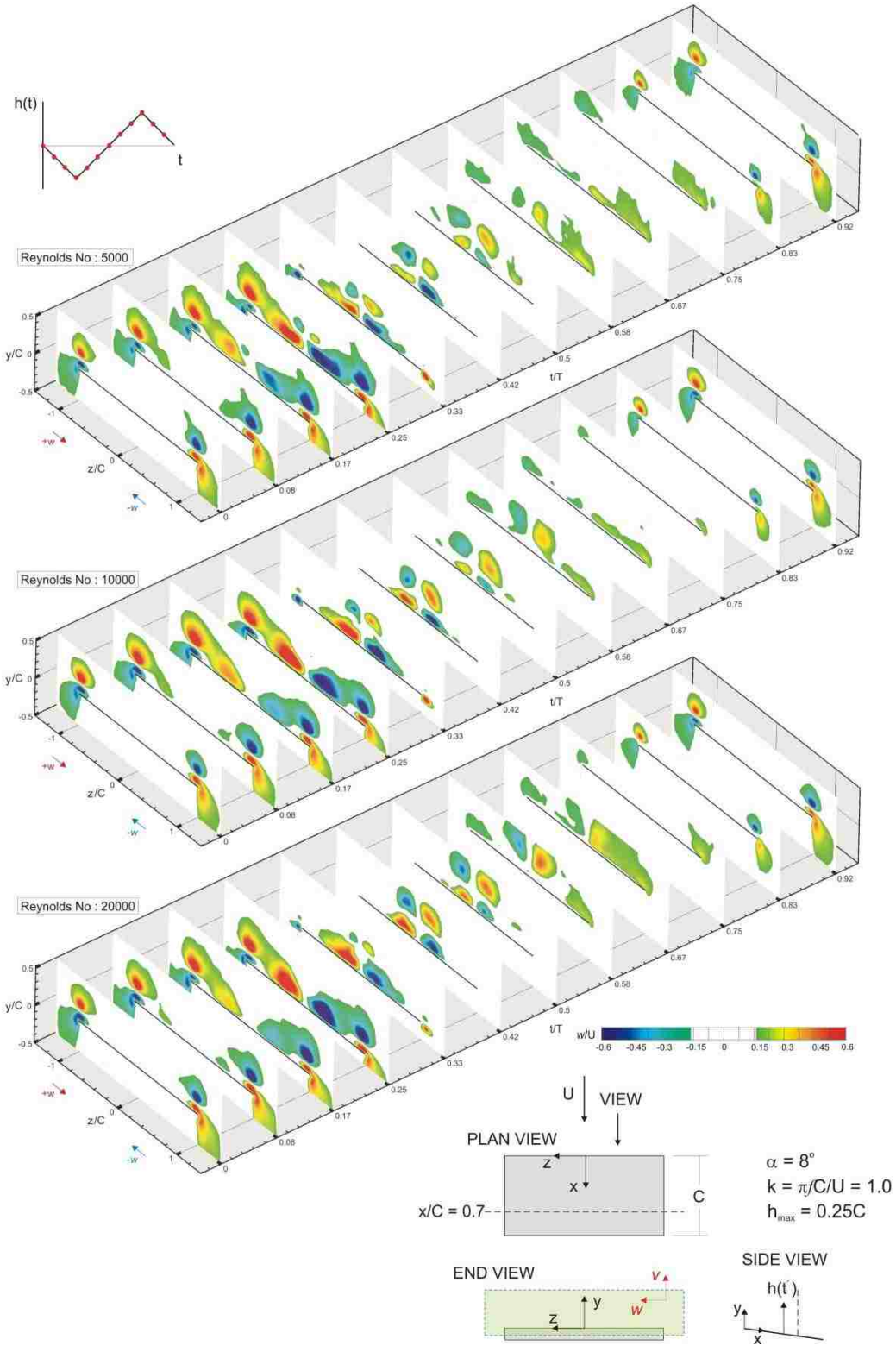

Figure 3.5.1: Phase-averaged patterns of transverse velocity in cross-flow plane for Re = 5,000 (top image), Re = 10,000 (middle image), and Re = 20,000 (bottom image).

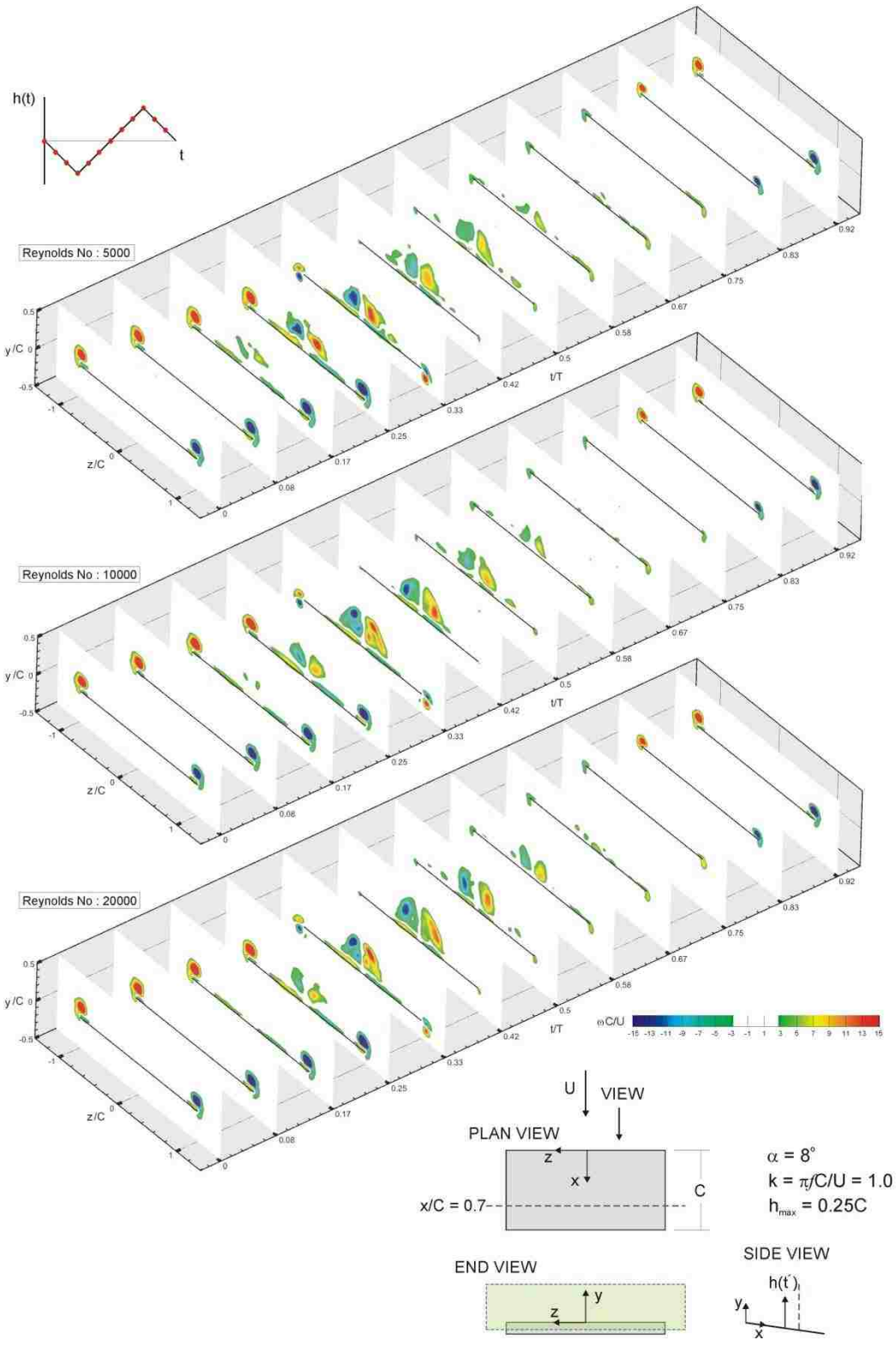

Figure 3.5.2: Phase-averaged patterns of streamwise vorticity in cross-flow plane for Re = 5,000 (top image), Re = 10,000 (middle image), and Re = 20,000 (bottom image).

CHAPTER 4

TIME EVOLUTION OF THREE-DIMENSIONAL FLOW STRUCTURE ON A LOW ASPECT RATIO WING SUBJECTED TO SINUSOIDAL PLUNGE MANEUVER

In order to gain further insight into the complex, three-dimensional unsteady flow structure on a plunging low-aspect-ratio wing, a technique of stereoscopic particle image velocimetry (SPIV) is employed, which yields the characterization of the flow structure in three-dimensional form. In this chapter, the time evolution of the flow structure and the generation of the complex vortex systems are interpreted in terms of phase-referenced three-dimensional streamline patterns, volume images of iso-Q, stacked contours of surface-normal vorticity and spanwise velocity, and vorticity projections in orthogonal directions.

In section 4.1, the experimental setup and methodology are introduced. The three-dimensional representation of the time evolution of the complex unsteady flow structure is addressed in section 4.2 in conjunction with the patterns of phase-averaged three-dimensional streamlines, iso-Q volumes, spanwise vorticity, surface-normal vorticity, and spanwise velocity. In section 4.3, the experimental flow visualizations are compared with the computational results obtained by the U.S. Air Force Research Laboratory, and the relationship between the flow structure and the lift coefficient is investigated. Finally, concluding remarks are given in section 4.4.

4.1 EXPERIMENTAL SYSTEM AND METHODOLOGY

4.1.1 Overview of Experimental Setup and Motion Control Mechanism

The experiments were performed in the same water channel as described in section 3.1. A rectangular wing model, shown in Figure 4.1a, and the same motion control mechanism, introduced in Chapter 2, were used for the stereo experiments. The freestream velocity was maintained at U = 90 mm/sec and the corresponding Reynolds number based on root chord C was 10,000. The wing was subjected to the pure plunging motion, which had a sinusoidal form, as illustrated in Figure 4.1b. The frequency and reduced frequency of the motion were respectively f = 0.28 Hz and $k = \pi fC/U$ = 1.0. The amplitude was h = 0.25C, corresponding to a peak-to-peak amplitude of 0.5C.

4.1.2 Stereoscopic Particle Image Velocimetry

A stereoscopic particle image velocimetry technique (SPIV) leads to determination of the quantitative, three-dimensional flow structure on a plane illuminated by a laser sheet. Two identical cameras, with an array of 1600 pixels × 1200 pixels, were employed on either side of the test section, to acquire all three components of the velocity on successive cross-flow planes, which were oriented perpendicular to the streamwise direction. In Figure 4.1c, a schematic of the stereo imaging system is shown. In order to reconstruct volume images, stereo images were acquired at various cross-flow planes. The dimensionless spacing between these planes was $\Delta x/C$ = 0.05. This reconstruction employed total of 21 evenly-spaced planes along the chord of the plate, and 4 additional planes located downstream of the

trailing-edge. A dual pulsed Yag laser system was operated at its maximum output of 120 mJ. The effective magnification of each camera provided 6.4 pixels/mm resolution in the plane of the laser sheet. Processing of the patterns of particle images via the cross-correlation technique, described in Chapter 2, yielded a maximum of approximately 6,223 velocity vectors within a cross-flow plane, and 130,683 vectors within the constructed volume of the flow.

An angular displacement configuration was used for the stereo imaging system. In order to obtain well focused images, the Scheimpflug condition was employed as described in section 2.3. Moreover, two prisms filled with distilled water were located on the side walls of the channel in order to reduce radial distortions arising from mismatch in refractive indices of air and water. Furthermore, a disparity mapping method, described in section 2.3, was employed during the calibration process, in order to correct the errors arising from misalignment between the calibration target and the measurement plane.

At each streamwise location, a phase-referencing technique was used to acquire 16 instantaneous images, which were averaged to generate phase-averaged images. Convergence was actually attained by averaging less than 16 images, i.e., only 7 images. The volume images of the flow structure were constructed from the three-dimensional phase-averaged velocities obtained on the cross-flow planes. The uncertainty involving in volume construction was assessed using a simulation technique which is explained in section 2.4. This solution allowed variation of the scale of the three-dimensional domain of vorticity, over the volume of interest. The representative uncertainty of the reconstructed velocity was 0.4%.

4.2 THREE-DIMENSIONAL REPRESENTATION OF TIME EVOLUTION OF FLOW STRUCTURE VIA STEREO IMAGING TECHNIQUE

4.2.1 Phase-Averaged Three-dimensional Streamline Patterns

Side, end and plan views of the three-dimensional streamline patterns are shown in Figure 4.2.1a and 4.2.1b. The figures display time sequence images at several successive phases of the plunging motion from $t/T = 0$ through $t/T = 0.5$, which are represented by the red colored circles on the motion graphs. The side view images and the corresponding end views of Figure 4.2.1a show the progressive development of a leading-edge vortex during the downstroke, and its formation into a pronounced three-dimensional structure during the initial stages of the upstroke. The evolution of these flow structures are also shown with the plan view images of the three-dimensional streamlines in Figure 4.2.1b.

Considering the sequence of side view images in the left column of Figure 4.2.1a, the formation of a large-scale leading-edge vortex system is evident during the downstroke. While the development of this leading-edge vortex looks two-dimensional in the side-view images, the corresponding end view images in the right column display a highly three-dimensional structure. The swirling streamline patterns at the tip regions of the wing correspond to the tip vortices. As shown in the first two rows of end view images, at $t/T = 0$ and 0.125, the leading-edge vortex is fairly uniform in spanwise direction at the central portion of the wing. However, it increases in scale, and at the plane of symmetry as it moves away from the surface of the wing during the final stages of the downstoke. At the end of downstroke, $\alpha_{eff} = 8.1°$ ($t/T = 0.25$), patterns of surface-parallel streamlines are evident near the surface of the wing.

As the wing plunges upward, the streamline patterns at t/T = 0.375 and 0.5 show that surface-parallel swirls thoroughly are located in the vicinity of the plane of symmetry. However, the side view images indicate that the central portion of the streamline patterns is inclined in the downstream direction.

The images in Figure 4.2.1b show the patterns of three-dimensional streamlines from the plan view perspective, and they conform to the streamline patterns in the side and end view images of Figure 4.2.1a. Moreover, during the initial stages of the upstroke, the downstream propagation of the streamline patterns, associated with the surface-parallel swirls, is clearly observed in the plan view images.

4.2.2 Phase-Averaged Iso-Q Volumes

Figures 4.2.2 shows surfaces of constant *Q*, whereby *Q* is defined as the positive second invariant of the velocity gradient tensor (deformation tensor). Surfaces of iso-*Q* correspond to constant values of the second invariant of the velocity gradient tensor, based on the *Q*-criterion defined by Wray et al (1988) and addressed by Green et al (2007), in relation to other criteria. Herein, the following form of the *Q* is employed:

$$Q = \frac{1}{2}\left[\Omega_{ij}\Omega_{ij} - \mathrm{S}_{ij}\mathrm{S}_{ij}\right] = -\frac{1}{2}\frac{\partial u_i}{\partial x_j}\frac{\partial u_j}{\partial x_i}$$

In essence, the *Q*-criterion is a measure of the magnitude of rotation, relative to strain. When *Q* is positive, rotation prevails over strain so that vortical structures can be identified as positive values of *Q* (Geers et al, 2005). Herein, the value of Q = 10. This value of *Q* was most compatible with the scale of the structures indicated by the patterns of streamlines, as well as the patterns of spanwise and surface-normal

vorticity. Generally speaking, as the value of Q increases, the scale of the structure indicated by Q decreases.

Phase-averaged images of iso-surfaces of Q-criterion are shown at eight successive phases of the oscillation cycle in Figure 4.2.2. Iso-Q surfaces display the evolution of three-dimensional flowfield on the upper surface of the wing during full period of the motion. At $t/T = 0$, where the wing has the maximum effective angle of attack, and has its maximum downward velocity, iso-surfaces of Q-criterion indicate a well-developed leading-edge vortex formation in the vicinity of the leading-edge, and a strong vortex formation along the wing tips. The initial stages of this leading-edge vortex formation, which has a fairly uniform formation in spanwise direction, are evident in the images of $t/T = 0.75$ and 0.875.

As the wing plunges downward, the leading-edge vortex and tip vortices lift away from the surface of the wing, and the flow field becomes highly three-dimensional as shown in the images of $t/T = 0.125$ and 0.25. The iso-Q surfaces, representing the leading-edge vortex, indicate that the leading-edge vortex system undergoes a substantial distortion, and evolves into a Λ-shaped formation at $t/T = 0.125$. At the end of downstroke, $t/T = 0.25$, the central portion of this vortex formation lifts further away from the wing surface, and its legs, pinned at the wing front corners, detach and move towards the plane of symmetry. With the starting of upstroke motion, at $t/T = 0.375$, the tip vortices on the upper side of the wing decay. At the earlier stages of the upstroke, the Λ-shaped vortex structure moves further downstream, and evolves into an arch-type structure. The names of "Λ-shaped" and "arch-type" of these three-dimensional vortex structures have been introduced by

Visbal (2011). As the wing moves upward, the arch-type vortex propagates downstream, and at t/T = 0.625, it arrives at the region of the trailing-edge. At the end of upstroke, t/T = 0.75, it detaches from the wing surface by forming a ring-like vortical structure, and sheds into the wake region as the wing starts its downward motion for the next plunging cycle.

4.2.3 Phase-Averaged Patterns of Spanwise Vorticity

Figure 4.2.3 shows slices of the vortex structure corresponding to contours of constant spanwise vorticity as a function of effective angle of attack, α_{eff}, ranging from α_{eff} = 34.7° (at t/T = 0) to -18.7° (at t/T = 0.5). The left and right columns of images represent respectively views looking downstream and upstream, which provide different perspectives of the patterns of spanwise vorticity. Blue colored contour levels represent the negative vorticity, which is in clockwise direction, while looking from these views.

Considering the first row of images in Figure 4.2.3, the spanwise variation of the vorticity concentrations is uniformly distributed along the leading-edge at α_{eff} = 34.7° (t/T = 0), except in the tip region. At α_{eff} = 27.5° (t/T = 0.125), the spanwise distribution of the leading-edge vortex system becomes nonuniform. Moreover, relatively larger scale patterns of vorticity appear near the plane of symmetry while much smaller-scale concentrations are evident as the tip of the wing is approached. At the end of downstroke, where α_{eff} = 8.1° and t/T = 0.25, the spanwise nonuniformity of the vorticity concentrations increases with the formation of Λ-shaped vortex structure at the central region of the wing. As the wing plunges upward, a cluster of large-scale,

high-magnitude spanwise vorticity layers is evident. A. They represent the spanwise vorticity distribution along the top region of the aforementioned arch-type vortex structure.

4.2.4 Phase-Averaged Patterns of Surface-Normal Vorticity

The streamline patterns shown in Figures 4.2.1a and 4.2.1b, as well as the iso-*Q* surfaces of Figure 4.2.2, indicate that aforementioned three-dimensional vortical structures, including the Λ-shaped and the arch-type, have a surface-parallel component of swirl at the different stages of the plunging cycle. In order to gain further insight into the evolution of these complex vortical structures, patterns of surface-normal vorticity contours on various surface-parallel planes are examined in Figure 4.2.4. Blue and red colored contour levels represent respectively negative (clockwise) and positive (counter-clockwise) vorticity.

At α_{eff} = 34.7° (t/T = 0), small-scale regions of surface normal vorticity are evident, at spanwise locations well inboard of the wing tips, and near the leading-edge. These concentrations are designated as *A* and *B* associated with the leading-edge vortex, and *C* and *D* associated with the tip vortices. As the wing plunges downward, the clusters of slices of surface-normal vorticity, designated as *A* and *B*, further develop and simultaneously move towards the plane of symmetry, as seen in the second and third row of images. However, the clusters designated as *C* and *D*, representing the tip vortices, begins decaying after α_{eff} = 27.5° (t/T = 0.125), and totally disappear on the upper surface of the wing during the upstroke.

The inboard clusters *A* and *B*, in the images of α_{eff} = 8.1° (*t/T* = 0.25) through α_{eff} = -18.7° (*t/T* = 0.5), indicate that the arch vortex yields layers of strong surface-normal vorticity due to the existence of significant surface-parallel swirling of the flow inside the legs of it. Furthermore, its legs stay attached on the surface of the wing as it continuously propagates downstream during the upstroke.

4.2.5 Phase-Averaged Patterns of Spanwise Velocity

Examination of patterns of spanwise velocity *w/U*, as shown in Figure 4.2.5, can provide further insight into the distinctive mechanisms of development of the patterns analyzed in the previous sections. In order to illustrate the behavior of the flowfield in spanwise direction, contours of constant *w/U* are shown on stacked surface-parallel planes. Directions of positive and negative *w/U* are designated respectively by yellow-red and blue contours; their directions are indicated by the arrows in the first row of images.

At α_{eff} = 34.7° (*t/T* = 0), contours *A* and *B* represent flow *towards* the plane of symmetry, which are compatible with the contours of surface-normal vorticity, and the patterns of streamlines described in the previous sections. The contour layers in the vicinity of the wing tips are associated with the tip vortices. At a later time of the downstroke, α_{eff} = 27.5° (*t/T* = 0.125), regions *A* and *B* have increased in scale, and moved further downstream as shown in the second row of images of Figure 4.2.5. Furthermore, small layers of spanwise velocity contours, designated as *C* and *D*, appear in the vicinity of the leading-edge, which indicate flow *away from* the plane of symmetry of the wing. At the end of downstroke, α_{eff} = 8.1° (*t/T* = 0.25), contours *A*

and *B*, and their adjacent layers *C* and *D*, are closer to one another, above the central region of the wing. The grouping of these layers is clearly due to the surface-parallel component of swirl associated with the aforementioned Λ-shaped vortex structure.

As the wing plunges upward, the large magnitude contours of spanwise flow are only apparent above the central region of the wing, as shown in the last two rows of images. These layers of prominent spanwise velocity contours are associated with the surface-parallel swirling flow inside the legs of the arch-type vortex. Considering the entire set of images in Figure 4.2.5, the mechanisms and rate of development of the patterns of *w/U*, as described in the foregoing, are consistent with the evolution of the patterns of surface-normal vorticity shown in the images of Figures 4.2.4.

4.2.6 Phase-Averaged Sectional Patterns of Flow Structure

In addition to the volume representations, given in the previous sections, comparing sectional cuts of velocity vectors, streamlines and constant spanwise velocity near the surface of the wing can provide critical insight into the onset and the development of the aforementioned complex flow structure. For this aim, a surface-parallel sectional cut, which is located a distance $y/C = 0.075$ above the surface of the wing, is extracted from the volume. In Figures 4.2.6a and 4.2.6b, the flow on these cross-sectional planes is characterized in terms of iso-surfaces of surface normal vorticity, velocity vectors, and patterns of streamlines with spanwise velocity contours. Each column of images in these figures represents the flow patterns at a selected time during the plunging cycle.

In the first column of Figure 4.2.6a, at $\alpha_{eff} = 34.7°$ ($t/T = 0$), the small portions of iso-surfaces of surface-normal vorticity, ω_y, indicate that small-scale swirls parallel

to the surface of the wing are evident near the leading-edge and well inboard of the wing tips. The patterns of associated velocity vectors on the cross-sectional plane, as shown in the third row of images, conform to these small-scale swirls, which form in the vicinity of the wing tips. Moreover, significant interaction is evident between leading-edge vortices and tip vortices in these regions, which can be viewed as the primary effect of movement of the flow *towards* the plane of symmetry. Furthermore, this interaction can also be one of the factors for formation of the aforementioned three-dimensional vortical structures, including the Λ-shaped and arch-type vortices, above the central region of the wing.

The second column of images in Figure 4.2.6a shows the flow patterns at a later time, where α_{eff} = 27.5° (t/T = 0.125). As the wing plunges downward, iso-surfaces of surface-normal vorticity increase in size, and expand towards the plane of symmetry. Furthermore, the patterns of velocity vectors display a relatively high velocity, jet-like flow near the inboard of the wing tips, through an alley between the well-defined vorticity concentrations of leading-edge and tip vortices.

Further clarification is provided by the patterns of sectional streamlines given in the bottom row of images in Figure 4.2.6a. Contours of constant spanwise velocity w/U are superposed on these streamline patterns. The foci F_a and F_b, which are located well downstream of the leading-edge, represent the small-scale swirls parallel to the surface of the wing, as addressed in the foregoing. The alleyway flow between the leading-edge and tip vortices is associated with a high value of spanwise velocity, of the order of 80% of the freestream velocity.

At α_{eff} = 34.7° (t/T = 0), the bifurcation lines, designated as BL^-, are located well downstream of the leading-edge. These lines converge towards the plane of symmetry, and form a stable node, designated as N_a, which represents the separation zone of the leading-edge vortex. On the other hand, diverging bifurcation lines BL^+, designated as positive bifurcation lines, extend through the alley between the leading-edge and the tip vortices, and finally intersect at a saddle point, designated as S_a, on the plane of symmetry, which indicates attachment of the flow. At the later time, α_{eff} = 27.5° (t/T = 0.125), the streamline patterns show that the scale of the surface parallel swirl patterns defined by the foci F_a and F_b increases, and their centers move towards the plane of symmetry. Due to the enlarged scale of the swirl patterns, positive bifurcation lines BL^+, and saddle point S_a are translated further downstream. Furthermore, new saddle points, designated as S_b and S_c, develop well downstream of the leading-edge.

Figure 4.2.6b shows the same type of sectional patterns as in Figure 4.2.6a, but at later times of the plunge motion, i.e. α_{eff} = 8.1° (t/T = 0.25) and α_{eff} = -11.6° (t/T = 0.375. Considering, first of all, the top two rows of images, the volume representations of surface-normal vorticity and streamlines, located over the central portion of the wing, correspond to the Λ-shaped and the arch-type vortical structures, described in the previous sections of this chapter. The representations of near-surface patterns of these structures are shown in the bottom rows of images.

The representations of velocity vectors, as shown in the third row of images of Figure 4.2.6b, display well-defined counter rotating adjacent swirl patterns in the

vicinity of the plane of symmetry. The centers of these swirl patterns correspond to the focal points, designated as F_a and F_b in the last row of images, showing the patterns of streamline, and spanwise velocity contours. Compared to the earlier times indicated in Figure 4.2.6a, the surface parallel swirl patterns defined by these foci propagate further downstream, and move towards the plane of symmetry as the wing plunges upward. The bifurcation lines, designated as BL^-, indicate spanwise flow away from the plane of symmetry near the leading-edge while they indicate a flow towards the plane of symmetry at earlier times. Moreover, the stable node, designated as N_a, converts to an unstable node at α_{eff} = 8.1° (t/T = 0.25). Then, it totally disappears at a later time, α_{eff} = -11.6° (t/T = 0.375), and yields to a saddle point S_d. Considering the patterns of spanwise velocity contours in the last row of images of Figure 4.2.6b, immediately upstream and downstream of each focus F_a and F_b, large magnitude spanwise flow is evident respectively in directions away from the plane of symmetry, and towards the plane of symmetry.

4.3 COMPARISON OF COMPUTED AND EXPERIMENTAL RESULTS

Comparison of the experimental flow visualizations, illustrated herein, with the computational simulations, obtained by the US Air Force Research Laboratory are presented in section 4.3.1. The computational simulations employ an extensively validated high-fidelity implicit large-eddy simulation (ILES) approach, which is described by Visbal and Rizzetta (2002) and Visbal et al. (2003). In addition to the flow visualizations, the lift coefficient C_L, obtained from the computations, is analyzed

in conjunction with the iso-*Q* surfaces of the flow structure in section 4.3.2, which yields the relationship between the flow structure and the lift coefficient.

4.3.1 Comparison of Flow Structure

Figure 4.3.1 shows the time-evolution of the iso-*Q* surfaces at four successive phases of the oscillation cycle, from α_{eff} = 34.7° (*t*/*T* = 0) through α_{eff} = -11.6° (*t*/*T* = 0.375). While the left column of images of Figure 4.3.1 corresponds to the experimental visualizations, the images in the right column display the computational visualizations. Considering all sets of images, and cross-comparing them, the experimental and high-fidelity simulations are found to be in good agreement with each other in terms of the evolution process of the unsteady three-dimensional flow structure during the oscillation cycle. More specifically, at α_{eff} = 34.7° (*t*/*T* = 0) and α_{eff} = 27.5° (*t*/*T* = 0.125), both indicate the generation of a leading-edge vortex system which is pinned at front corners of the wing. At a later time, α_{eff} = 8.1° (*t*/*T* = 0.25), this vortex detaches from the corners, and evolves into a Λ-shaped vortex structure as described in the foregoing. Finally, at α_{eff} = -11.6° (*t*/*T* = 0.375), as shown in the third row images, the legs of the Λ-shaped vortex move towards the plane of symmetry of the wing, and form an arc-type vortex structure.

The comparison shown in Figure 4.3.1 demonstrates that the time-evolution of the three-dimensional flow structure follows the same process, described above, for both experimental and computational cases. However, the computational visualizations include many small-scale structures of the iso-*Q* surfaces, which are not present on the experimental visualizations, because higher spatial resolution is used in

computations, and computational results are phase-averaged using a smaller number of instantaneous images compared to the experimental results. While 16 instantaneous images are employed for phase-averaging of the experimental visualizations, 6 instantaneous images are used in computations.

4.3.2 Relationship between Flow Structure and Aerodynamic Loads

As shown in the previous section, the experimental and computational visualizations of the unsteady three-dimensional flow structure show very similar characteristics. Therefore, it is possible to construct a relationship between the three-dimensional flow structure, obtained from the experiments, and the aerodynamics loads, calculated from the computations. In the middle of Figure 4.3.2, a graph shows the computed phase-averaged lift coefficient as a function of effective angle-of-attack for two different Reynolds numbers, i.e., 1,000 and 10,000, designated as a red dashed line and a black solid line respectively. The red dots on this graph represent the values of lift coefficient at selected phases, and the associated iso-Q surfaces of the flow structure are shown at these phases.

The lift significantly increases at the beginning of the downstroke, $\alpha_{eff} = 8.1°$ ($t/T = 0.75$), and reaches its peak immediately after the wing passes its maximum effective angle-of-attack, $\alpha_{eff} = 34.7°$ ($t/T = 0$), where the well-developed leading-edge vortex system (dynamic stall vortex system) is evident on the wing. With the detachment of this vortex system from the corners of the wing, the lift starts dramatically decreasing at $\alpha_{eff} = 27.5°$ ($t/T = 0.125$), and continues to decrease during the first half of the upstroke. Right after the arch-type vortex reaches near the trailing-

edge at α_{eff} = -18.7° (t/T = 0.5), the lift tends to increase, and keeps increasing during the rest of the upstroke.

Furthermore, the graph indicates a smooth lift coefficient distribution during the oscillation cycle, and shows no evidence of deep stall, which may be due to the high value of reduced frequency yielding significant non-circularity lift contribution. Moreover, the computations indicate that the effect of Reynolds number on the lift is insignificant (Visbal, 2011).

4.4 CONCLUDING REMARKS

The complex unsteady flow structure over a plunging low aspect ratio rectangular wing is investigated using techniques of stereoscopic particle image velocimetry. The wing is subjected to a sinusoidal plunging motion at a reduced frequency $k = \pi fC/U$ = 1.0 and amplitude h = 0.25C. The time sequences of the volume images of the flow structure are interpreted in conjunction with three-dimensional streamline patterns, iso-Q surfaces, contours of vorticity projections in orthogonal directions, spanwise velocity, velocity vectors, and streamline topology on cross-sectional planes.

First of all, this investigation shows that the flow patterns on plunging low aspect ratio wings have complex, unsteady, highly three-dimensional characteristics, which set them apart from the classical, quasi two-dimensional flows. These unique characteristics of the time evolution of the flowfield involve:

1. Presence of a pronounced axial flow in the nascent leading-edge vortex during its initial stages of development (first half of the downstroke).

2. Evolution of the leading-edge vortex system into a Λ-shaped formation, whose legs are pinned at the front corners of the wing, observed at α_{eff} = 27.5° (t/T = 0.125).

3. Detachment of the Λ-shaped vortex from the corners of the tip, movement of its legs towards the plane of symmetry, and formation of the surface-parallel swirls near the surface of the wing, which is evident at the end of downstroke α_{eff} = 8.1° (t/T = 0.25).

4. Evolution of the Λ-shaped formation into an arch-type vortex structure during the initial stages of the upstroke.

5. Downstream propagation of the arch vortex, and movement of its legs toward the wing centerline during the upstroke.

6. Reconnection of the legs of the arch vortex at the end of upstroke, and its shedding from the trailing-edge in a ring-like form as the next plunging cycle begins.

In addition to the flow structure described above, the wing tip vortices follow a process including formation, vortex breakdown, total collapse, and reformation at various stages of the plunging cycle, which have been also observed in the computational results (Visbal, 2011).

Furthermore, the experimental flow visualizations are compared with the high resolution computational visualizations, performed by the US Air Force Research Laboratory. The patterns of the flow structure show same characteristics for both studies. In addition to the flow visualizations, the relationship between the three-dimensional flow structure and lift coefficient is investigated. A smooth lift coefficient

distribution is observed, and no evidence of deep stall is found during the oscillation cycle. Moreover, the computations indicate that the Reynolds number has a limited effect on the lift coefficient.

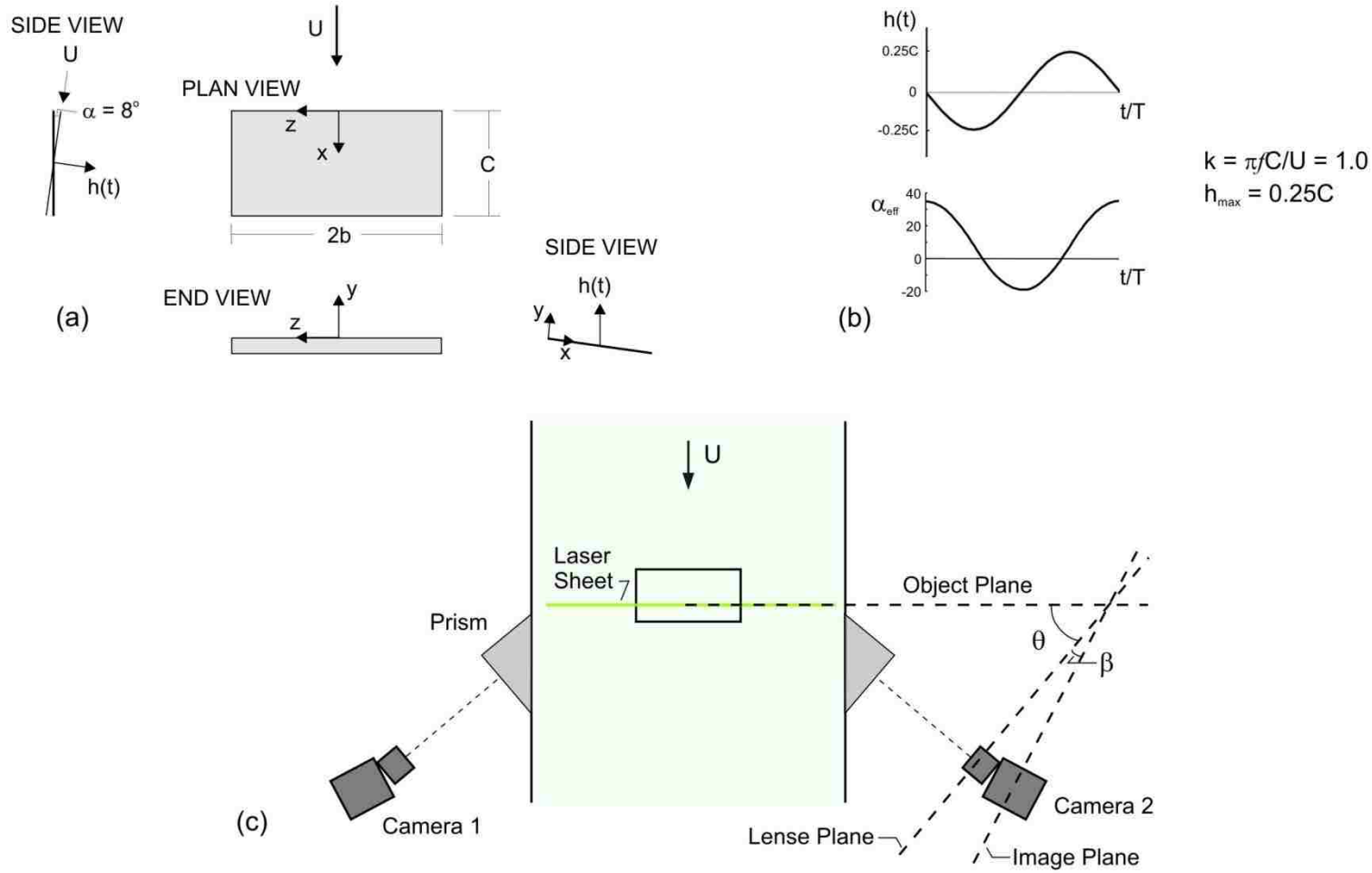

Figure 4.1: (a) Overview of wing configuration; **(b)** plunge schedule of wing motion; **(c)** quantitative imaging system.

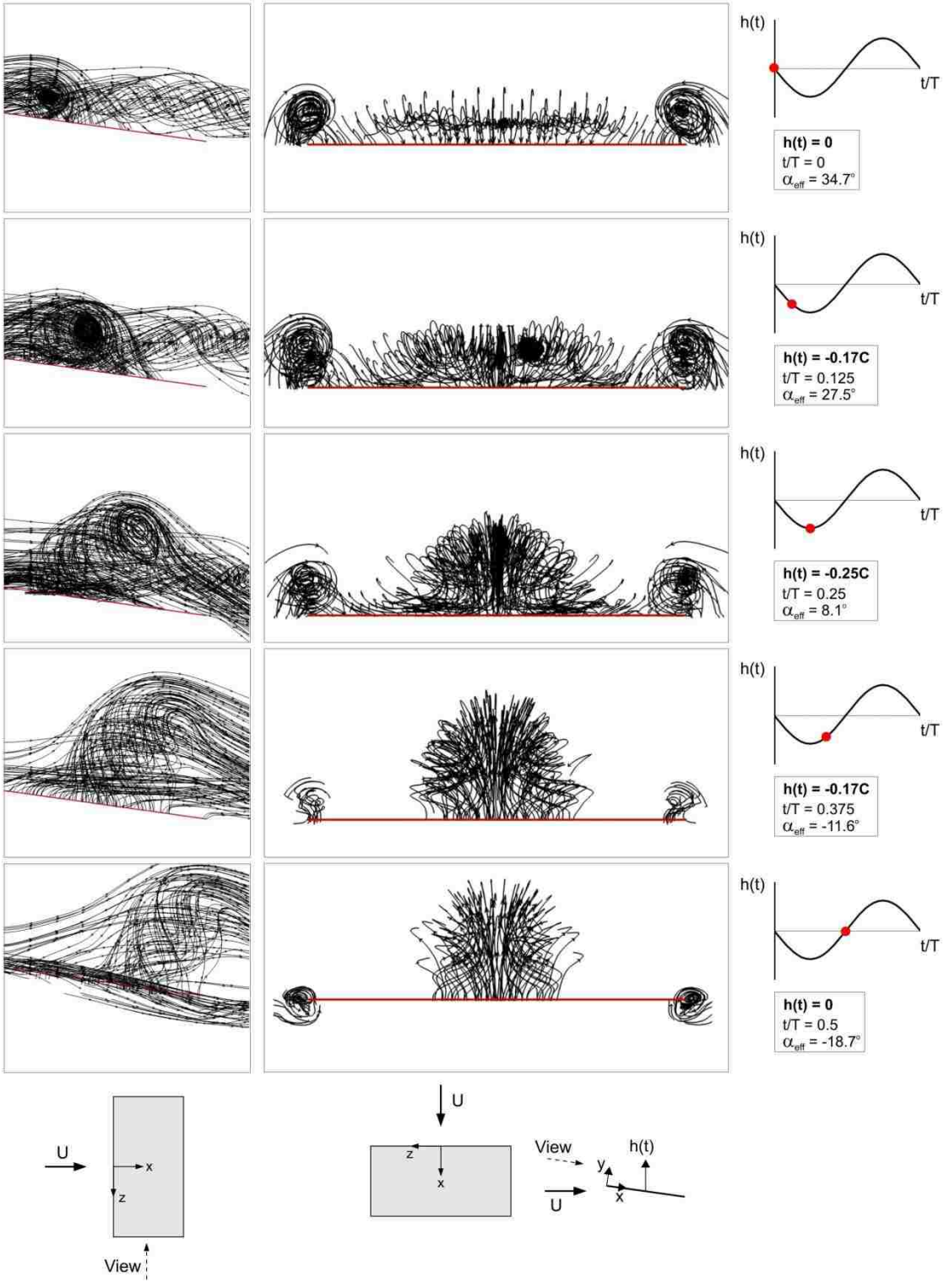

Figure 4.2.1a: Side (left column) and end (right column) views of three-dimensional streamline patterns as a function of time.

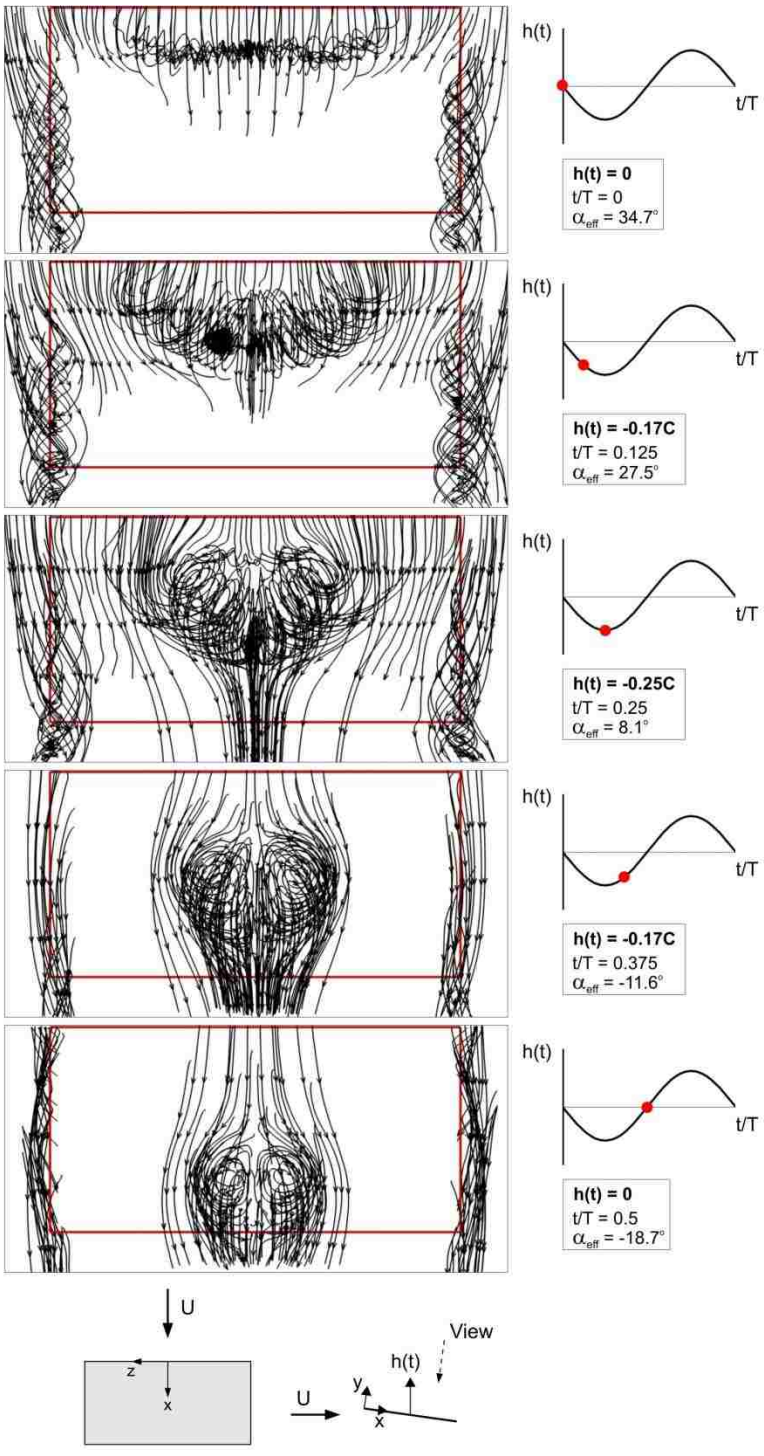

Figure 4.2.1b: Plan views of three-dimensional streamline patterns as a function of time.

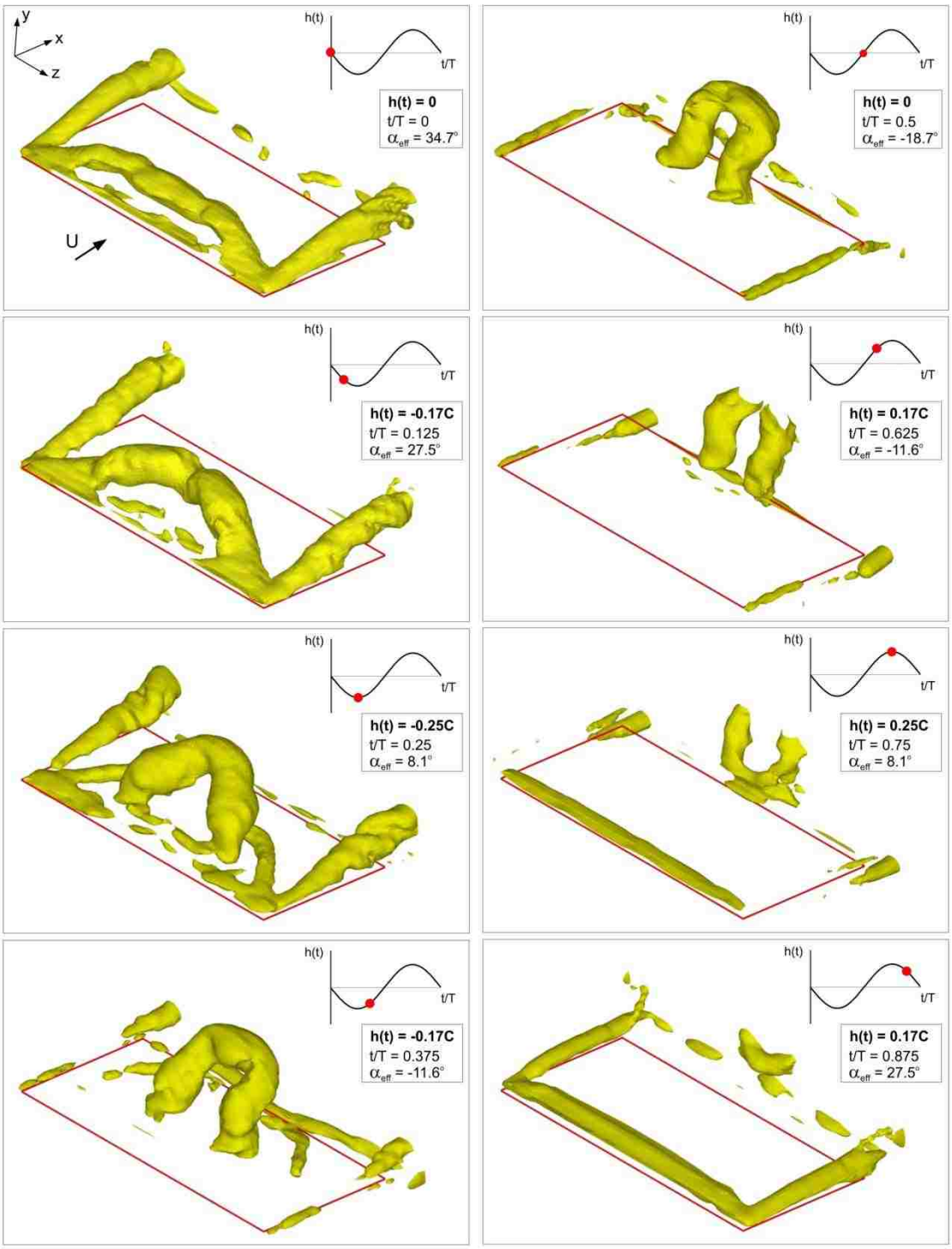

Figure 4.2.2: Volumes of iso-Q as a function of time. Views are in the downstream direction, looking towards the leading-edge of the wing.

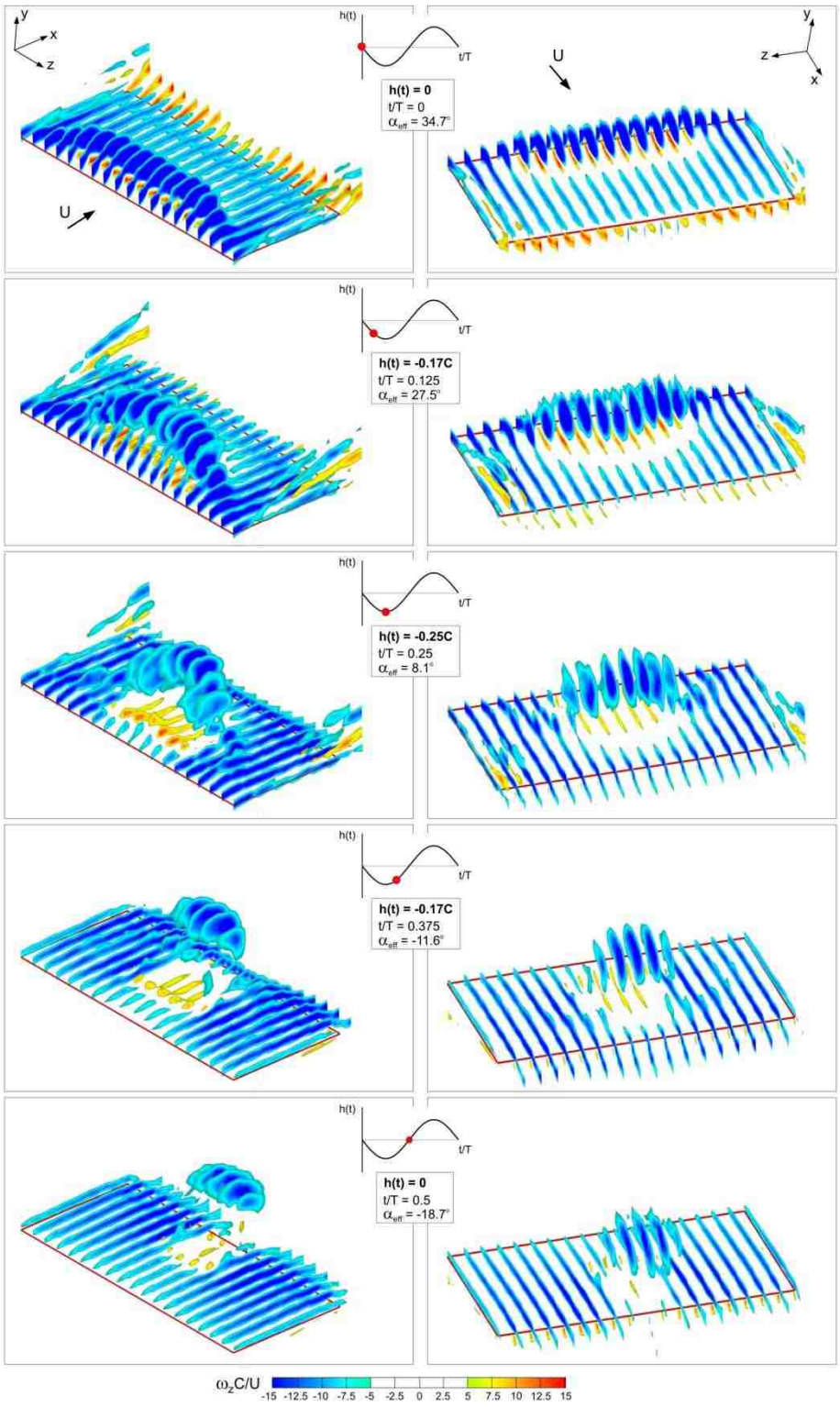

Figure 4.2.3: Sectional cuts of spanwise vorticity as a function of time. Views are in the downstream direction, looking towards the leading-edge (left column), and in the upstream direction, looking towards the trailing-edge of the wing (right column).

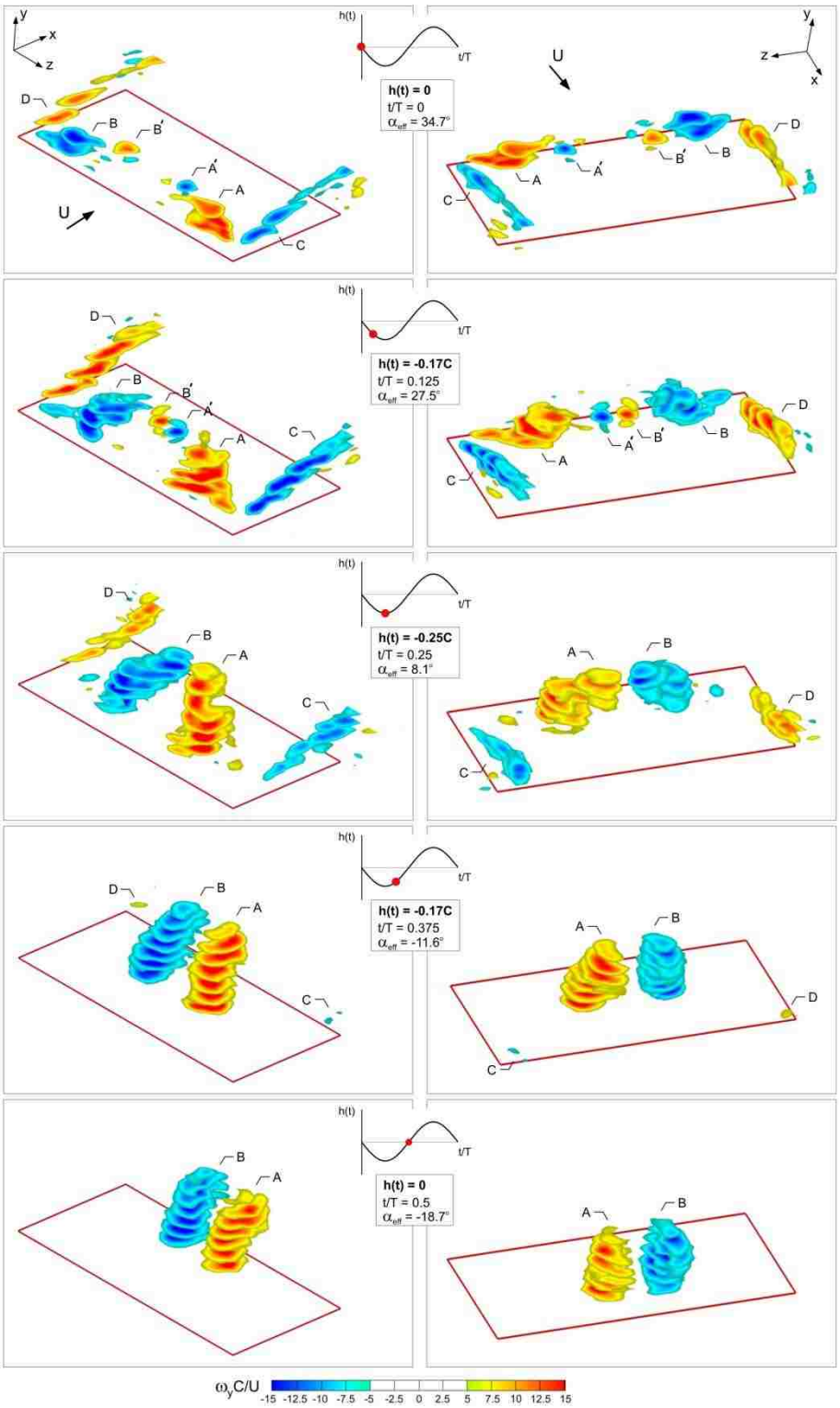

Figure 4.2.4: Sectional cuts of surface-normal vorticity as a function of time. Views are in the downstream direction, looking towards the leading-edge (left column), and in the upstream direction, looking towards the trailing-edge of the wing (right column).

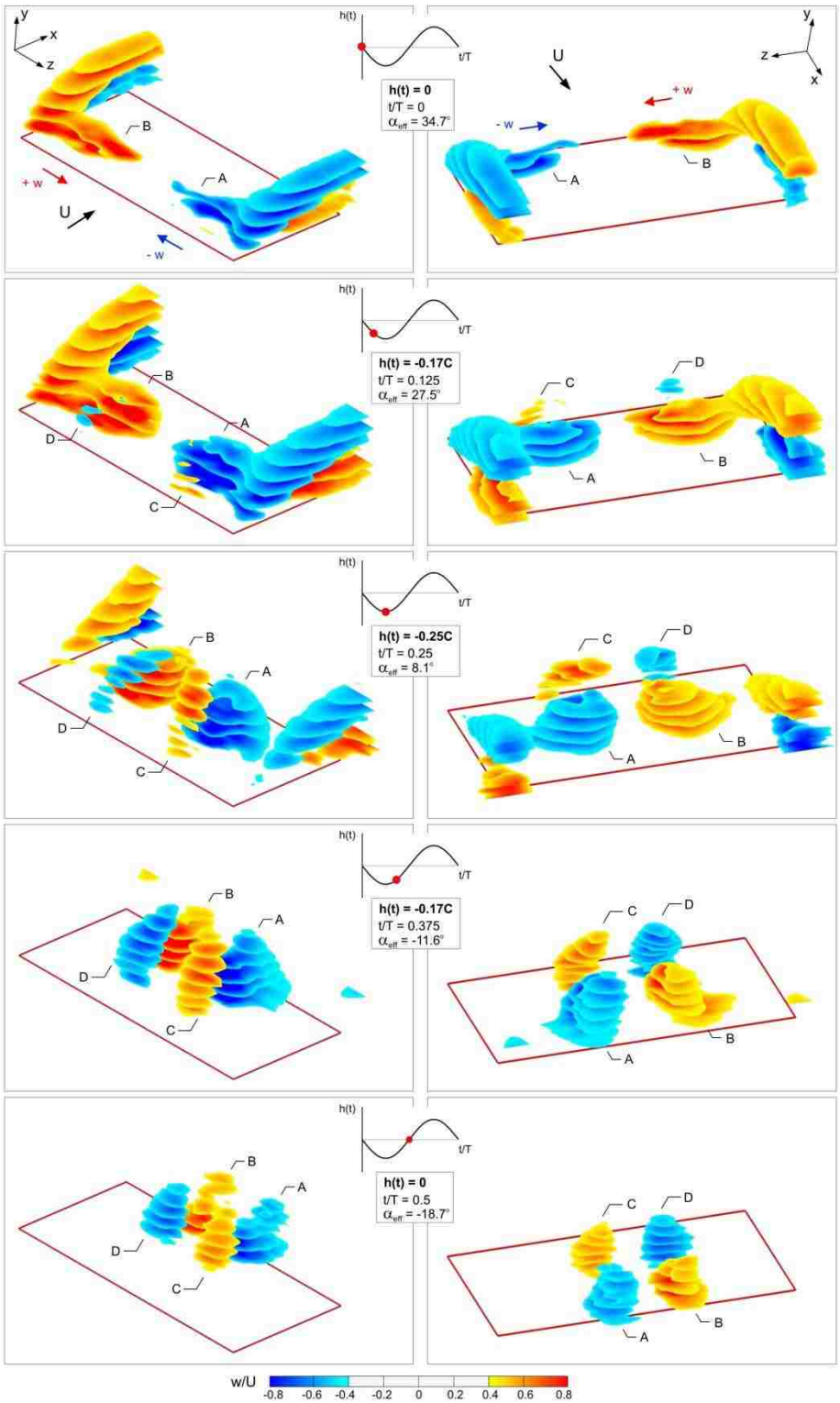

Figure 4.2.5: Slices of contours of constant spanwise velocity as a function of time. Views are in the downstream direction, looking towards the leading-edge (left column), and in the upstream direction, looking towards the trailing-edge of the wing (right column).

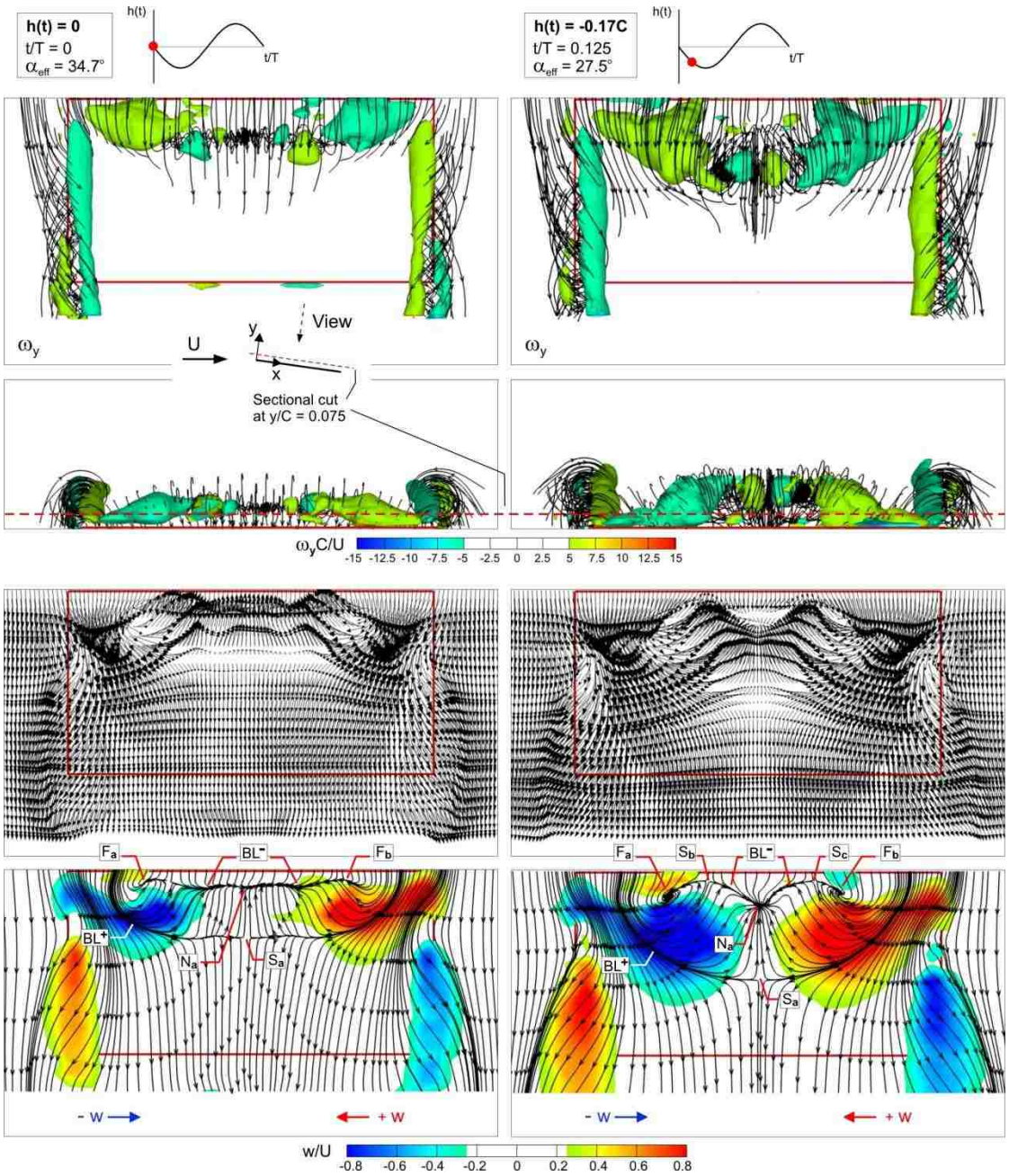

Figure 4.2.6a: Volumes of surface-normal vorticity superposed on three-dimensional streamlines (top two rows of images), velocity vectors (third row), and streamline topology with superposed contours of constant spanwise velocity (fourth row).

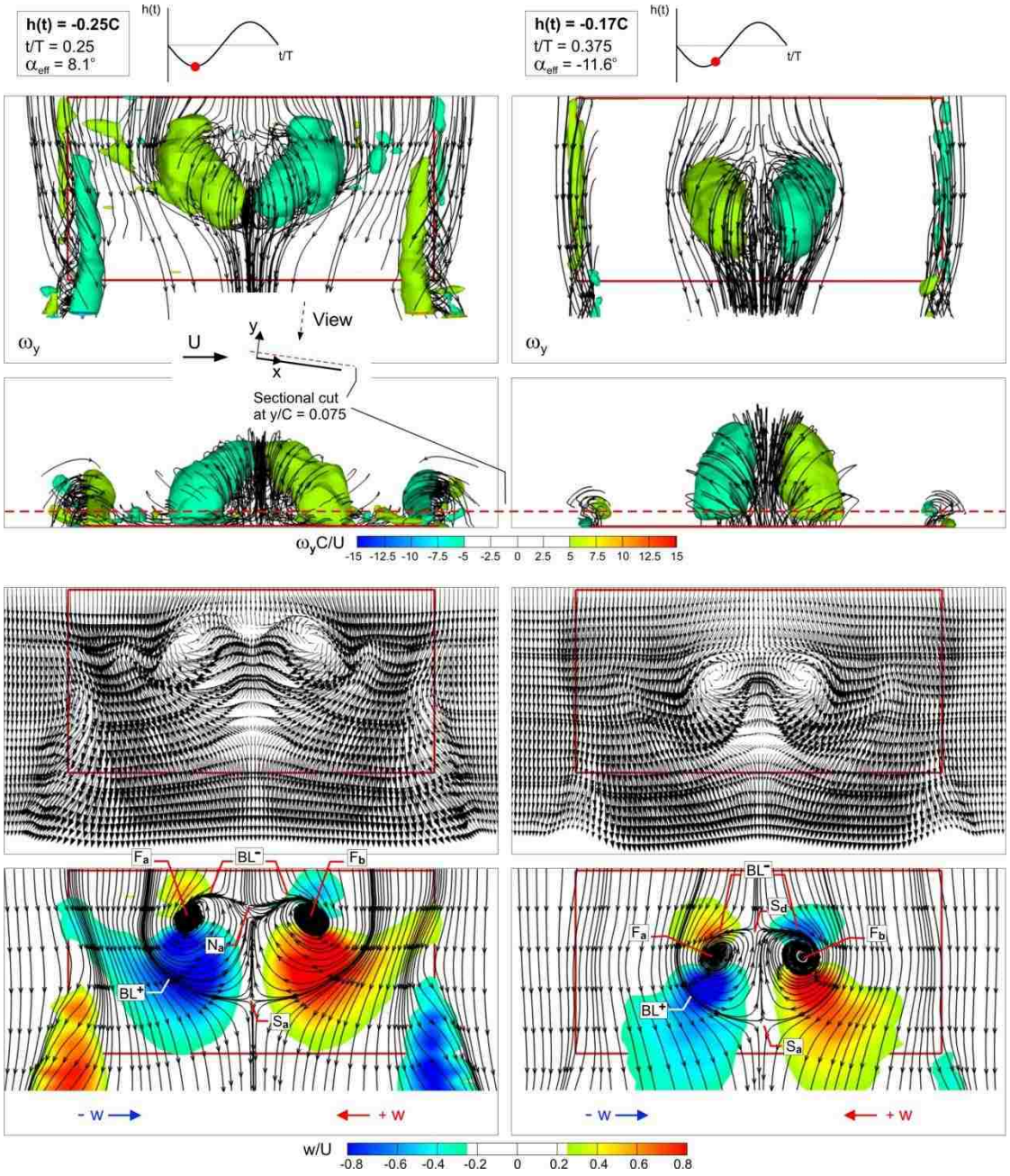

Figure 4.2.6b: Volumes of surface-normal vorticity superposed on three-dimensional streamlines (top two rows of images), velocity vectors (third row), and streamline topology with superposed contours of constant spanwise velocity (fourth row).

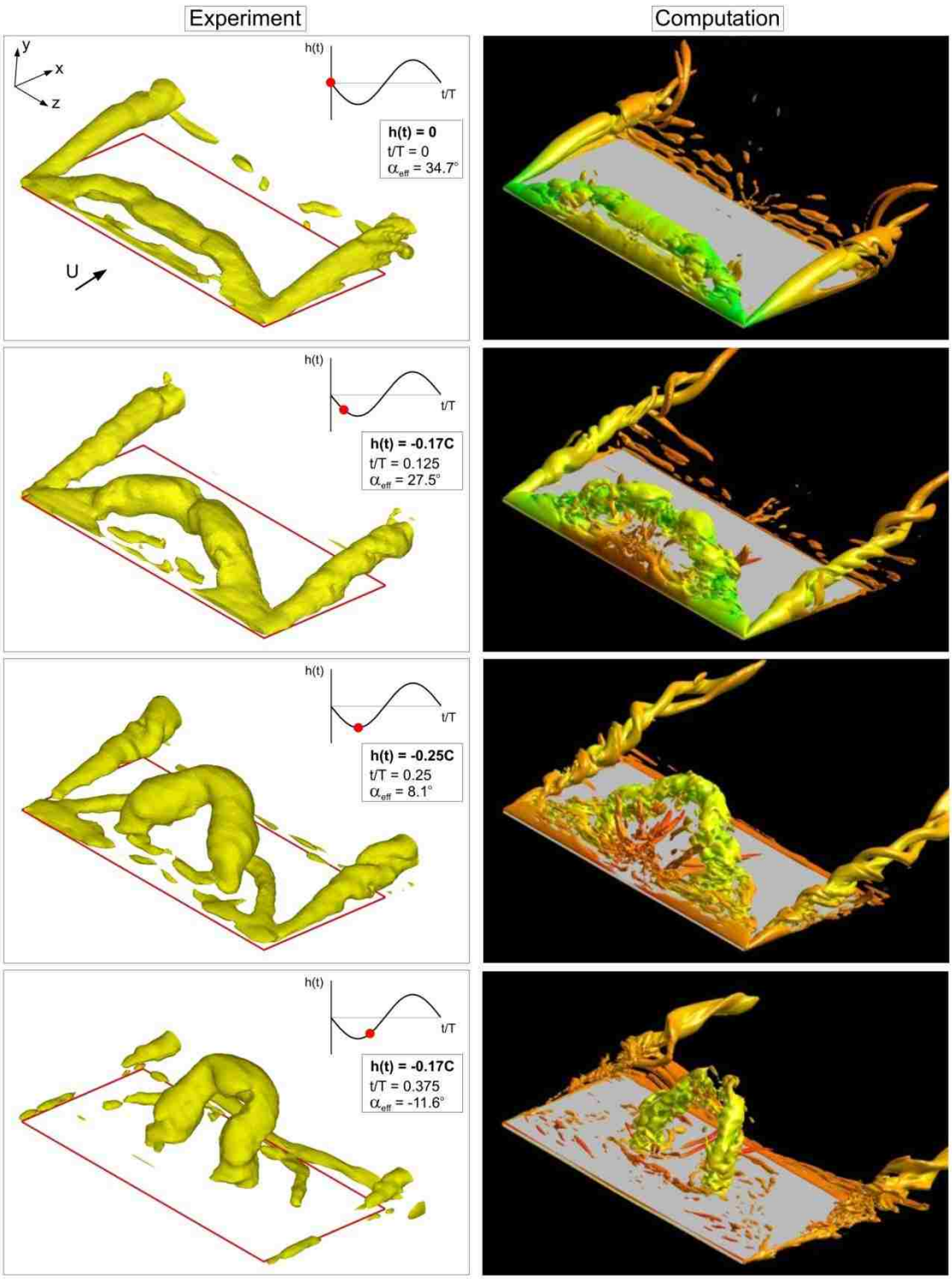

Figure 4.3.1: Comparison of volumes of iso-Q obtained from experimental (left column) and computational (right column) results (Visbal, 2011).

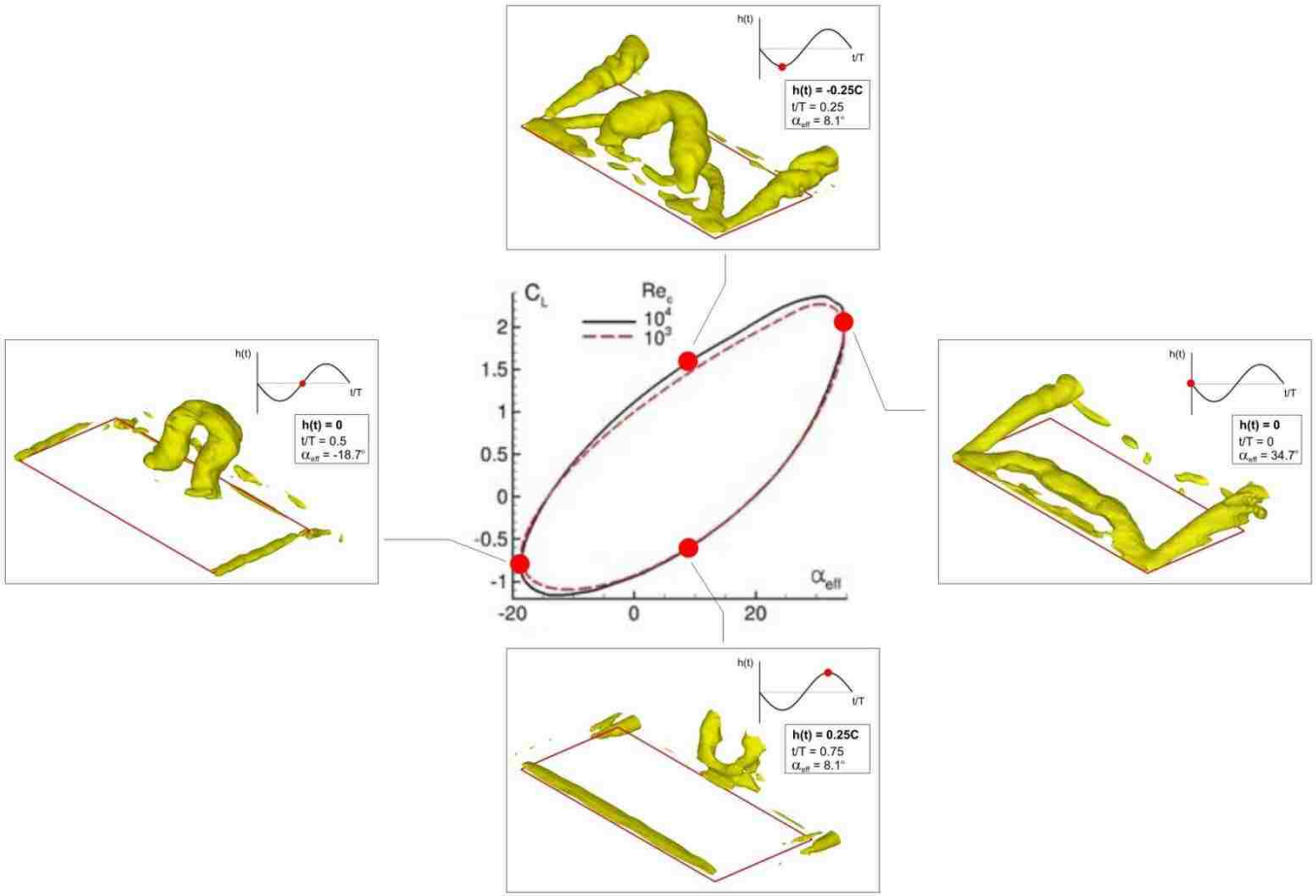
h(t)
t/T
h(t) = -0.25C
t/T = 0.25
α_{eff} = 8.1°
C_L
Re_c
10^4
10^3
2
1.5
1
0.5
0
-0.5
-1
-20
0
20
α_{eff}
h(t) = 0
t/T = 0.5
α_{eff} = -18.7°
h(t) = 0
t/T = 0
α_{eff} = 34.7°
h(t) = 0.25C
t/T = 0.75
α_{eff} = 8.1°

CHAPTER 5

THREE DIMENSIONAL REPRESENTATION OF TIME EVOLUTION OF FLOW STRUCTURE ON VARIOUS LOW ASPECT RATIO WING CONFIGURATIONS SUBJECTED TO PITCH UP MANEUVER

In this chapter, the three-dimensional flow structure and topology on low aspect ratio wing configurations subjected to a smoothed linear ramp-like pitching motion is addressed. A technique of stereoscopic particle image velocimetry and dye visualization are used to determine the flow structure. Four different configurations of wing planforms, described in section 2.2, are employed to investigate the onset and development of the three-dimensionality of the flow structure. A technique of dye visualization reveals effects of variation of the dimensionless pitch rate $K = \dot{\alpha}C/2U$ on the development of the flow structure during the maneuver.

In section 5.1, the experimental setup and methodology are explained. The distinctive stages of flowfield evolution on various wing configurations with different pitch rates are qualitatively addressed in section 5.2. In section 5.3, the three-dimensional flowfield and the time evolution of the vortical patterns are quantitatively characterized in terms of phase-referenced three-dimensional streamline patterns, volume images of iso-Q, and vorticity projections in orthogonal directions for both elliptical and rectangular wing configurations. Finally, concluding remarks are given in section 5.4.

5.1 EXPERIMENTAL SYSTEM AND METHODOLOGY

5.1.1 Overview of Experimental Setup and Motion Control Mechanism

An overview of the experimental setup is shown in Figure 5.1.2. Four different wing configurations, indicated as A, B, C and D, were employed. They are shown in the plan and side views of Figure 5.1.1 (a). All had a low aspect ratio AR = 2, a root chord C = 101.6 mm and a total span $2b$ = 203.2 mm. The models were thin brass plates with a thickness of t = 1.59 mm, corresponding to t/C = 0.016. All edges of the plates of the plates had a semicircular contour. The freestream velocity was maintained at U = 90 mm/sec and the corresponding Reynolds number based on root chord C was 10,000.

The wing motion, represented in Figure 5.1.1 (b), was a linear pitch up from angle of attack α = 0 to 45°, about the quarter-chord of the wing, x_p/C = 0.25. At α = 0° and 45°, the prescribed motion was rounded according to the smoothing method explained in section 2.2.2.

The dye experiments were performed for three different values of time scale 1.0, 2.0, and 4.0 C/U in order to investigate the pitch rate effect on the flowfield evolution. The corresponding pitch-up ramp rates were $\dot{\alpha}$ = 0.696, 0.348, and 0.174 rad/sec, and reduced pitch rates, based on chord C were $K = \dot{\alpha}C/2U$ = 0.393, 0.196, and 0.098 respectively. The pitch pivot point of the plate was maintained at the location x_p/C = 0.25, during the pitch-up motion.

5.1.2 Stereoscopic Particle Image Velocimetry

In order to determine the quantitative, three-dimensional flow structure on the maneuvering wings, stereoscopic particle image velocimetry technique (SPIV) was employed. An angular displacement configuration was used, as shown in the schematic of Figure 5.1.2. Two identical cameras were employed to acquire three components of the velocity on a cross-flow plane perpendicular to the streamwise direction.

The water was filtered by a one-micron filter system, and seeded with 12 micron metallic-coated hollow plastic spheres, with sufficiently high density such that the interrogation window of 32 pixels × 32 pixels typically contained about 15-20 particle images. The laser sheet of 1 mm thickness was generated by a dual pulsed Nd:Yag laser system having a maximum output of 120 mJ. Images were captured using two cameras with an array of 1600 pixels × 1200 pixels. The effective magnification of each camera provided 6.4 pixels/mm resolution in the plane of the laser sheet. During the maneuver, images were acquired at 15 unique positions of the wing from t = 0 to 5.6 C/U. The patterns of particle images were processed using a frame-to-frame cross-correlation technique, and a standard overlap of 50% was employed, in accord with the Nyquist criterion as described in section 2.3. As a consequence, the spatial sampling separation of the velocity data was 2.5 mm, yielding a maximum of approximately 6,223 velocity vectors within a crossplane, and 130,683 vectors within the constructed volume of the flow.

For the stereo configuration shown in Figure 5.1.2, the object plane is not parallel to the lens plane. It is therefore difficult to obtain well focused images. This problem was overcome by employing the Scheimpflug condition as described in section 2.3.3. Moreover, in order to reduce radial distortions arising from mismatch in refractive indices of air and water, two prisms filled with distilled water were located on each side wall of the channel, as shown in Figure 5.1.2. Furthermore, a disparity mapping method, described in section 2.3.3, was employed during the calibration process, in order to correct the error arising from misalignment between the calibration target and the measurement plane. For this stereo configuration, the rms residual pixel displacement error generated during the interpolation phase of the stereo reconstruction was calculated as 0.103 pixels.

5.1.3 Instantaneous vs. Phase-averaged Images

During the SPIV experiments, the laser sheet was oriented orthogonal to the direction of the freestream. In order to reconstruct volume images, images were acquired at 21 evenly-spaced locations along the chord of the plate. The dimensionless distance between each plane was $\Delta x/C = 0.05$. At each streamwise location, a phase-referencing technique was used to acquire 15 instantaneous images, which were then averaged, in order to provide phase-averaged images. Figure 5.1.3 shows the instantaneous and averaged flow structure at two different cross-flow planes where $x'/C = 0.13$ and 0.43. For $x'/C = 0.13$, the left column compares layouts of instantaneous and averages of 15 images respectively in terms of spanwise velocity, velocity vector, and vorticity. In the right column, the image layouts show the instantaneous and averaged patterns at $x'/C = 0.43$. Located at the bottom of Figure

5.1.3, a graph represents averaged vorticity values with respect to the number of images averaged in a selected area which is designated by a square on the flowfield. As shown in this graph, averaging of 10 or more images yields a value of phase-averaged vorticity within less than 1.5% of the asymptotic value. Using the three-dimensional phase-averaged velocities on each of the planes, volume images of the flow structure were determined using software developed in-house, as explained in section 2.4. For the parameters employed in the present investigation, the representative uncertainty of the reconstructed velocity was 0.4%.

5.2 FLOWFIELD EVOLUTION DUE TO PITCHING MOTION ON VARIOUS WING PLANFORMS WITH DIFFERENT PITCH RATES

5.2.1 Patterns of Leading-edge Vortex Formation on Various Wing Planforms

For the case of highest reduced pitch rate $K = \dot{\alpha}C/2U = 0.393$, development of the flow patterns and leading-edge vortex formation is indicated by the plan views and side views of dye visualization respectively in Figure 5.2.1a and Figure 5.2.1b. Images of each column show sequential states of flowfield formation on different wing planform. The time sequence of images is designated with angle of attack α and dimensionless time C/U on each image of the left column. The instantaneous angle of attack is indicated by a dot on the schematic of the pitching schedule (α versus time t) given below the left column.

Distinctive types of flow patterns are evident during the maneuver and the first stages of relaxation for each type of wing planform. In the first row of images of Figure 5.2.1a and Figure 5.2.1b, corresponding to $\alpha = 22.5°$, both the plan and side views indicate the incipient formation of a leading-edge vortex on each wing

planform. Subsequently, at α = 33.75°, as indicated in second row of images, a small vortex evident in the vicinity of the leading-edge of each type of wing configuration. The corresponding plan views show inboard-oriented axial flow, designated by the red arrows on the images, through the center of the leading-edge vortex towards the plane of symmetry only on the rectangular, type B and C wing planforms. Moreover, dye patterns indicate that the inboard-oriented axial flow originates from the tips of the leading-edge which is a unique characteristic to wing geometry.

In the third row images of Figure 5.2.1b, the side view of the leading-edge vortex shows a substantial increase in scale at the termination of the maneuver where α = 45° and t = 1.0 C/U. Correspondingly, due to the axial flow through the leading-edge vortex, the plan views in Figure 5.2.1a show further movement of dye patterns towards the plane of symmetry on each wing planform, except on the elliptical wing. In contrast, due to lack of this type of axial flow over the elliptical wing, the leading-edge vortex system is relatively more uniform as seen in the first three rows of images.

At a larger value of convective time, t = 1.25 C/U, in the fourth row of images, both plan and side views show the first stage of relaxation of the flow patterns after the end of the maneuver. At this instant of time, plan views indicate that the pattern of axial flow through the leading-edge vortex finally reaches the plane of symmetry. From the corresponding side view images in Figure 5.2.1b, it is clearly seen that the leading-edge vortex continues to grow in size. At a later time of the relaxation process t = 1.75 C/U, both plan and side views show that the three-dimensional leading-edge vortex matures to a larger scale and undergoes substantial distortion due to interaction of opposing flow patterns on the central portion of the

wings. Following this interaction, a substantial change occurs in the direction of the axial flow through the leading-edge vortex of the wings. The fronts of the dye marker indicate a flow away from the plane of symmetry, designated by the blue arrows on the plan view images shown in the last row of Figure 5.2.1a.

Considering the entire set of images of Figure 5.2.1a, and cross-comparing them, it can be seen that the sequential states of the flow field development are similar on the rectangular, type B and C wing planforms. First, all show presence of the axial flow through the leading-edge vortex during the pitching maneuver. Second, a sudden change in the direction of the axial flow through the leading-edge after the end of maneuver is a common feature for these three different wing configurations. However, during the relaxation process, the leading-edge vortex on the rectangular wing and the type B wing occupies relatively large area, and the tip vortices on these wings are more prominent compared to the vortical structures on type C and the elliptical wings.

Comparing the side views of dye patterns in Figure 5.2.1b, it is evident that the leading-edge vortex is closer to the surface on the type C wing and the elliptical wing during the maneuvering and the relaxation process. Furthermore, on the rectangular wing and the type B wing, the leading-edge vortex moves further upward off the wing surface, particularly at the later time $t = 1.75\ C/U$. This phenomenon can be influenced by the tip vortices on the development of the leading-edge vortex on finite-span wings. As can be seen in the last row images of the plan and side views, relatively larger leading-edge vortex formation appears on the rectangular and the type B wing planforms, where strong interaction between leading-edge and tip vortices is evident. On the other hand, the leading-edge vortex develops close to the surface on

the elliptical wing; the reason may be lack of a strong tip vortex, which does not deflect toward the leading-edge vortex during the maneuver.

For a lower value of reduced pitch rate $K = \dot{\alpha}C/2U = 0.196$, Figure 5.2.1c shows plan views of sequential states of the flow field at five different instants of time from 1.0 to 3.5 *C/U*. In the first row of images, corresponding to $\alpha = 22.5°$ (1.0 *C/U*), the initial stage of leading-edge vortex formation is evident on each wing planform. At this instant, pronounced, inboard-oriented axial flow occurs through the center of the leading-edge vortex towards the plane of symmetry. It is observed only on the rectangular and the type B wing planforms. At a later time $t = 1.5$ *C/U*, and at $\alpha = 33.75°$, inboard-oriented axial flow is also observed in the vicinity of the mid-span of the type C wing planform. However, this type flow pattern is not evident on the elliptical wing until termination of the maneuver.

The third row of images of Figure 5.2.1c shows flow patterns at the end of pitch-up maneuver for $t = 2.0$ *C/U* and $\alpha = 45°$. At this instant, first stage of interaction of the opposing flow patterns occurs on the central portion of the wings A, B and C. Immediately following this interaction, the direction of the flow along the leading-edge is reversed, and a flow occurs in the direction away from the plane of symmetry. However, this type of interaction occurs with a delay on the elliptical wing. This delay is most likely due to the weaker formation of axial flow, which is just evident at the end of maneuver. At later times of the relaxation process, $t = 2.5$ and 3.5 *C/U*, in the fourth and fifth rows of images, the three-dimensional vortex matures to a larger scale and undergoes substantial distortion.

Analyzing the entire set of images of Figure 5.2.1c, it can be seen that flowfield evolution is similar on the rectangular, type B, and type C wing planforms. These similarities include pronounced, inboard-oriented axial flow through the center of the leading-edge vortex during the maneuver, interaction of opposing flow patterns at the termination of the maneuver, and formation of a prominent tip vortex. Furthermore, the dye patterns indicate similar flow structure on each type of wing at the later instant of time as shown in the fifth row of images, although completely different flowfield evolution is evident on the elliptical wing during the maneuver.

For the lowest value of reduced pitch rate studied herein, $K = \dot{\alpha}C/2U = 0.098$, time evolution of the flowfield is illustrated in Figure 5.2.1d. The pronounced inboard-oriented axial flow is still evident during the first stages of the pitching maneuver on the rectangular, type B, and type C wing planforms. The aforementioned collision of opposing flow patterns in the vicinity of mid-span occurs before the termination of the maneuver on each type of wing planform, i.e., at angle-of-attack of $\alpha = 28.1°$ for the rectangular, type B, and type C wing planforms, and at a higher angle-of-attack for the elliptical wing.

5.2.2 Effect of Wing Geometry

Considering the whole set of images in Figures 5.2.1a through 5.2.1d, and cross-comparing them, the effects of wing geometry on the leading-edge vortex formation and flowfield evolution can be further clarified. The dye patterns show that development of the three-dimensional flow field on each wing is evident at any instant of time, even for low values of pitch rate. However, each type of wing planform has its distinctive stages of leading-edge and tip vortex formation. While formation of the

vortical structures around the corners of the leading-edge on the rectangular and type B wing planforms is evident during the first stages of the maneuver, there are no discontinuities in the vortex sheet emanating from the leading-edge and the tips on the type C and elliptical wings. Moreover, for all values of pitch rate studied herein, the pronounced, inboard-oriented axial flow through the center of the leading-edge vortex, and subsequent interaction of these axial flows is observed only on the rectangular, type B, and C wing planforms during the early stages of the maneuver. For the elliptical wing planform, more organized development of the leading-edge vortex is evident, and a weak three-dimensional interaction between the well-developed leading-edge vortices only appears later in time. Furthermore, due to the absence of sharp wing tips for this planform, the vortical structures from the leading-edge develop with an ordered form as they convect downstream. Additionally, the dye patterns on the rectangular wing indicate that the leading-edge vortex spreads more downstream on the rectangular wing for any case of pitch rate.

In spite of distinctly different leading-edge and tip vortex evolution on each planform, a similar flow structure is still evident during the final stages of the maneuver, which involves a relaxation process. This structure includes large-scale, counter-rotating adjacent swirl patterns on both sides of the plane of the symmetry as designated by the white colored, circular lines in the figures. But, a similar state of the flow patterns appears at different instants of time and angle of attack, depending on the pitch rate. The effect of pitch rate on the flowfield evolution is further investigated in the following section.

5.2.3 Effect of Pitch Rate

In order to investigate the effects of pitch rate on the flowfield evolution, different values of reduced pitch rate $K = \dot{\alpha}C/2U$ = 0.393, 0.196, and 0.098 are considered for each wing planform. The sequence of images in Figure 5.2.1a through Figure 5.2.1d respectively shows flowfield evolution for any pitch rate studied herein. Cross-comparing the sequential states of flow patterns given in those figures, it is clearly seen that leading-edge and tip vortex formations are unique to each wing geometry. It is also evident from the plan view images that these leading-edge vortices display similar primary flow events, even with variation of pitch rate. Generally speaking, the major features of the flow structure are similar for variation of reduced frequency. But, this variation simply induces a shift in time of occurrence of the sequence of three-dimensional events.

In order to gain a deeper understanding of the role of pitch rate on the aforementioned flow fields, both plan and side view images of the flow patterns are compared for different values of reduced pitch rate in Figure 5.2.3. With the hypothesis that the LEV pattern exhibits similarity at different values of K, examination of movies yielded the LEV patterns at the values of angle of attack α and reduced frequency K indicated in Figure 5.2.3. In essence, the effect of increasing K is to advance occurrence of the LEV pattern to smaller values of C/U, but to delay it along the indicated pitching schedule. The time shift caused by this delay is represented by a reference pattern of the leading-edge vortex development, which is taken to occur at t =1.25 C/U, and angle of attack α = 45°, i.e., the three -dimensional form of the leading-edge vortex, during the late stage of its formation on the

rectangular (type A) wing planform, for K = 0.393. As the pitch rate is decreased from K = 0.393 to 0.098 by a factor of 4, the similar state of the leading-edge vortex is delayed by the order of 1.25 C/U. Also, side view images indicate that the leading-edge vortex forms further away from the wing surface for the high values of pitch rate.

Analyzing the images, in the same way described above, of the flow patterns on the other wing configurations shown in Figure 5.2.3, it can be concluded that variation of pitch rate has a very similar effect on the flowfield evolution along any wing geometry, e.g., it causes a delay in timing of formation and development of the leading-edge vortex. However, quantitative characterization of the flow structure is still necessary, in order to properly define the basic features of three-dimensional vortex formation, and the influence of pitch rate and wing geometry. In the following section, quantitative characterization of the flow structure involves stereoscopic particle image velocimetry technique.

5.3 THREE-DIMENSIONAL REPRESENTATION OF TIME EVOLUTION OF FLOW STRUCTURE VIA STEREOSCOPIC PARTICLE IMAGE VELOCIMETRY

In this section, the focus is on further investigation of the effect of wing geometry on vortex formation and development. The quantitative three-dimensional flow structure and topology are determined along finite-span wings subjected to pitch up motion. Two extreme wing configurations, represented by the rectangular and elliptical plates, are chosen from the wing planforms described in the previous section.

The smoothed linear pitch-up motion of the wing, which is represented by the green color on the graph of Figure 5.1.1b, is about the quarter-chord of the wing, from

an angle of attack α = 0 to 45°. This pitch-up occurs over a dimensionless time scale t =4.0 C/U. For both types of wing configurations, the pitch-up ramp rate is $\dot{\alpha}$ = 0.174 rad/sec. The corresponding reduced pitch rate, based on chord C, is $K = \dot{\alpha}C/2U$ =0.098 for both wings, and based on mean aerodynamic chord, it is $K = \dot{\alpha}\bar{C}/2U$ = 0.098 for the rectangular wing, and 0.084 for elliptical wing.

The techniques of stereoscopic particle image velocimetry (SPIV) and volume reconstruction described in section 5.2 are employed to determine the three-dimensional flow structure.

5.3.1 Phase-Averaged Three-dimensional Streamline Patterns

Figures 5.3.1a, 5.3.1b and 5.3.1c provide side, end and plan views of the three-dimensional streamline patterns on the rectangular and elliptical wings. The overall objective of the streamline construction is to visualize the development of the three-dimensional, large-scale vortical structures. Emphasis is therefore given to streamlines in this region of the flow, by originating streamlines in the regions of high vorticity concentration. In addition, it is insightful to reveal the separation streamlines from the edges of the plate, and therefore streamlines were also originated in this region.

The side views of Figure 5.3.1a show the progressive development of an apparent leading-edge vortex. For the case of the rectangular wing, represented by the images in the left column of Figure 5.3.1a, the sequence of images suggests that the apparent leading-edge vortex moves away from the surface of the wing and increases in scale. In comparison, for the case of the elliptical wing, shown in the right column of images, the concentrated swirl pattern, which corresponds to the apparent leading-

edge vortex, gradually increases in scale as it moves away from the surface of the wing in the first three images, followed by departure from the wing surface in the fourth image. The two-dimensional computations of Visbal and Shang (1989) are for a range of dimensionless pitch rate $\Omega C/U$ from 0.1 to 0.6 ($K = \dot{\alpha}C/2U$ from 0.05 to 0.3) and pitching axis locations from quarter- to three-quarter chord and pitch-up from 0 degrees to 50 degrees. The present study corresponds to a value of $\Omega C/U$ = 0.196 ($\dot{\alpha}C/2U$ = 0.098), with the pitching axis at quarter chord, and the closest case of Visbal and Shang (1989) is $\Omega C/U$ = 0.2 with the pitching axis at quarter-chord. In their case, patterns of vorticity indicate formation of a large-scale leading-edge vortex, which is displaced a smaller distance from the surface of the wing than the apparent leading-vortex of Figure 5.3.1a.

Figure 5.3.1b, which provides end views of the streamline pattern, indicates, however, that the apparent leading-edge vortex of Figure 5.3.1a corresponds only to the central portion of the streamline pattern. For the rectangular wing, shown in the left column of images, lift up of the central portion of the streamline pattern occurs at α = 36° through α = 45° (5.6 *C/U*). During this lift up process, and at locations away from the plane of symmetry of the wing, there is onset and development of streamlines having a component of swirl parallel to the wing surface. For the case of the elliptical wing, shown in the right column, lift-up of the central portion of the vortex is inhibited, and does not occur at α = 27° and 36°. Such lift up eventually becomes evident at α = 45° (4.0 *C/U*), and at α = 45° (5.6 *C/U*), the overall form of the end view of the streamline pattern becomes very similar to that of the rectangular wing at α = 45° (4.0 and 5.6 *C/U*).

Figure 5.3.1c gives corresponding plan views of the streamline patterns. The left column of images corresponds to the rectangular wing. At the earliest instant (α = 22.5°), the ends of the leading-edge vortex are not pinned to the leading-corners of the wing; rather the ends are on either side of the plane of symmetry of the wing, and at locations corresponding to 28 percent of the semi-span. The leading-edge vortex has the form of two opposing swirls. The origin of each swirl is at the leading-edge of the wing, and it has both circumferential and axial flow components. Each swirl is in a direction towards the plane of symmetry of the wing, and they collide at that location. Furthermore, two regions of alleyway flow are apparent; they correspond to the non-swirling streamlines between the origins of the swirl at the leading-edge and the tip vortex at each leading corner. At a later instant, α = 27°, the central portion of the leading-edge vortex has advanced towards the trailing-edge of the wing. Finally, at α = 36° through α = 45° (5.6 *C/U*), the onset and development of a streamline pattern having a swirl component parallel to the wing surface is evident; it increases in scale until it occupies the entire semi-span of the wing.

For the elliptical wing, shown in the right column of images of Figure 5.3.1c, the initial development of the leading-edge vortex is distinctly different from that on the rectangular wing described in the foregoing. At the earliest instant (α = 22.5°), the separation process that gives rise to the leading-edge vortex occurs along the entire periphery of the leading-edge of the wing and, correspondingly, swirling flow with significant spanwise velocity is not evident. At α = 27°, lack of spanwise flow within the leading-edge vortex is evident. At α = 36°, continued development of the vortex shows an increase in diameter and straightening of its axis; simultaneously, streamline

patterns having a component of swirl parallel to the surface occur in the vicinity of the wing tips. These patterns are first evident at α = 36° and at α = 45° (4.0 *C/U*), the scale of these surface-parallel swirl components increases and they occupy an increasingly larger extent of the wing semi-span. At α = 45° (5.6 *C/U*), this swirl extends over nearly the entire semispan, in a manner very similar to the rectangular wing at α = 45° (5.6 *C/U*). The spatial extent of the aforementioned surface-parallel swirl, shown at α = 45° (5.6 *C/U*) in Figure 2c, extends over the semi-spans of each wing. This large-scale swirl is accompanied by distortion of the tip vortices for both the rectangular and elliptical wings. Such distortion is evident at α = 45° (4.0 *C/U*), where the centerline of the tip vortices is deflected in the inboard direction. At α = 45° (5.6 *C/U*), the tip vortices have become ill-defined.

The foregoing patterns of streamlines suggest distinctive features of the vortex evolution on rectangular and elliptical wings, which, nevertheless, lead to a similar state at sufficiently long time from the onset of the wing motion. To substantiate and quantify the development of these vortex patterns, characterization of volumes of iso-*Q*, and projections of vorticity are essential. These features are described in the sections that follow.

5.3.2 Phase-Averaged Iso-Q Volumes

Figures 5.3.2a and 5.3.2b show surfaces of constant *Q*. Surfaces of iso-*Q* correspond to constant values of the second invariant of the velocity gradient tensor. It is previously explained in detail in section 4.2.2. Herein, the value of Q = 5.

In Figure 5.3.2a, the view is looking downstream, and in Figure 5.3.2b, it is looking upstream. In both figures, the left column of images corresponds to the

rectangular wing and the right column represents the elliptical wing. For the rectangular wing, the central portion of the vortical structure that originates in the leading-edge region lifts away from the surface of the wing at α = 27° and 36°, whereas no such distortion is evident for the case of the elliptical wing. At α = 45° (4.0 and 5.6 *C/U*), however, the three-dimensional vortical structure develops on the elliptical wing, and at α = 45° (5.6 *C/U*), the structures on both wings closely resemble each other. Taking an overview of all of the images in Figures 5.3.2a and 5.3.2b, and comparing with the corresponding images of the three-dimensional streamline patterns in Figures 5.3.1a and 5.3.1b, it is evident that the evolution of the three-dimensional surfaces of iso-*Q* are compatible with the major features of the streamline patterns.

5.3.3 Phase-Averaged Patterns of Spanwise Vorticity

Figures 5.3.3a and 5.3.3b show slices of the vortex structure corresponding to contours of constant spanwise vorticity. As in previous layouts, the left and right columns of images represent respectively the rectangular and elliptical wings. Views looking downstream (Figure 5.3.3a) and upstream (Figure 5.3.3b), provide different perspectives of the patterns of spanwise vorticity as a function of angle of attack. Consider the rectangular wing, as represented in the left columns of Figures 5.3.3a and 5.3.3b. At α = 27° and 36°, the spanwise variation is substantial, with relatively large-scale patterns of vorticity well above the surface of wing near the plane of symmetry, and much smaller-scale concentrations as the tip of the wing is approached. The layers of vorticity at, and immediately adjacent to, the tip of the wing are, of course, strongly influenced by formation of the tip vortex. In contrast, consider the case of the elliptical wing in the right columns of Figures 5.3.3a and 5.3.3b, in particular at α = 27° and

36°, the spanwise variation of the concentrations of vorticity shed from the leading-edge is relatively mild, except in the tip region.

At α = 45° (4.0 *C/U*), the spanwise nonuniformity of the vorticity concentrations from the rectangular wing is much more pronounced than from the elliptical wing, but the degree of spanwise nonnuniformity on the elliptical wing has increased. Finally, at α = 45° (5.6 *C/U*), the patterns of spanwise vorticity on the rectangular and elliptical wings have attained a very similar structure, that is, the spanwise variation is remarkably congruent.

5.3.4 Phase-Averaged Patterns of Surface-Normal Vorticity

The streamline patterns of Figures 5.3.1b and 5.3.1c indicate a surface-parallel component of swirl at sufficiently high angle of attack and, furthermore, the iso-*Q* surfaces of Figures 5.3.2a and 5.3.2b show volumes oriented normal to the surface, at spanwise locations well away from the plane of symmetry of the wings. These general observations, along with distinctively different mechanisms and rate of development of the three-dimensional vortical structures on the rectangular and elliptical wings, suggest that examination of slices of surface-normal vorticity can provide further insight. Figures 5.3.4a and 5.3.4b show such representations (Images in these layouts conform to the layouts of Figures 5.3.1 through 5.3.3). On the rectangular wing, at α = 27°, small-scale regions of surface normal vorticity are evident, at spanwise locations well inboard of the wing tips. These concentrations are designated as *A* and *B*. On the other hand, on the elliptical wing, corresponding concentrations at α = 27° are not discernable. Concentrations do appear, however, at the wing tips, and they are designated as *A* and *B*.

At α = 36°, on the rectangular wing, the clusters of surface-normal vorticity, designated as *A* and *B*, have further developed, and simultaneously moved towards the plane of symmetry. On the elliptical wing, the clusters *A* and *B* have further matured near the tip of the wing.

At α = 45° (4.0 *C/U*), clusters *A* and *B* on the rectangular wing take on a larger scale as a result of continued development near the plane of symmetry. On the elliptical wing, clusters *A* and *B* also indicate a larger scale, as well as movement towards the plane of symmetry.

Finally, the images at α = 45° (5.6 *C/U*) indicate that the clusters *A* and *B* have a remarkably similar form on the rectangular and elliptical wings. On the rectangular wing, clusters *A* and *B* have actually moved further apart, while on the elliptical wing, they have moved closer together, relative to their respective locations at α = 45° (4.0 *C/U*). In addition to the inboard clusters *A* and *B* described in the foregoing, the surface-normal vorticity associated with the tip vortices undergoes well-defined alterations. These clusters are designated as *A′* and *B′*. With increasing angle of attack, clusters *A′* and *B′* are deflected in the inboard direction until, as indicated at α = 45° (5.6 *C/U*), they envelop clusters *A* and *B*. This general process is modified for the case of the elliptical wing, but, in the end, clusters *A′* and *B′* eventually envelop *A* and *B* in a similar fashion as for the rectangular wing.

5.3.5 Phase-Averaged Patterns of Spanwise Velocity

Further insight into the distinctive mechanisms of development of the patterns of Figures 5.3.4a and 5.3.4b can be gained by examination of patterns of spanwise velocity *w/U*, as shown in Figure 5.3.5. Contours of constant *w/U* are stacked, in order

to allow illustration of the higher levels that would be obscured by a regular volume construction. Directions of positive and negative *w/U* are designated respectively by yellow-red and blue contours; their directions are indicated by the arrows.

Consider images for the rectangular wing, shown in the left column of Figure 5.3.5. At α = 27°, flow *towards* the plane of symmetry is represented by contours *A* and *B*, which are associated with the contours of surface-normal vorticity at α = 27° in Figures 5.3.4a and 5.3.4b. At α = 36° in Figure 5.3.5, regions *A* and *B* have increased in scale, and are comprised of a number of stacked contours. These regions are associated with the stacked contours of surface-normal vorticity ω_y designated as *A* and *B* in the corresponding images of Figures 5.3.4a and 5.3.4b, as well as with the plan view of the streamline patterns on the rectangular wing at α = 27° and 36° in Figure 5.3.1c. A further, important feature of the flow pattern on the rectangular wing at α = 36° is the onset of small-scale stacked contours of *w/U*, designated as *C* and *D*, in the vicinity of the leading-edge. These contours clearly indicate flow *away from* the plane of symmetry of the wing.

In contrast, on the elliptical wing in Figure 5.3.5, at α = 27° and 36° patterns of spanwise velocity similar to those in the foregoing do not exist at locations inboard of the tips. This observation indicates that the relatively undeformed streamline patterns of the leading-edge vortex on the elliptical wing at α = 27° and 36° in Figures 5.3.1b and 5.3.1c, do not involve significant spanwise flow through the vortex core.

Further evolution of the patterns of spanwise velocity *w/U* is shown at α = 45° (4.0 and 5.6 *C/U*). For the rectangular wing, the scale of these contours progressively increases. Correspondingly, on the elliptical wing, the first indication of flow away

from the plane of symmetry in the vicinity of the leading-edge is at α = 45° (4.0 *C/U*), and its rapid development to much larger scale is shown at the later time α = 45° (5.6 *C/U*). That is, the spatial extent of the contours of *w/U* along the leading-edge of the elliptical wing has dramatically increased, such that it is commensurate with the patterns along the leading-edge of the rectangular wing.

The mechanisms and rate of development of the patterns of *w/U* in the vicinity of the leading-edge, as described in the foregoing, are consistent with the evolution of the patterns of surface-normal vorticity shown in the images of Figures 5.3.4a and 5.3.4b, at α = 45° (4.0 and 5.6 *C/U*).

5.3.6 Phase-Averaged Sectional Patterns of Flow Structure

In addition to volume representations of the flow structure, as given in the foregoing, it is insightful to directly compare sectional cuts of vorticity, velocity vectors, streamlines and contours of constant spanwise velocity. These representations are provided in Figures 5.3.6a through 5.3.6c, at different times after onset of the pitch-up motion, as well as for different elevations of the sectional cut above the surface of the wing.

Figure 5.3.6a shows images at α = 45° (4.0 *C/U*). In the top two rows of images, volume representations of surface-normal vorticity ω_y are superposed on streamline patterns. Both plan and end views of these volume representations are shown. The sectional cuts in the third through fifth rows of images of Figure 5.3.6a are all on the same plane, which is located a distance *y/C* = 0.3 above the surface of the wing.

The patterns of surface-normal vorticity ω_y in the third row of images are due to contributions from: the deflected tip vortices; and the large-scale swirls parallel to the surface of the wing. These representations for the rectangular and elliptical wings correspond to selected sectional slices of ω_y given in Figures 5.3.4a and 5.3.4b.

The patterns of velocity vectors given in the fourth row of images of Figure 5.3.6a have distinctive features that are evident on both the rectangular and elliptical wings. First of all, the velocity vectors in the vicinity of the plane of symmetry indicate well-defined flow in the upstream direction. Second, a relatively high velocity, jet-like flow occurs just inboard of the outermost vorticity concentrations ω_y. This jet-like flow is located on both sides of the plane of the symmetry of the rectangular and elliptical wings, as shown in the third row of images. Comparison of these regions of jet-like flow with the sectional concentrations of surface-normal vorticity ω_y shows that the jet-like flow occurs through the alley between the well-defined vorticity concentrations.

Further clarification is provided by the patterns of sectional streamlines on the rectangular and elliptical wings given in the bottom row of images of Figure 5.3.6a. Contours of constant spanwise velocity w/U are superposed on these streamline patterns. On either side of the plane of symmetry on the wing, streamlines of an alleyway flow are located between two well-defined swirl patterns, one located well upstream of the trailing-edge and the other located near the trailing-edge of the wing. The swirls located well upstream of the trailing-edge, designated by the foci F_a and F_b, represent the aforementioned large-scale swirls parallel to the surface of the wing, addressed in Figures 5.3.1b and 5.3.1c. The swirl patterns near the trailing-edges of

the rectangular and elliptical wings are designated by the foci F_e and F_f. They are due to tilting of the axes of the tip vortices. That is, the axis is not parallel to the surface of the wing, rather it is substantially deflected away from the surface, as shown in the side view of images (at an angle of attack $\alpha = 45°$) in Figure 5.3.1a. The alleyway flow between the swirl patterns F_a and F_e, as well as between F_b and F_f is associated with a high value of spanwise velocity, of the order of 80% of the freestream velocity.

Over the central portion of the rectangular wing in the bottom image of figure 5.3.6a, two large-scale swirls of opposite sense are contained within streamlines that are connected to saddle points S_a and S_b (apparent intersections of streamlines) near the leading-and trailing-edges of the wing. Moreover, the upstream half of this streamline corresponds to merging together of streamlines from the regions interior and exterior to it; these streamlines correspond to negative bifurcation lines BL^-. On the other hand, the downstream half is associated with streamlines that diverge away from it, thereby forming positive bifurcation lines BL^+. Finally, the upstream half of this streamline pattern, specifically the negative bifurcation line BL^-, is coincident with maxima of the spanwise velocity, which indicate spanwise flow *away* from the plane of symmetry of relatively large magnitude, that is, of the order of 80% of the freestream velocity. On the other hand, the streamline pattern over the central portion of the elliptical wing, shown in the image at the bottom right of Figure 5.3.6a is not as well developed as for the rectangular wing. Moreover, large magnitude contours of spanwise velocity, which are evident near the leading-edge of the rectangular wing, do not exist on the elliptical wing.

Figure 5.3.6b the shows the same type of sectional patterns as in Figure 5.3.6a, but at a later time, as indicated in the schematic at the top of Figure 5.3.6b, that is for α = 45° (5.6 *C/U*). The volume representations of surface-normal vorticity and streamlines, shown in the top two rows of images, are generally similar for both the rectangular and elliptical wings. Regarding the sectional cuts of surface-normal vorticity shown in the third row of images, they also have a broadly similar form. The patterns of velocity vectors shown in the fourth row of images of Figure 5.3.6b also are analogous, with predominance of upstream-oriented flow over the central portion of each wing. Finally, for the patterns of streamline topology, shown in the fifth row of images, the overall form of the bounding streamlines, i.e., bifurcation lines BL^- and BL^+, which are connected to saddle points S_a and S_b, is similar for both wings. Merging of streamlines towards the streamline designated as a negative bifurcation line BL^-, occurs over the region upstream of the midchord of the wing; and divergence of streamlines away from the streamline indicated as a positive bifurcation line BL^+, occurs over the region downstream of the midchord. Compared to the earlier time indicated in Figure 5.3.6a, the scale of the surface parallel swirl patterns defined by the foci F_a and F_b has increased in spatial extent to the edges of the wings. Due to this enlarged scale of the swirl patterns, the foci F_e and F_f on the elliptical wing have disappeared, and they have moved towards the trailing-edge on the rectangular wing. Furthermore, the patterns of spanwise velocity indicate, for both wings, pronounced flow away from the plane of symmetry near the leading-edge and towards the plane of symmetry near the trailing-edge, with magnitudes of approximately 80 percent of the freestream velocity.

Figure 5.3.6c provides representations of near-surface patterns (at y/C = 0.1). Considering, first of all, the top two rows of images, at α = 45° (4.0 *C/U*), generic features evident in the preceding Figures 5.3.6a and 5.3.6b persist: (i) pronounced upstream flow over the central region of the wing; (ii) exterior to this region, jet-like flows in the downstream direction, emanating from the regions near the corners of the rectangular wing; and (iii) contours of constant spanwise velocity that indicate high velocity flow away from the plane of symmetry near the leading-edge, and towards the plane of symmetry near the trailing-edge. On the elliptical wing, however, the spanwise flow away from the plane of symmetry (in the vicinity of the leading-edge) has a relatively low magnitude. For both the rectangular and elliptical wings, a well-defined saddle point S_a occurs at the leading-edge, and the streamline corresponding to the negative bifurcation line BL^- is the coincident with the leading-edge of the wing. Furthermore, while foci F_a and F_b (apparent centers of swirl streamline patterns) occur on the central portion of the rectangular wing, they are located away from the plane of symmetry, i.e., near the tips on the elliptical wing. The focal points of the large-scale swirl patterns, designated as F_c and F_d, are evident near the leading-edge on the rectangular wing. However, foci F_c and F_d appear at locations downstream of the midchord of the elliptical wing. In essence, details of the near-surface streamline patterns are distinctively different from those on the plane away from the surface of the wing, which are shown in the preceding figure layouts.

In the bottom row of images of Figure 5.3.6c, corresponding to a later time, α = 45° (5.6 *C/U*), a more mature form of the large-scale swirl patterns of streamlines is evident on both the rectangular and elliptical wings. Furthermore, immediately

upstream and downstream of each focus F_a and F_b, large magnitude spanwise flow is evident respectively in directions away from the plane of symmetry, and towards the plane of symmetry. Along the leading-edges of both the rectangular and elliptical wings, the saddle point S_a, as well as the negative bifurcation lines BL^-, are evident. At the trailing edge of the rectangular wing, the saddle point S_b and adjacent nodes N_a and N_b are present. Along the trailing edge of the elliptical wing, however, positive bifurcation lines BL^+ as well as nodes N_c and N_d occur.

In essence, the near-surface region of the wing tends to exhibit certain of the overall patterns evident at the higher elevation shown in Figures 5.3.6b and 5.3.6c. Distinguishing features are, however, present, as the flow topology must conform to the geometrical outline of the wing planform.

5.3.7 Phase-Averaged Patterns of Spanwise Vorticity and Circulation

In addition to the characterization of flow patterns described in previous sections, circulation calculation is performed at different chordwise planes in order to gain further insight into the distinctive mechanisms of leading-edge vortex development. In Figure 5.3.7, the normalized circulation $\Gamma/2bU$ distribution in the spanwise direction z/C is shown with the patterns of spanwise vorticity. Circulations are computed from the velocity data at each chordwise plane with the methodology which is described in section 2.5. The enclosed area used for circulation calculations is chosen as a rectangular area which only covers leading-edge vortex on each chordwise plane. Therefore, distinctive stages of the flowfield development for each wing planform can be analyzed in terms of the circulation strength of the leading-edge vortex system. In order to consider only the leading-edge vortex circulation, the

circulation values at the chordwise planes close to the tip regions is excluded. The graphs show the values of the leading-edge vortex circulation on the planes between $z/2b$ = -0.75 and 0.75.

As indicated in the first row of images of Figure 5.3.7, corresponding to an angle of attack, α = 27°, and a convective time 2.4 C/U, the circulation values vary along the spanwise direction because of the substantial spanwise variation of vorticity on the rectangular wing. Also, the circulation reaches its maximum value around $z/2b$ = ±0.25, and remains uniform over the range -0.25< $z/2b$ <0.25. However, for the elliptical wing, the leading-edge vortex has quite uniform circulation strength in the spanwise direction. At α = 36° (3.2 C/U), as indicated in the second row of images, the circulation distribution is very similar for both wing planforms. Pronounced nonuniformity of circulation at this instant is due to the formation of larger-scale patterns of vorticity in the vicinity of the plane of symmetry. As seen from the images in the third row of Figure 5.3.7, the circulation distribution on both wings becomes remarkable similar at α = 45° (4.0 C/U), although the spanwise nonuniformity of the patterns of vorticity concentration along the span of the rectangular wing is much more pronounced than along the elliptical wing.

The spanwise variations of the leading-edge vortices coexist with tip vortices shown in the bottom set of images of Figure 5.3.7. The vorticity contours therein correspond to streamwise (not chordwise) projections of vorticity, designated as $\omega_{x'}$. Variations of $\Gamma/2bU$ (based on $\omega_{x'}$) vs. x/C are shown, with blue and red dots representing respectively values of circulation corresponding to each of the vorticity contours on the rectangular and elliptical wings. Although the asymptotic value of

$\Gamma/2bU$ is nearly the same for both wings, the rise of $\Gamma/2bU$ is delayed to larger values of x/C on the elliptical wing.

Considering the entire set of images of Figure 5.3.7, and cross-comparing them, the overall circulation of the leading-edge vortex on both wings increases with time and angle of attack. However, during early stages of the maneuver, the variation of circulation is more uniform on the elliptical wing compared to the circulation distribution on the rectangular wing. Also, the values of leading-edge vortex circulation along the central portion of the elliptical wing are lower than the circulation values along the rectangular wing. But, at the end of the maneuver, a remarkably similar distribution of circulation of the leading-edge vortex system is evident for both wings, in spite of a distinctly different sequence of events of the leading-edge vortex formation.

5.4 CONCLUDING REMARKS

Low aspect ratio wings undergoing pitch-up motion to high angle of attack give rise to the onset and development of three-dimensional vortical structures that converge to a well-defined state. The time evolution of these structures is characterized using techniques of stereoscopic particle image velocimetry and dye visualization. Evolution of the three-dimensional leading-edge vortex formation, effects of wing geometry and pitch rate on the flow structure are addressed via dye visualization. Time sequences of volume images provide interpretation of the three-dimensional flow structure in conjunction with three-dimensional streamline patterns, iso-Q surfaces, contours of vorticity projections in orthogonal directions, spanwise velocity, velocity vectors, and circulation as well as streamline topology on cross-

sectional planes. The principal findings of this investigation are described in the following.

A fully-evolved state of the flow structure is approached after attainment of the maximum angle of attack. The large-scale vortical structures on the wing take a form that is relatively independent of the wing planform. Near the surface of the wing, large-scale swirl patterns of opposite sense occur on either side of the plane of symmetry of the wing; each swirl occupies nearly the entire semispan. Correspondingly, volumes of surface-normal vorticity occur within each of these regions. Near and at the plane of symmetry, however, at elevations well above the surface of the wing, spanwise vorticity dominates.

In this fully-evolved state, the large-scale swirl near the surface of the wing, which is parallel to the wing surface, involves large magnitudes of spanwise velocity. Near the leading-edge of the wing, the spanwise velocity is away from the plane of symmetry and near the trailing edge of the wing, it is towards the plane of symmetry. These spanwise velocity magnitudes can be nearly as large as the freestream velocity. Moreover, the associated (surface parallel) streamline topology shows similar types and locations of critical points, i.e., foci, bifurcation lines and saddle points, at elevations above the wing surface, irrespective of which of the extreme planforms, rectangular versus elliptical, is considered. The large-scale swirl involves a well-defined focus at the center of the swirl streamline pattern, which may be either stable or unstable. At the surface of the planform, however, the streamline topology shows distinguishable differences, which are dependent upon planform geometry, as it adapts to the local wing configuration.

The initial stages of vortex development and distortion that eventually lead to the fully-evolved state described in the foregoing are, however, strongly dependent upon the occurrence or nonoccurrence of axial flow within the leading-edge vortex, and thereby are dependent on the planform of the wing. The initial stage of formation of the leading-edge vortex on the rectangular wing involves formation of opposing, small-scale vortices having axial and circumferential components, and emanating from the straight leading-edge of the wing, located at 28 percent of the semi-span on either side of the plane of symmetry of the wing; in contrast, formation of the leading-edge vortex from the leading-edge of the elliptical wing does not involve a mechanism for generation of axial flow. When such axial flow occurs within the leading-edge vortex, as is the case on the rectangular wing, it is oriented towards the plane of symmetry of the wing, and gives rise to rapid displacement of the central portion of the vortex (located near the plane of symmetry of the wing) away from the wing surface, thereby causing severe vortex distortion. A further, important consequence of axial flow within the leading-edge vortex is as follows. Due to interaction of opposing axial flows at the plane of symmetry, it leads, in that region, to the rapid onset of swirl oriented parallel to the surface of wing. This surface-parallel swirl is, in turn, associated with the rapid development of volumes of surface normal vorticity on either side of the plane of symmetry of the wing. The scale of these volumes increases with time, as they move away from the plane of symmetry. If, however, axial flow does not occur within the leading-edge vortex, the patterns of surface-parallel swirl and corresponding clusters of surface normal vorticity are first evident near the tips of the wing and, with increasing time, they increase in scale while moving towards the plane

of symmetry. This case of insignificant axial flow within the leading-edge vortex is associated with a substantial time lag for onset of the fully-evolved state of the three-dimensional vortex system, relative to the case where substantial axial flow occurs.

The traditional interpretation of the flow structure on a wing of large span undergoing pitch up motion to high angle of attack involves the large-scale, quasi-two-dimensional leading-edge vortex, i.e., the dynamic stall vortex. For low aspect ratio wings, the foregoing observations indicate that the flow structure is highly three-dimensional, with pronounced regions of surface-normal vorticity and surface-parallel swirl that are orthogonal to the vorticity and swirl of the classical large-scale leading-edge vortex. This three-dimensionality has important consequences for the variation of spanwise vorticity of the leading-edge vortex along the span of the wing. Sectional cuts of spanwise vorticity show, for the asymptotic state, remarkably similar spanwise variations; only near the plane of symmetry do large-scale regions of spanwise vorticity exist, with relatively large values of circulation. Moreover, these spanwise variations of sectional cuts of spanwise vorticity show a rapid approach to the fully-evolved state of the flow structure when pronounced spanwise velocity occurs in the leading-edge vortex, relative to the case where insignificant spanwise flow occurs.

The overall nature of the flow structure characterized in this investigation has broad similarities, or analogies, with recent investigations. Taira and Colonius (2009a) computed the evolution of the three-dimensional vortex structure on an impulsively-translated wing and observed the onset of a vortex loop, particularly in the vicinity and downstream of the trailing-edge of the wing. Visbal (2011) computed the flow structure on a plunging rectangular wing and characterized an arch vortex during the

final stages of three-dimensional development; it is more compact than the analogous structure characterized herein. That is, in the investigation of Visbal (2011), the distance between the legs of the arch vortex and their characteristic diameter are much smaller than the analogous vortical structures characterized herein; a common feature, however, involves spanwise velocities of large magnitude oriented away from the plane of symmetry of the wing near the leading-edge and towards the plane of symmetry near the trailing-edge of the wing. For the limiting case of steady flow past a flat plate at sufficiently high angle of attack, Visbal (2011) reveals the onset of swirl parallel to the wing surface, where the centers of swirl are at the leading-corners of the wing. These previous investigations, taken together with the present study, suggest generic features of the three-dimensional vortex structure on wings undergoing various types of motion.

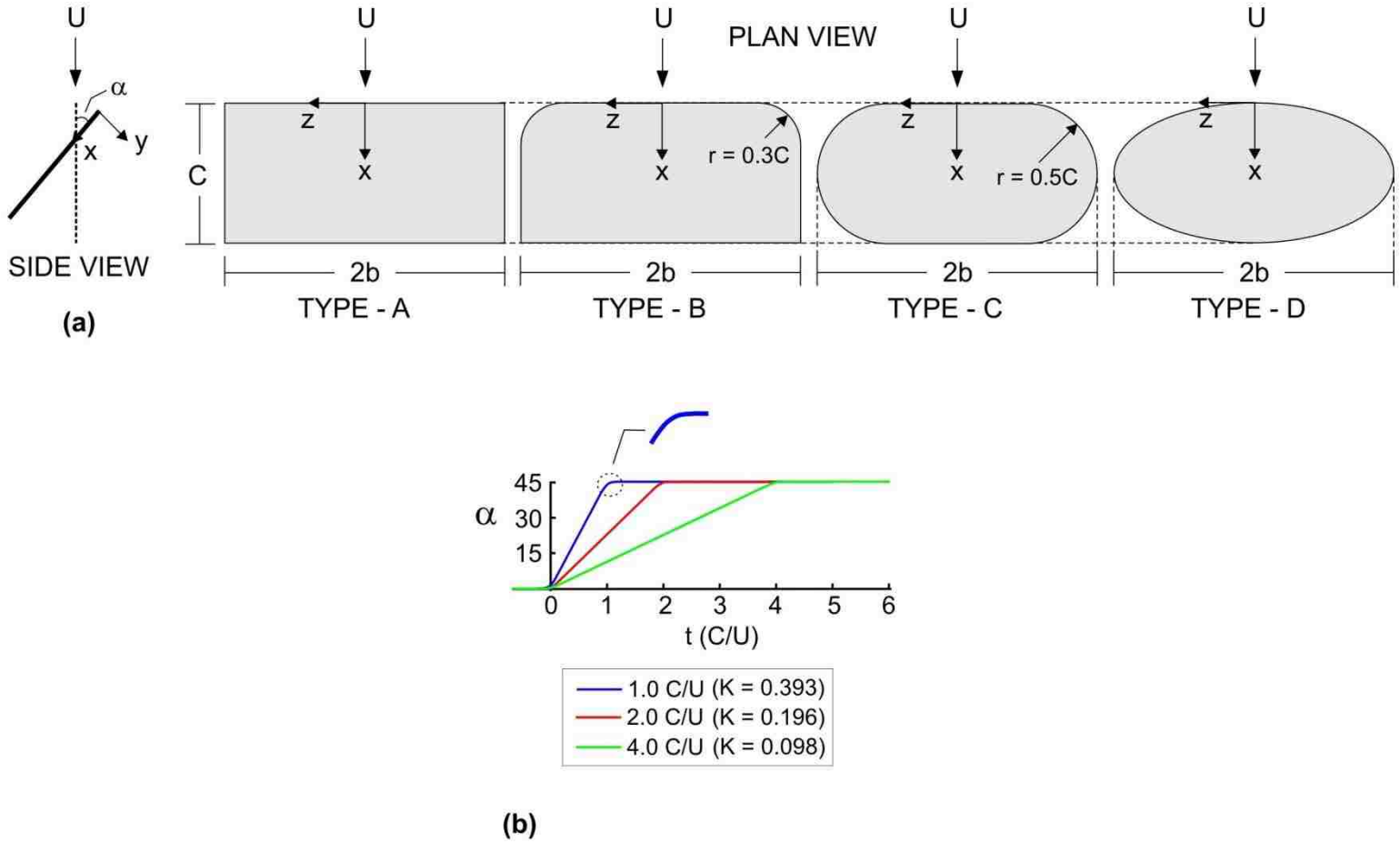

Figure 5.1.1: (a) Overview of wing configurations; **(b)** pitch-up schedule of wing motion.

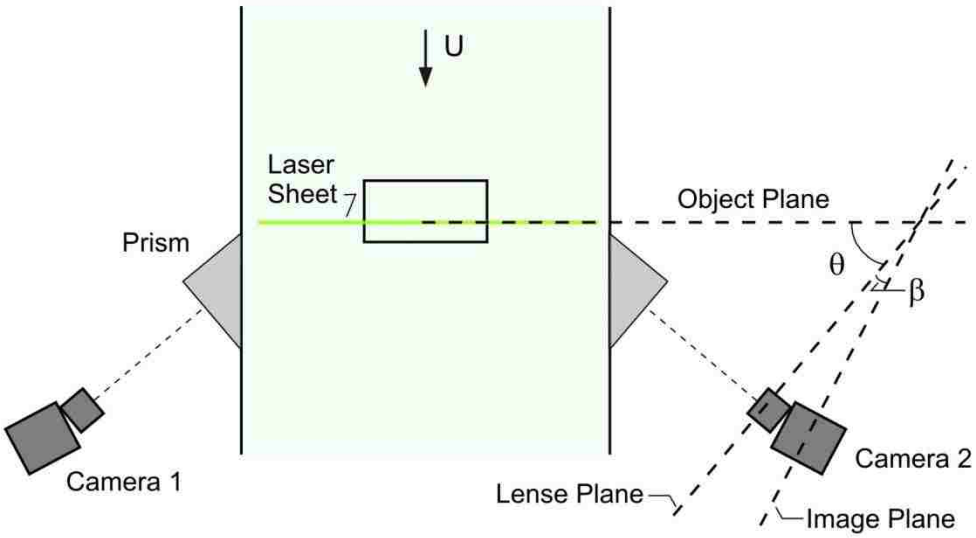

Figure 5.1.2: Overview of quantitative imaging system.

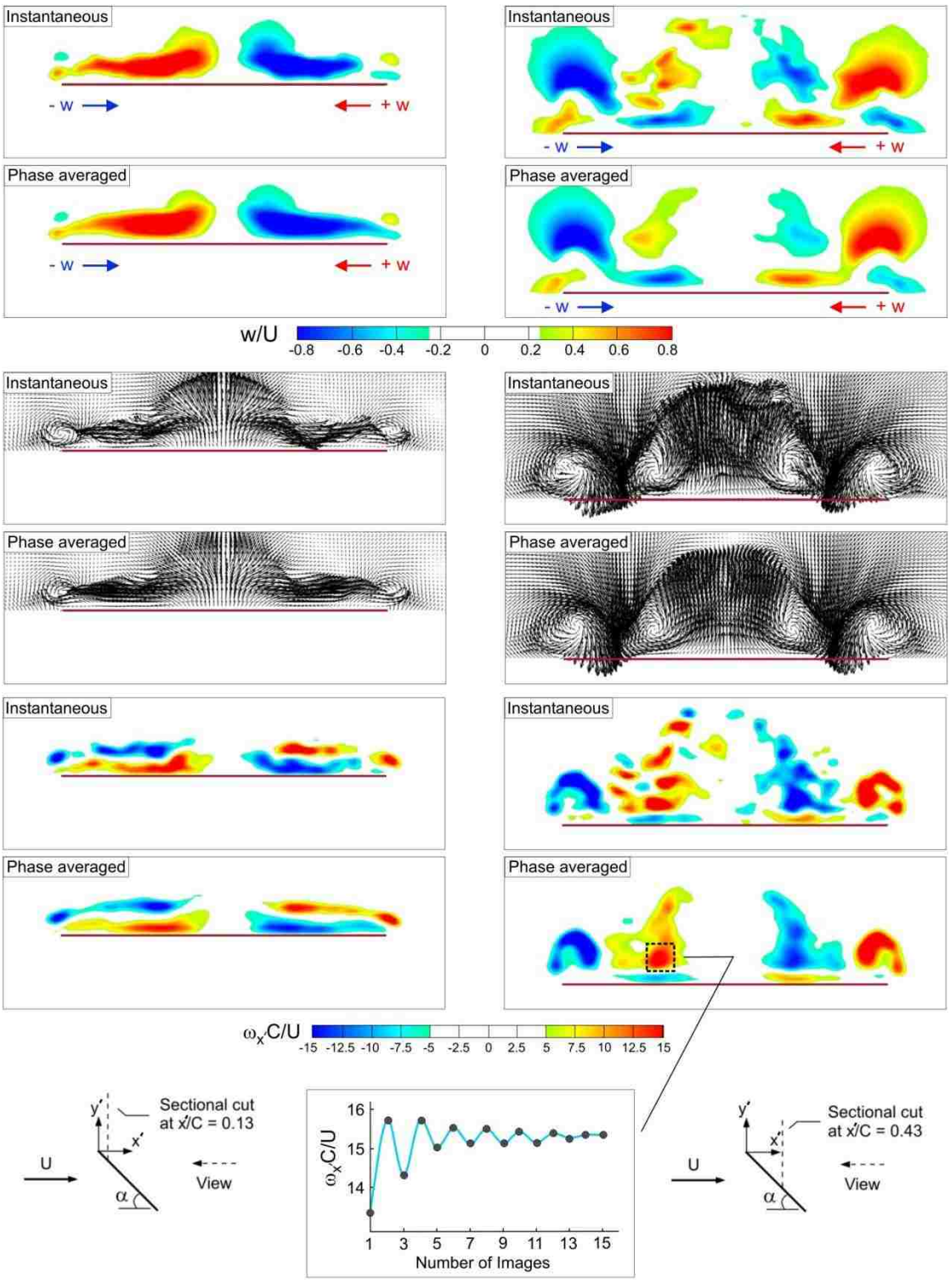

Figure 5.1.3: Comparison of instantaneous and phase-averaged images at two different cross-flow planes; $x'/C = 0.13$ (left column) and $x'/C = 0.43$ (right column).

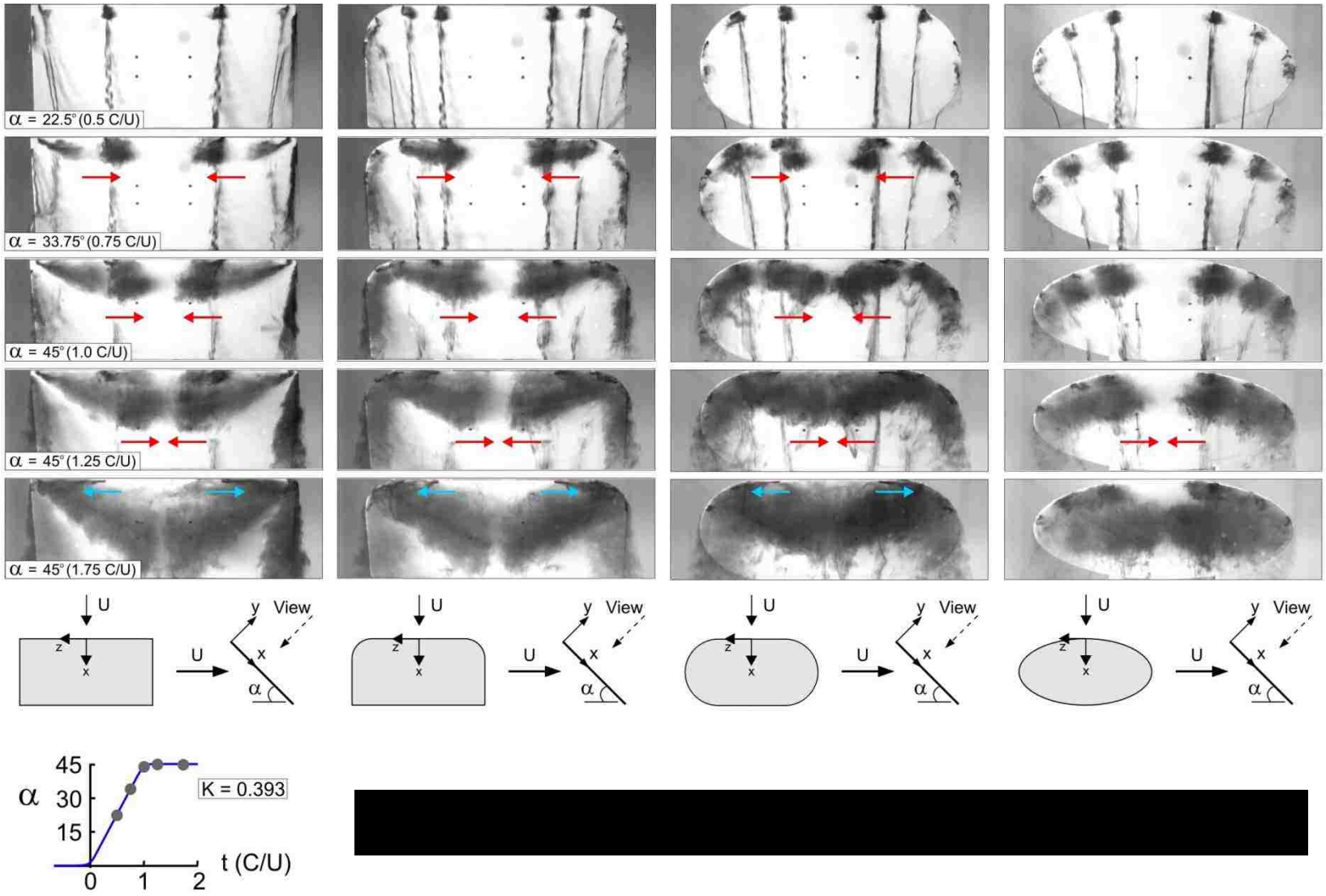
α = 22.5° (0.5 C/U)
α = 33.75° (0.75 C/U)
α = 45° (1.0 C/U)
α = 45° (1.25 C/U)
α = 45° (1.75 C/U)
U
y
View
z
x
α
45
30
15
0
1
2
t (C/U)
K = 0.393

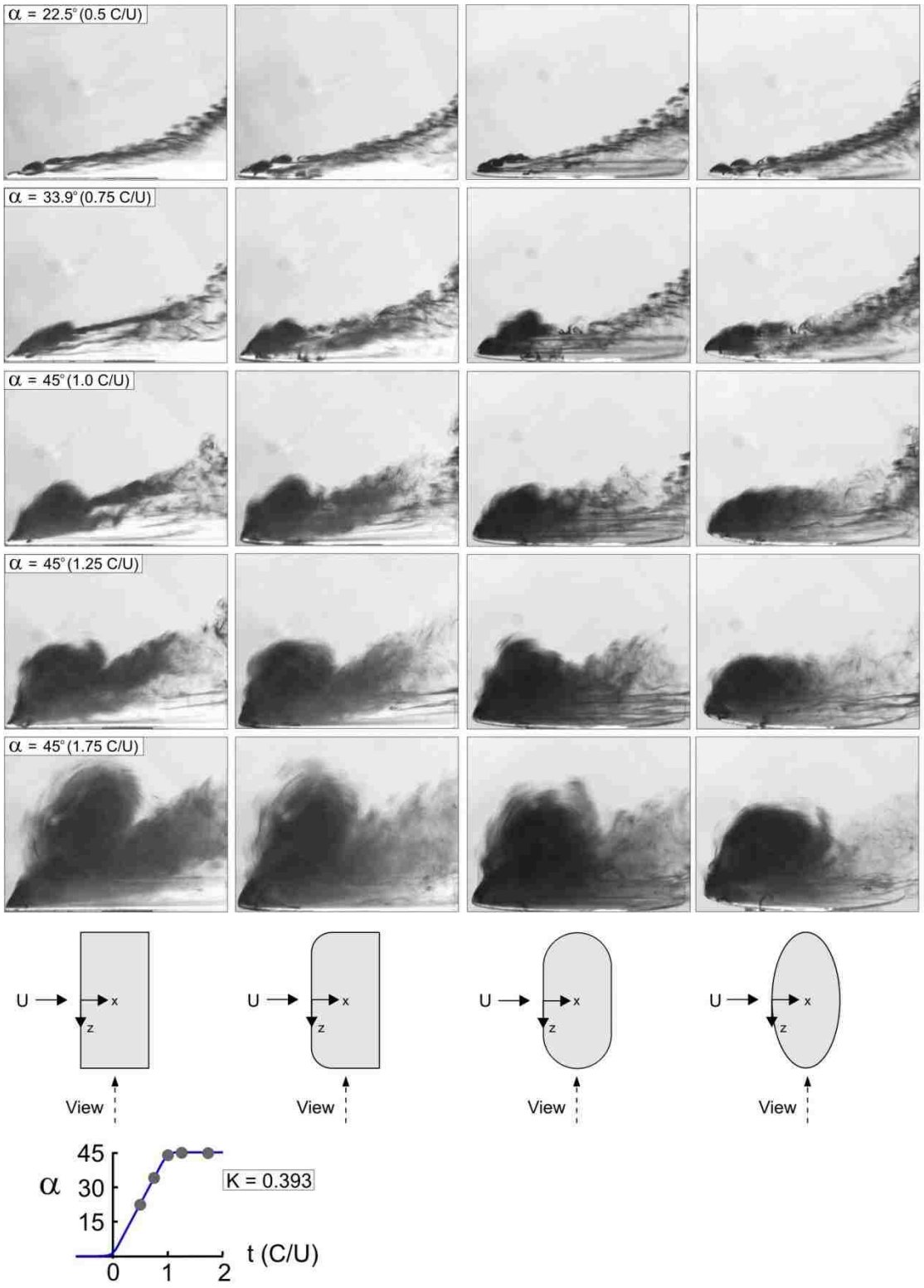

Figure 5.2.1b: Side views of development of flow structure on various wing configurations during pitch-up motion using dye visualization. Pitch point x_p/C = 0.25 and K = 0.393.

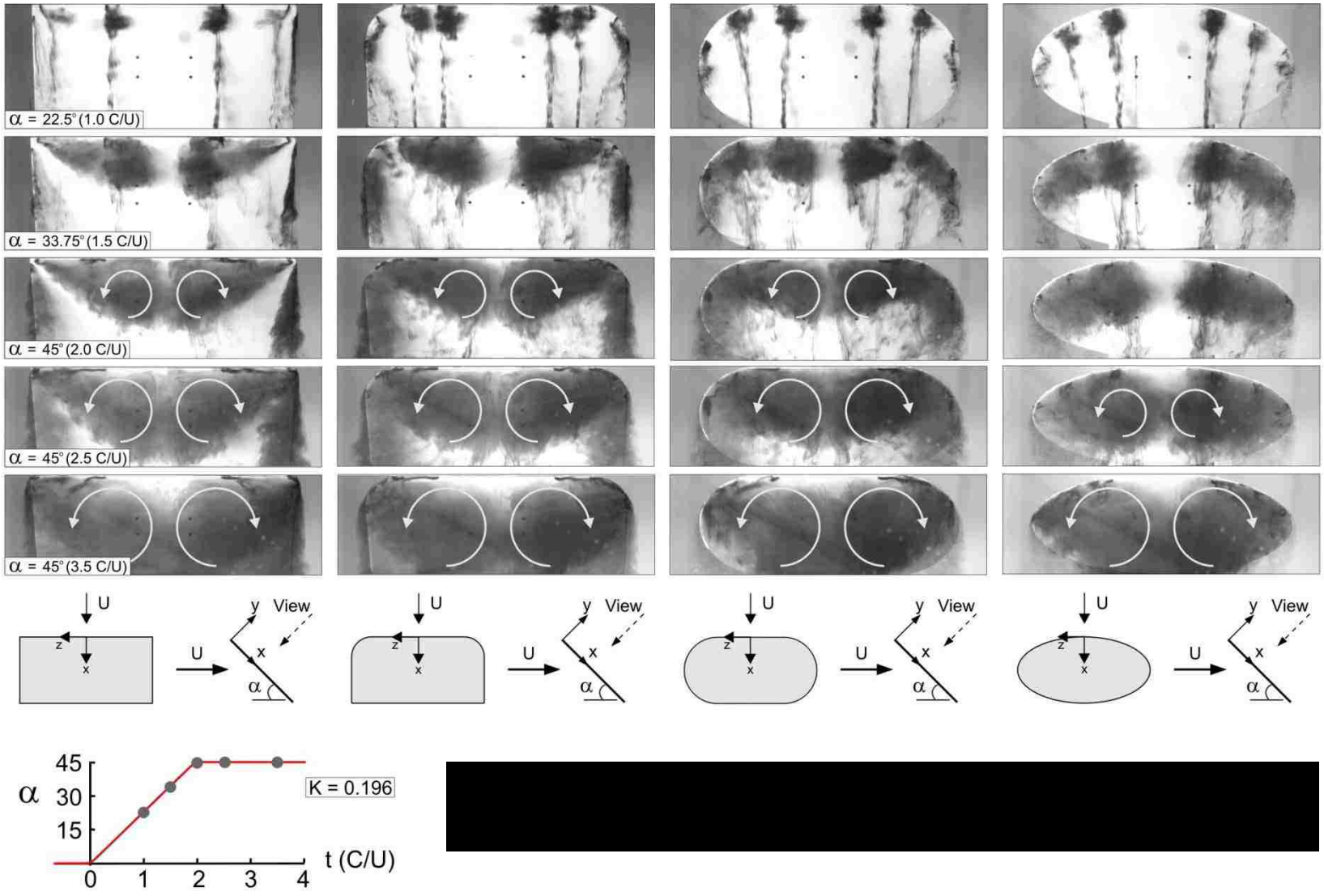
α = 22.5° (1.0 C/U)
α = 33.75° (1.5 C/U)
α = 45° (2.0 C/U)
α = 45° (2.5 C/U)
α = 45° (3.5 C/U)
U
y
View
z
x
α
45
30
15
0
1
2
3
4
t (C/U)
K = 0.196

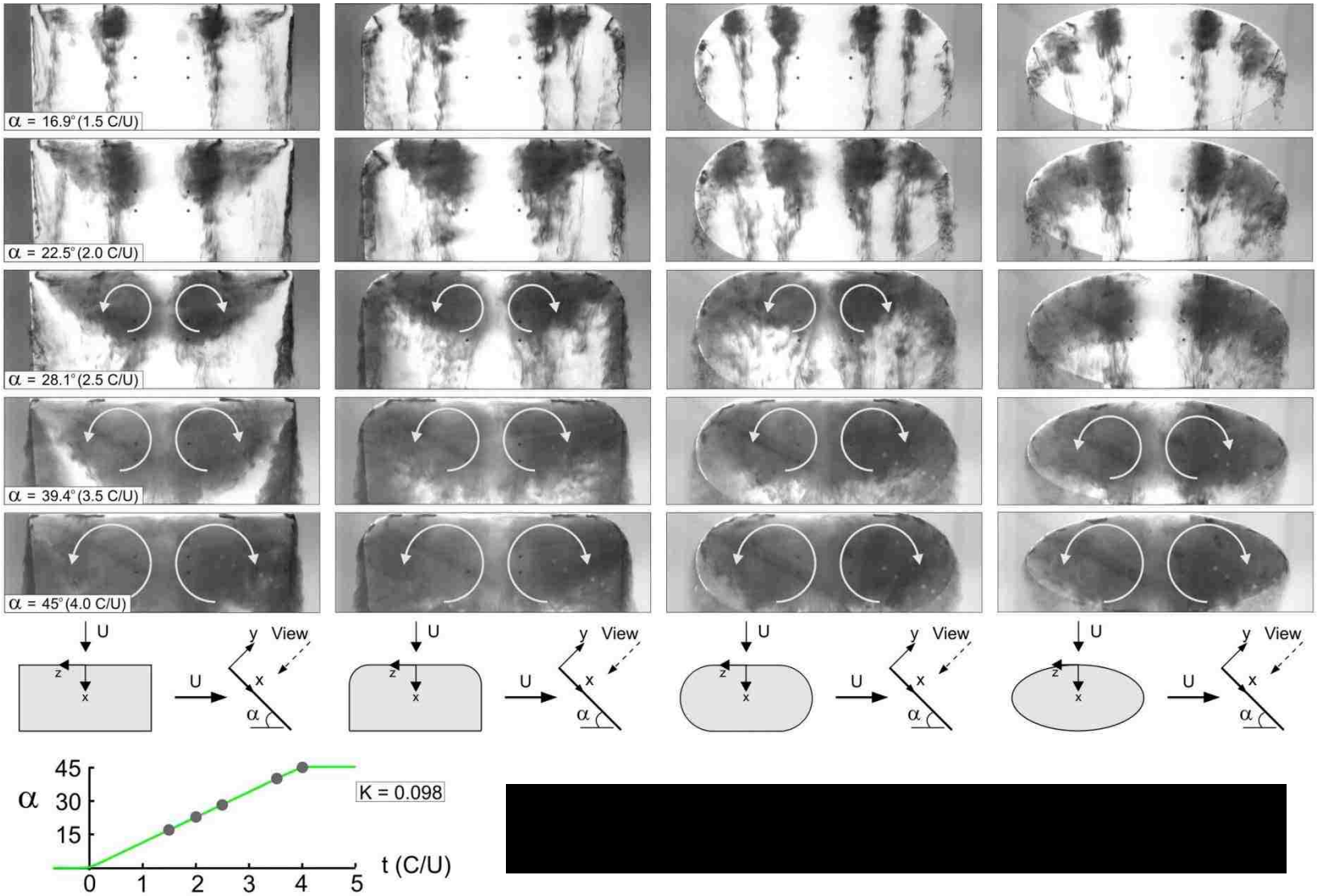
α = 16.9° (1.5 C/U)
α = 22.5° (2.0 C/U)
α = 28.1° (2.5 C/U)
α = 39.4° (3.5 C/U)
α = 45° (4.0 C/U)
U
y
View
z
x
α
45
30
15
0
1
2
3
4
5
K = 0.098
t (C/U)

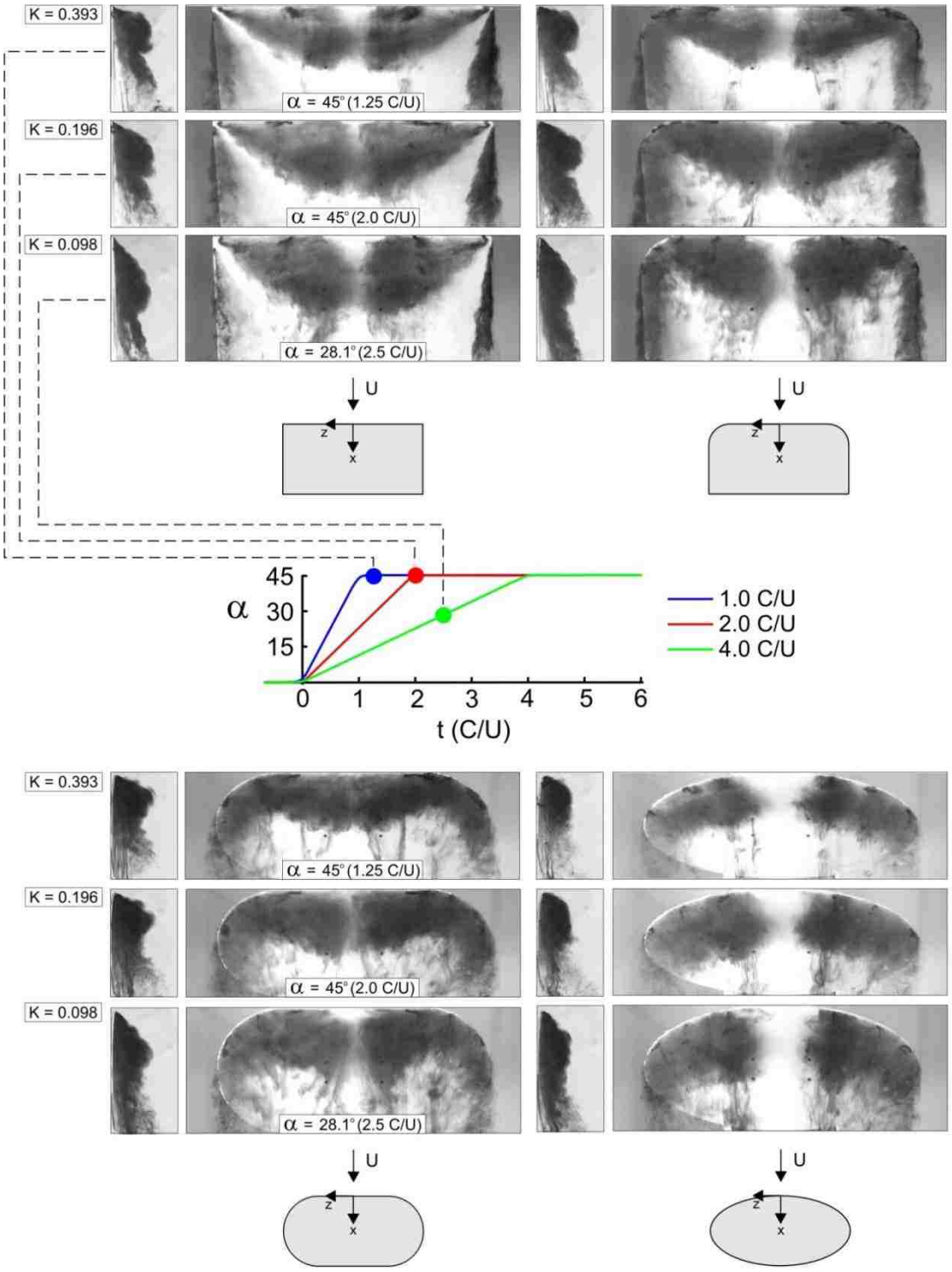

Figure 5.2.3: Side and plan views of dye visualization showing effect of magnitude of reduced frequency K = 0.098, 0.196, and 0.393 on flow structure. Pitch point x_p/C = 0.25.

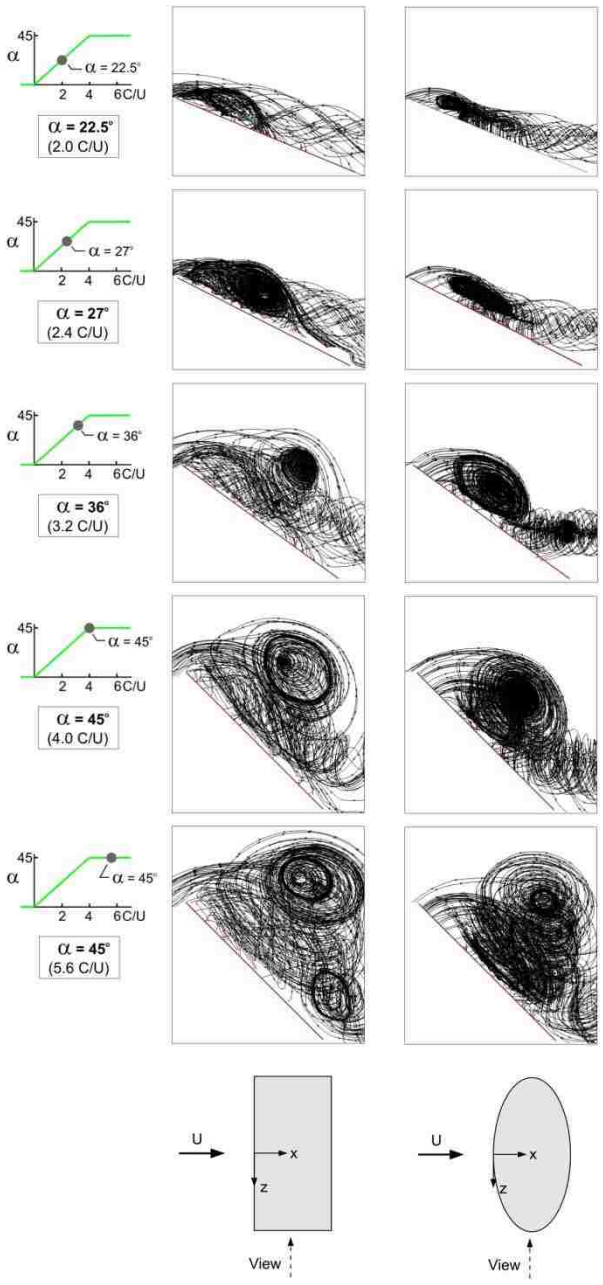

Figure 5.3.1a: Side views of three-dimensional streamline patterns as a function of angle of attack.

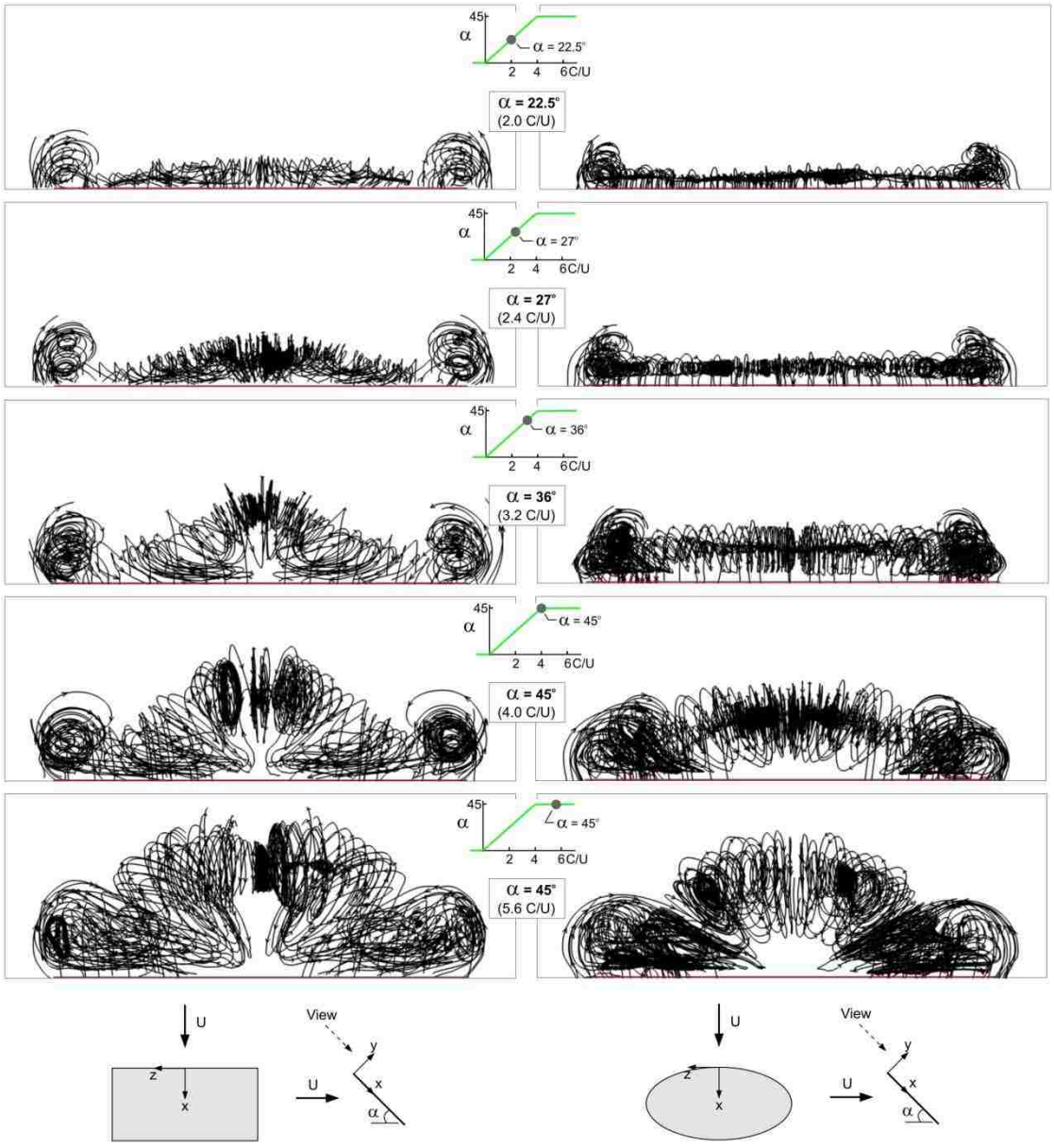

Figure 5.3.1b: End views of three-dimensional streamline patterns as a function of angle of attack.

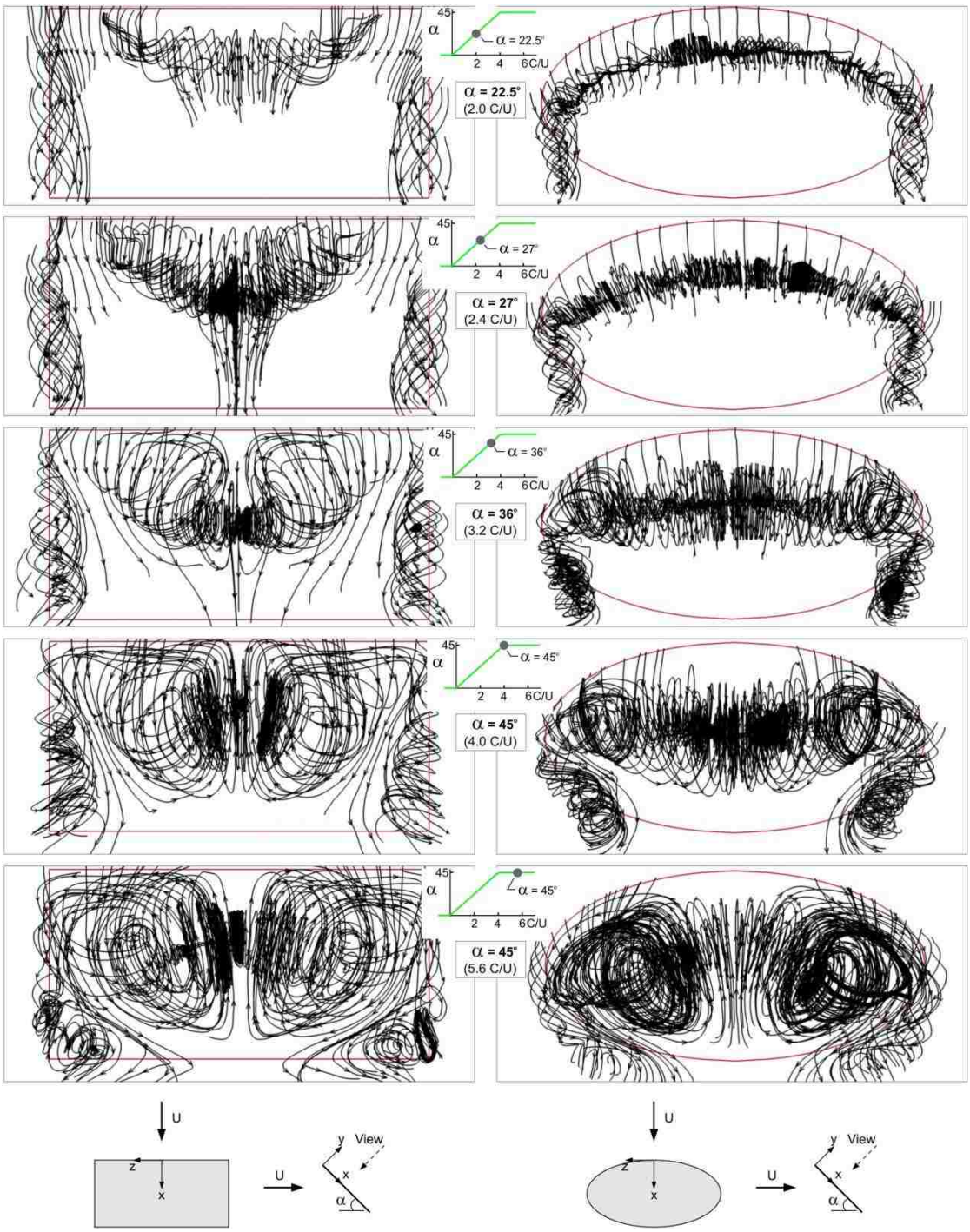

Figure 5.3.1c: Plan views of three-dimensional streamline patterns as a function of angle of attack.

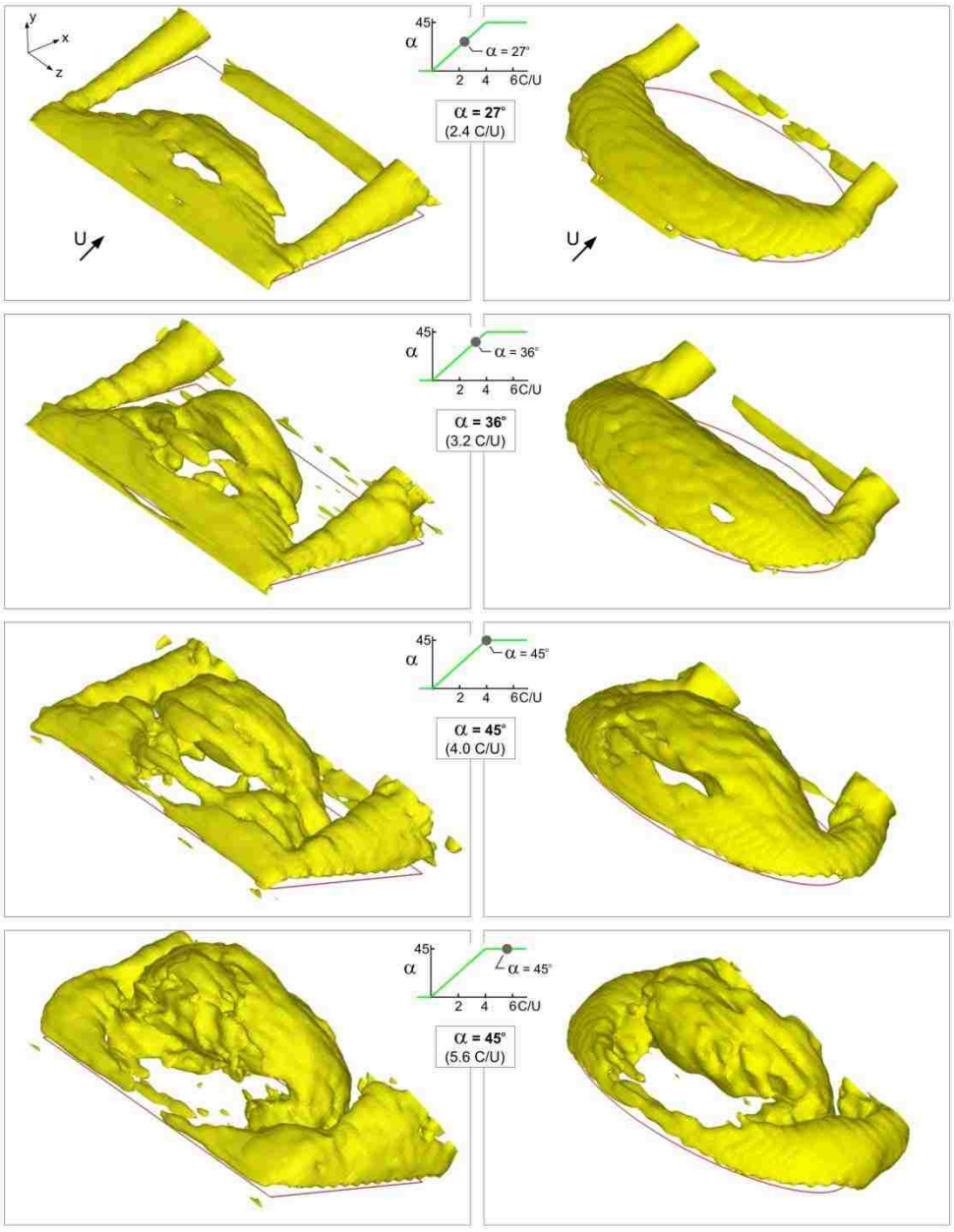

Figure 5.3.2a: Volumes of iso-Q as a function of angle of attack. Views are in the downstream direction, looking towards the leading-edge of the wing.

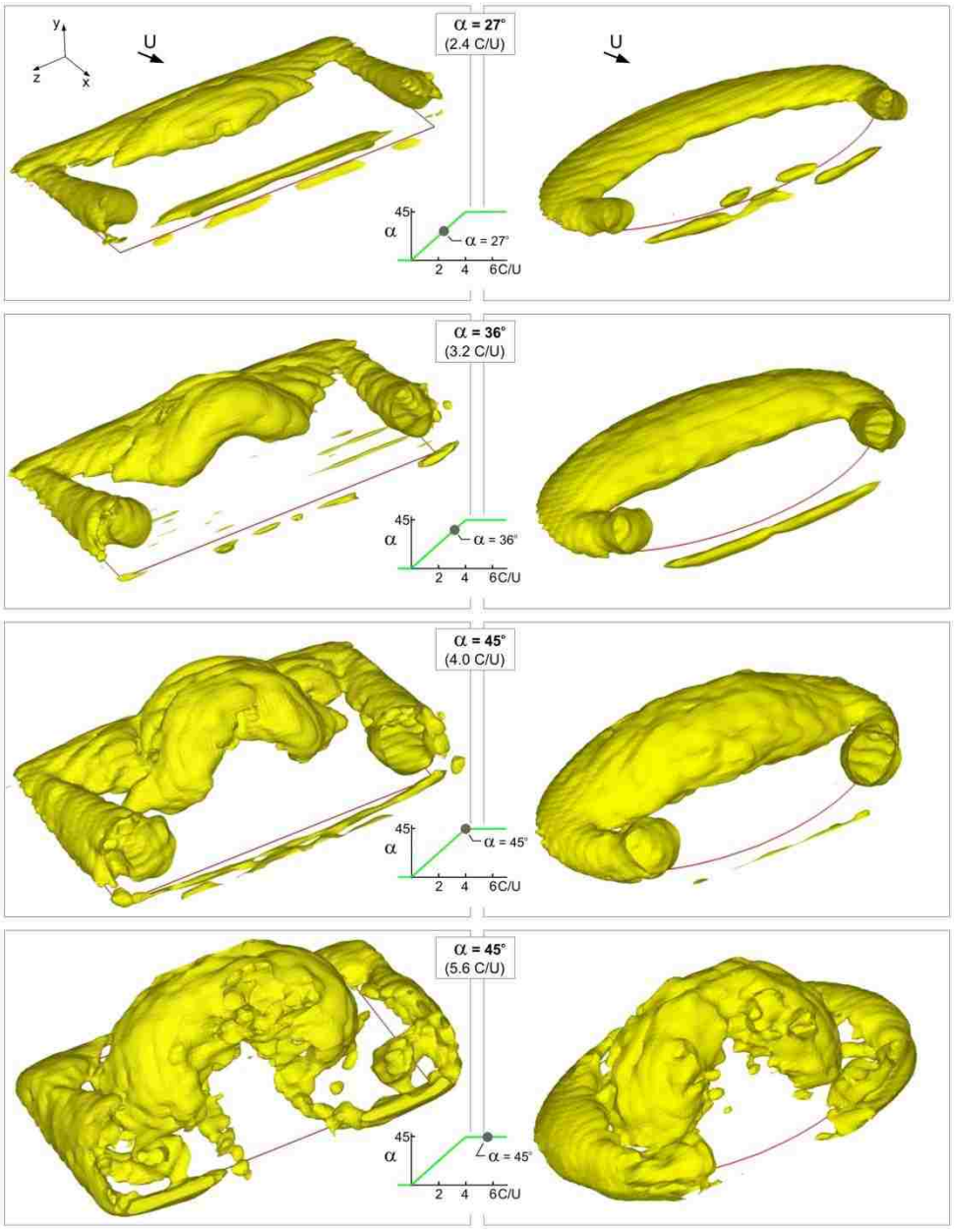

Figure 5.3.2b: Volumes of iso-*Q* as a function of angle of attack. Views are in the upstream direction, looking towards the trailing-edge of the wing.

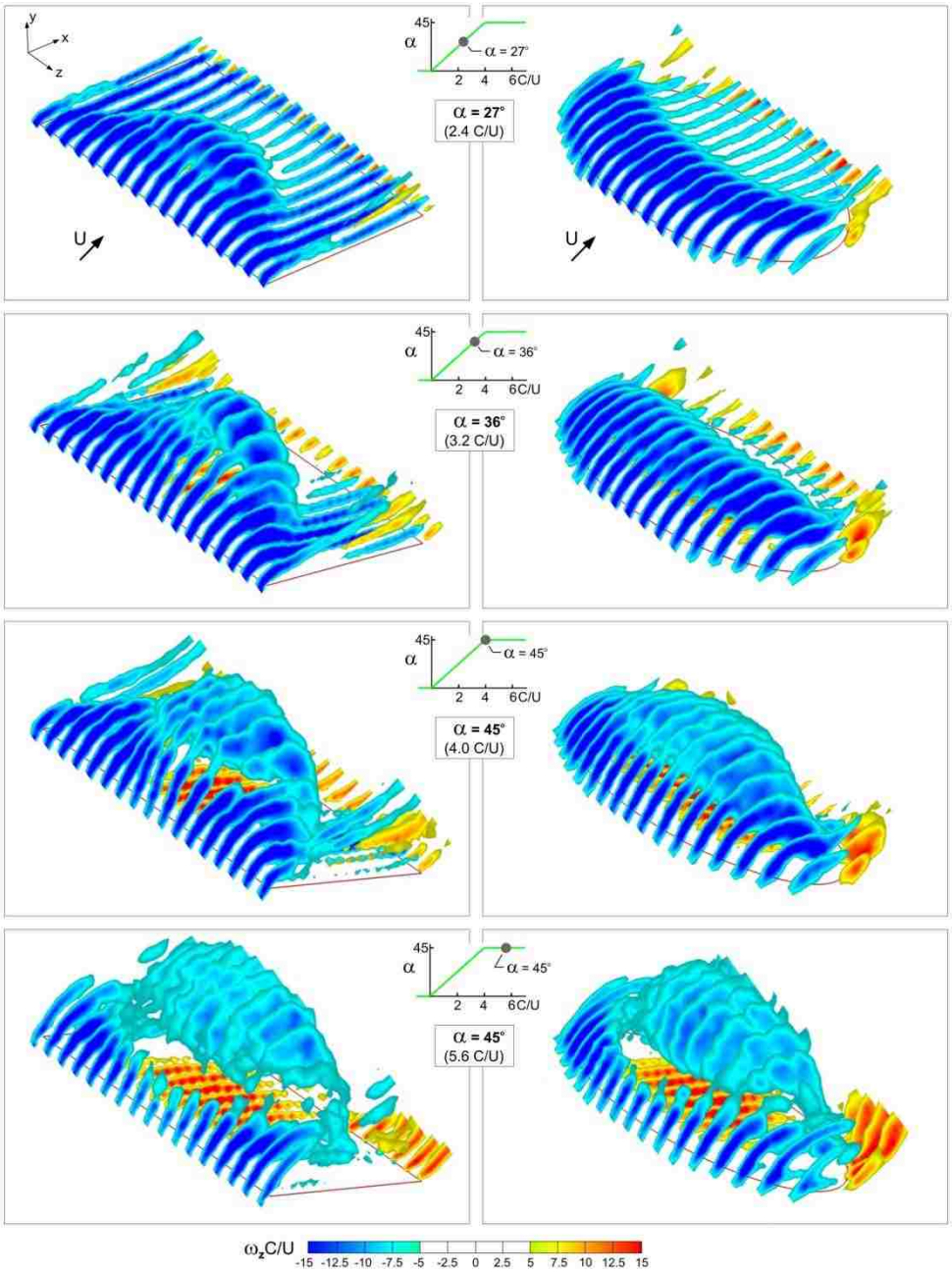

Figure 5.3.3a: Sectional cuts of spanwise vorticity as a function of angle of attack. Views are looking in the downstream direction, towards the leading-edge.

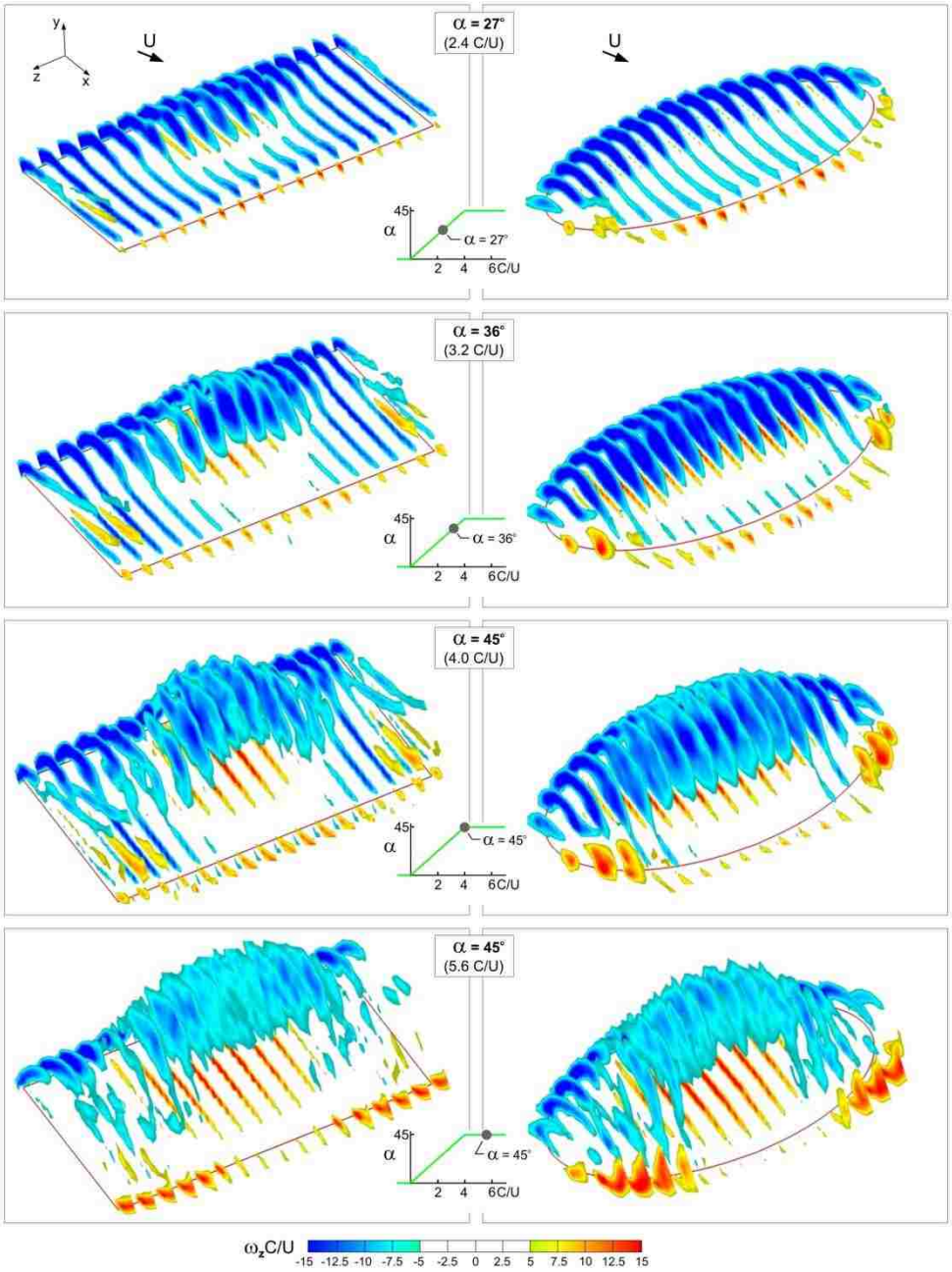

Figure 5.3.3b: Sectional cuts of spanwise vorticity as a function of angle of attack. Views are looking in the upstream direction, towards the trailing-edge.

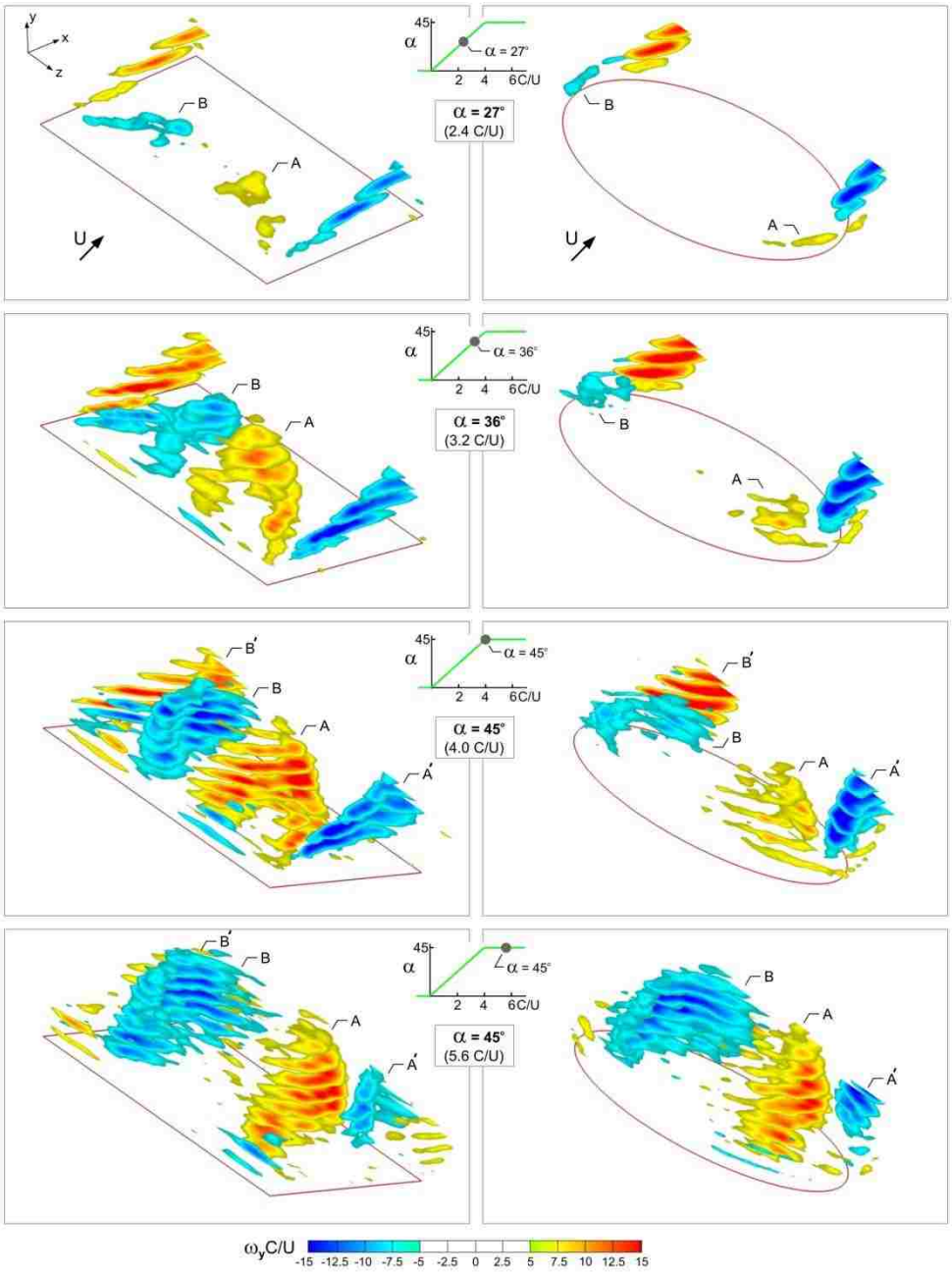

Figure 5.3.4a: Sectional cuts of surface-normal vorticity as a function of angle of attack. Views are looking in the downstream direction, towards the leading-edge.

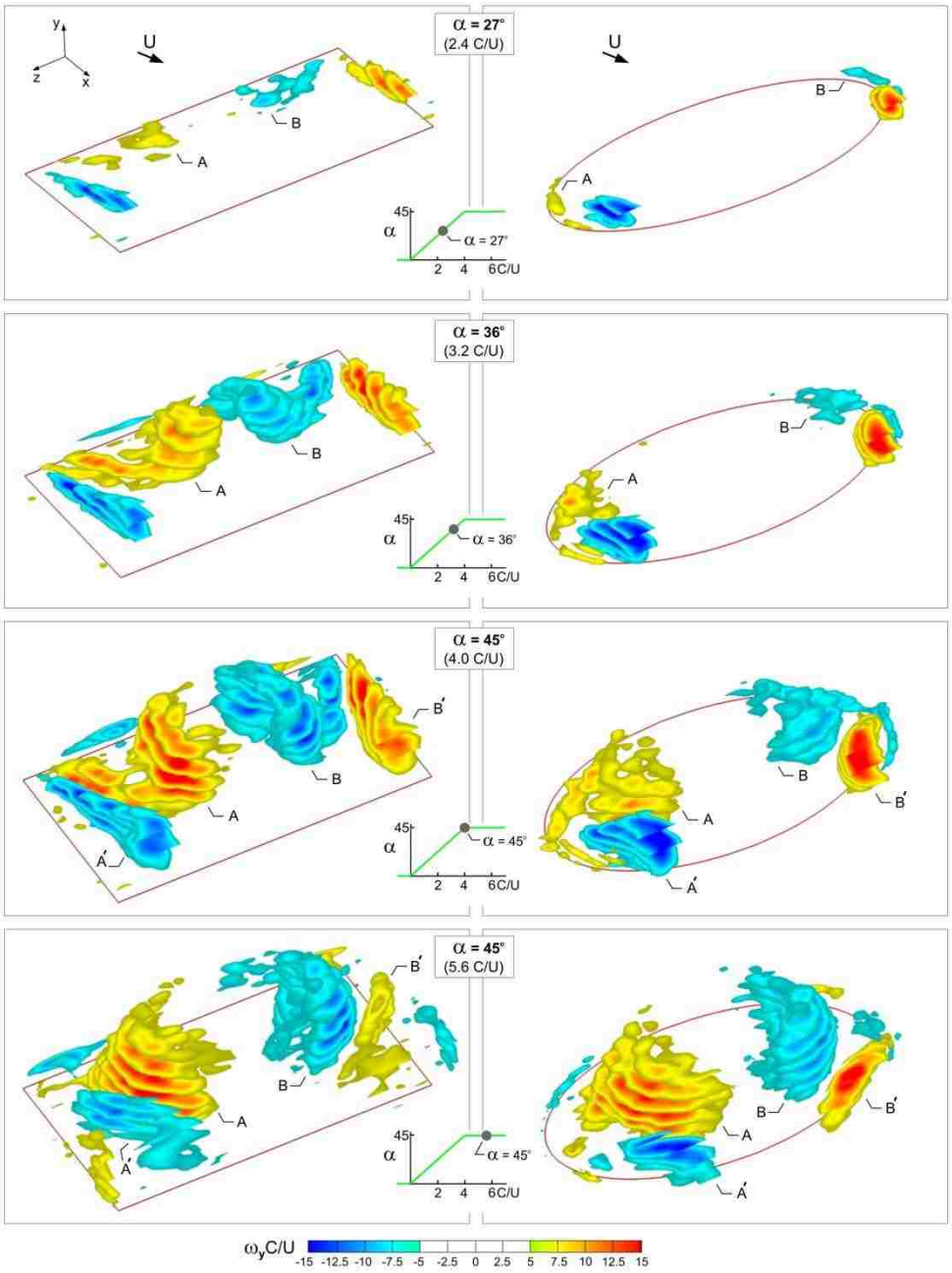

Figure 5.3.4b: Sectional cuts of surface-normal vorticity as a function of angle of attack. Views are looking in the upstream direction, towards the trailing-edge.

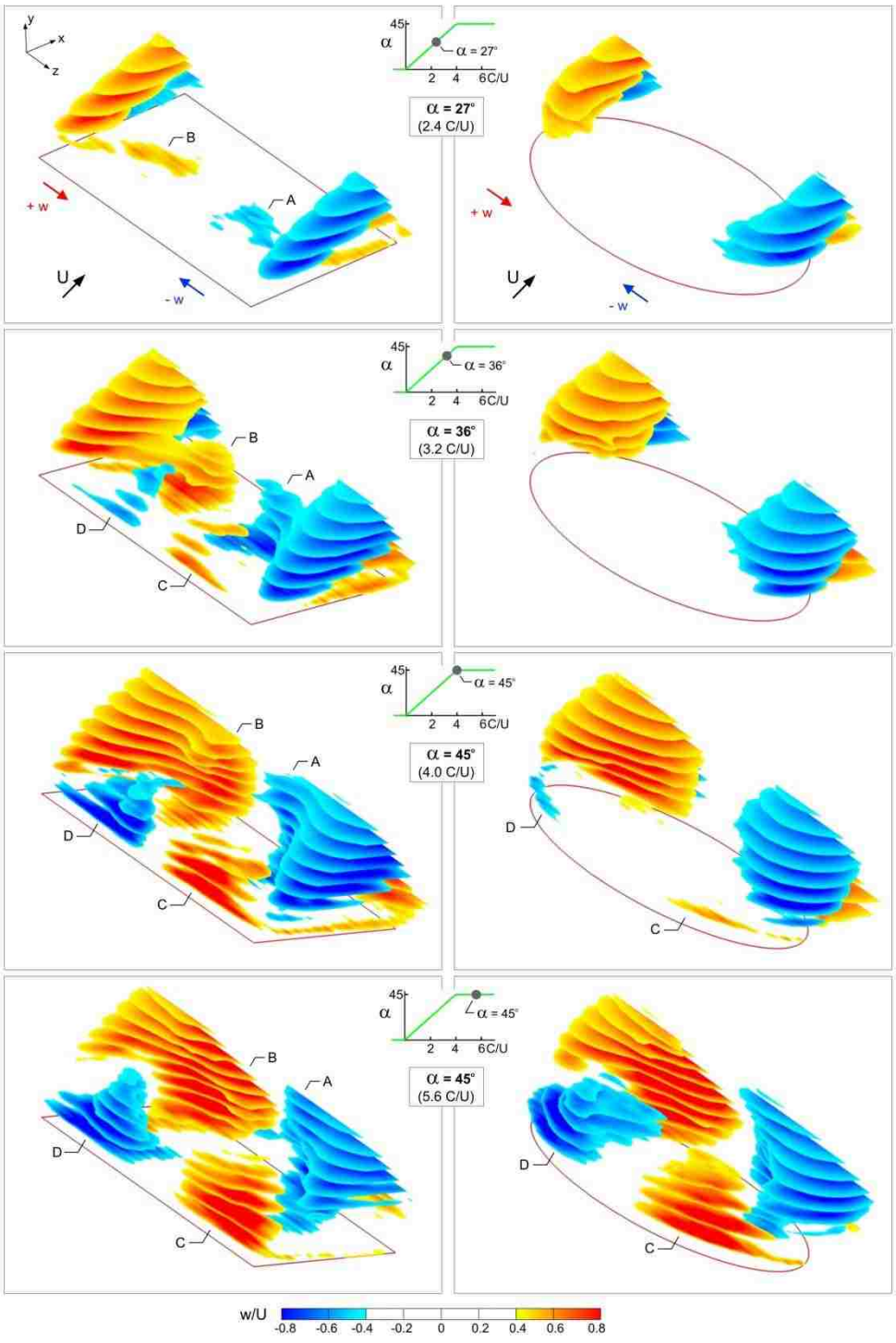

Figure 5.3.5: Slices of contours of constant spanwise velocity as a function of angle of attack. Views are looking in the downstream direction, towards the leading-edge.

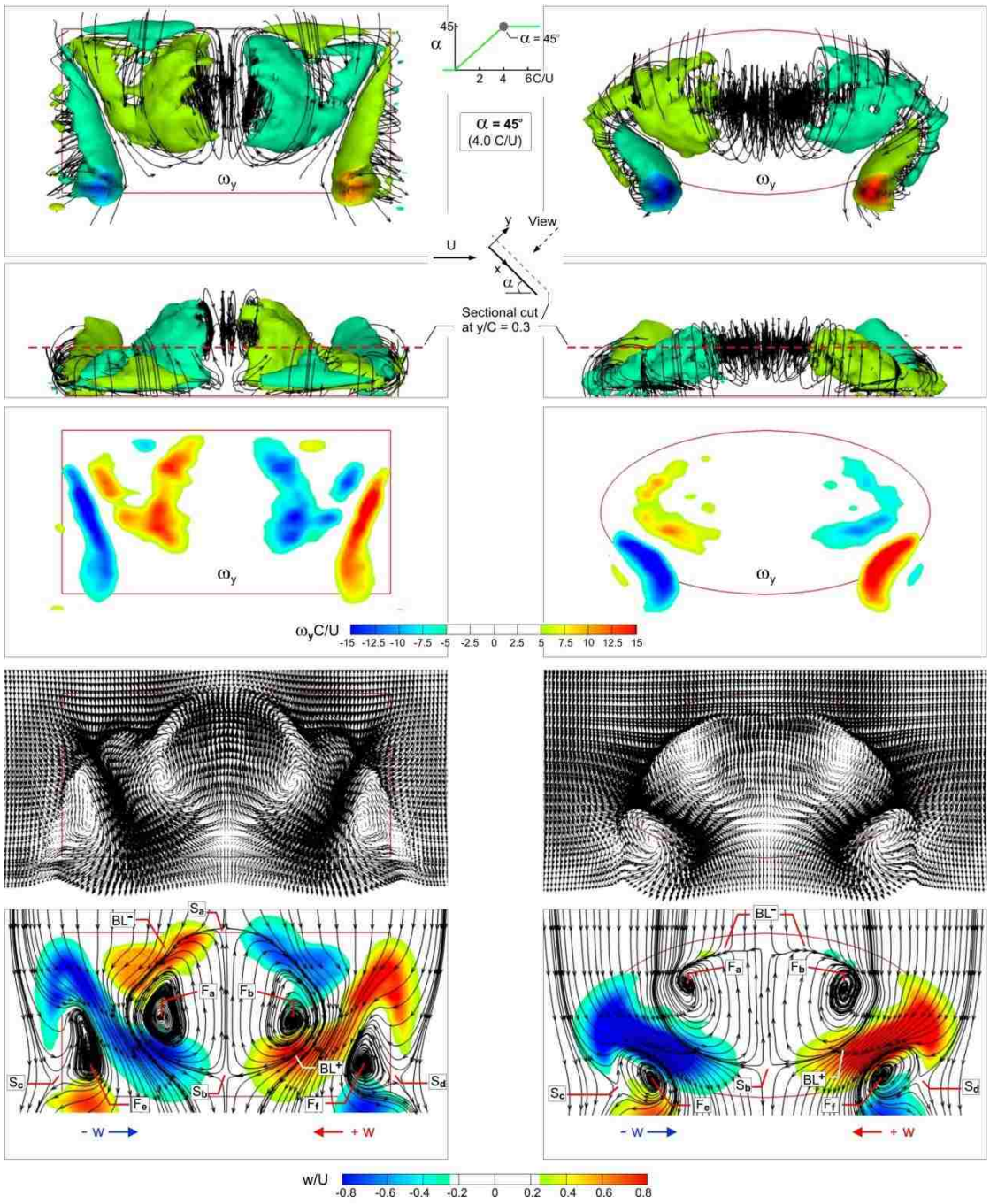

Figure 5.3.6a: Comparison of volumes of surface-normal vorticity superposed on three-dimensional streamlines (top two rows of images), sectional cuts of surface-normal vorticity (third row), velocity vectors (fourth row), and streamline topology with superposed contours of constant spanwise velocity (fifth row). Although the flow structure on the rectangular wing has approached its fully-evolved state, that on the elliptical wing is still developing.

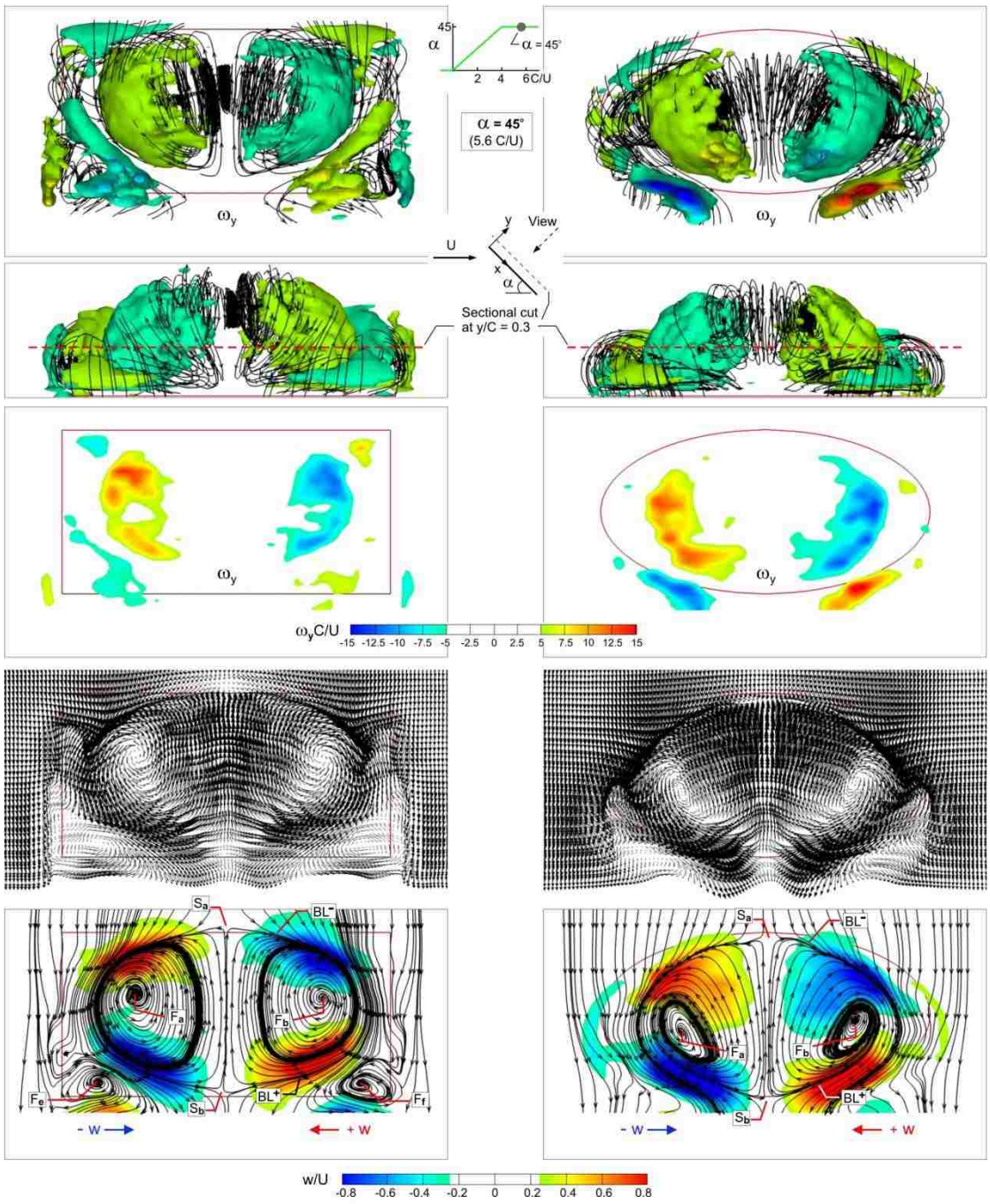

Figure 5.3.6b: Comparison of volumes of surface-normal vorticity superposed on three-dimensional streamlines (top two rows of images), sectional cuts of surface-normal vorticity (third row), velocity vectors (fourth row), and streamline topology with superposed contours of constant spanwise velocity (fifth row). Images correspond to the fully-evolved state of the flow structure on both the rectangular and elliptical wings.

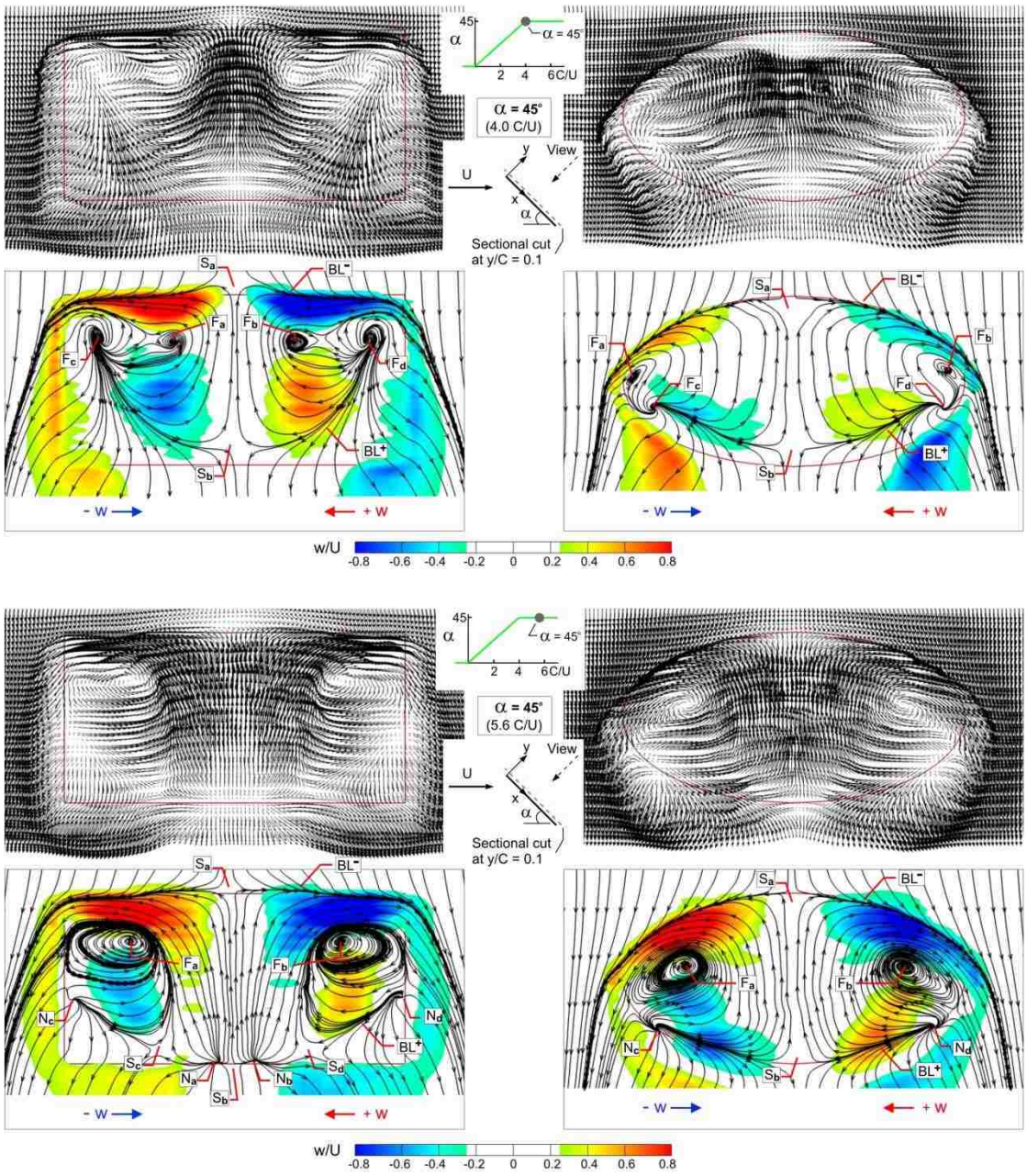

Figure 5.3.6c: Comparison of patterns of velocity vectors and streamlines topology superposed on contours of constant spanwise velocity at an elevation very close to the surface of the wing. Top two rows of images correspond to the instant where the flow structure on the rectangular wing has attained its fully-evolved state, while that on the elliptical wing is still under development. Bottom two rows of images correspond to the fully-evolved state of the flow structure on both wings.

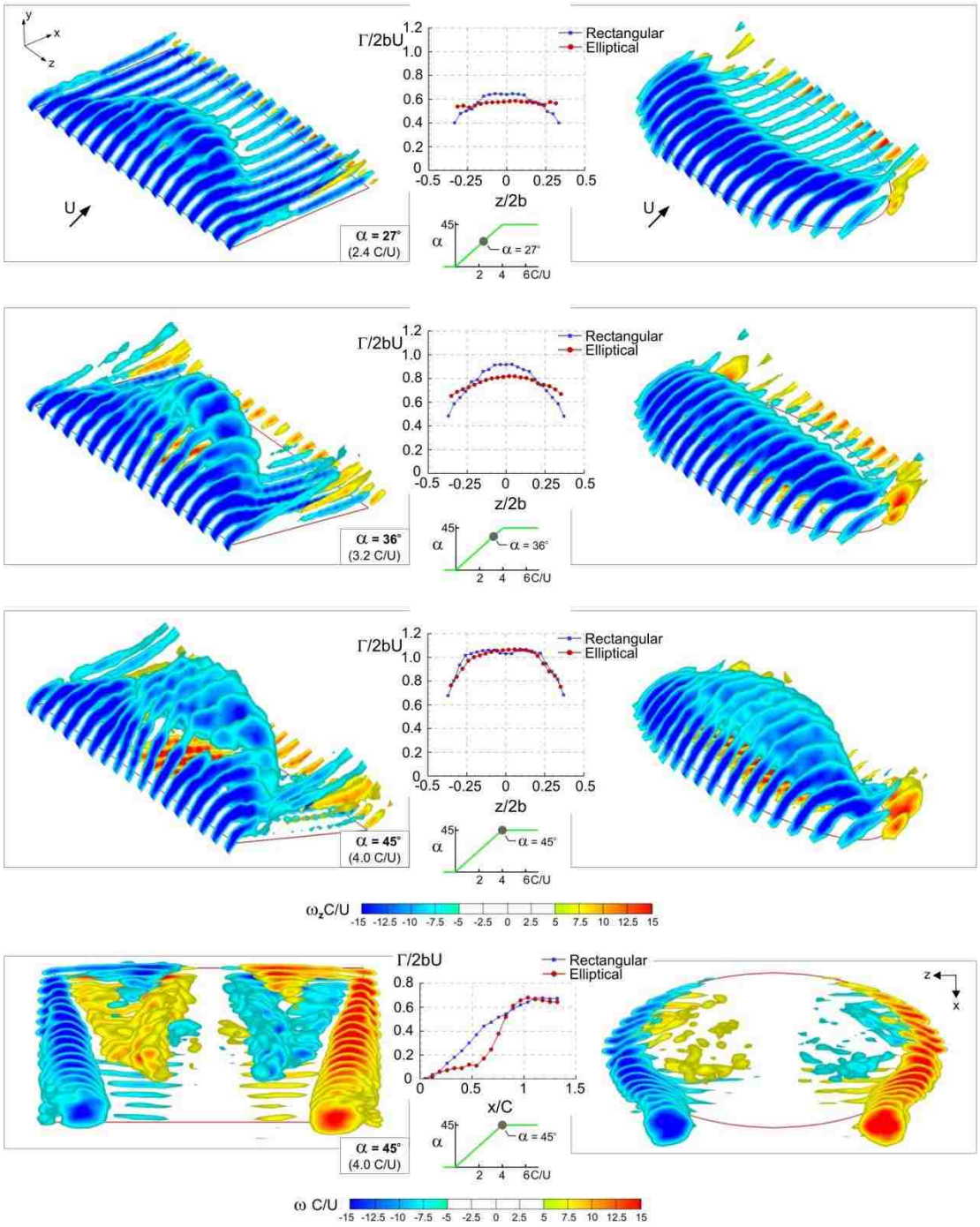

Figure 5.3.7: Sectional cuts of spanwise vorticity as a function of angle of attack (first three rows of images). Views are looking in the downstream direction, towards the leading-edge. Insets show circulation of leading-edge vortex. Sectional cuts of streamwise vorticity (fourth row of images). Inset shows circulation of tip vortices.

CHAPTER 6

CONCLUDING REMARKS AND RECOMMENDATIONS

6.1 SUMMARY

This investigation focused on characterization of the unsteady three-dimensional flow structure on low aspect ratio wings subjected to various generic maneuvers that are representative of nature-inspired flight. The maneuvers employed in this study were pitch-up motion to high angle of attack and periodic plunging motion. The flow structure arising from these maneuvers includes, but is not limited to, formation and development of a three-dimensional leading-edge vortex with pronounced axial flow, three-dimensional flow separation, formation of large-scale, surface-parallel swirl structures, and formation of three-dimensional tip vortices.

In order to gain further insight into the flow physics associated with the aforementioned flow structure, both qualitative (dye visualization) and quantitative (PIV, SPIV) measurement techniques were employed. These quantitative imaging techniques provided interpretation of the time evolution of the flow structure in terms

of sectional patterns of velocity vectors, velocity components, streamlines, and vorticity, in conjunction with volume images of phase-averaged patterns of *Q*-criterion, three-dimensional streamlines, and iso-surfaces of vorticity.

The first part of the present study provides dye visualization of the time evolution of the three-dimensional flow structure on a low aspect ratio rectangular wing subjected to two types of pure periodic plunging motion: triangular; and sinusoidal. In the second part, the three-dimensional unsteady flow structure arising from periodic sinusoidal plunging motion was investigated using a technique of stereoscopic particle image velocimetry (SPIV). In the third and final part, the three-dimensional flow structure and topology on wings subjected to a smoothed linear ramp-like pitching motion were addressed. Different configurations of low aspect ratio wings were studied using dye visualization and stereoscopic particle image velocimetry (SPIV).

Concluding remarks for each of these phases of investigation are given in the following.

6.1.1 Flow Structure on a Low Aspect Ratio Plunging Wing

The time evolution of the unsteady flow patterns on various cross-flow planes along a plunging rectangular wing of aspect ratio AR = 2 at an angle of attack $\alpha = 8°$ were investigated via techniques of particle image velocimetry and dye visualization. Two types of periodic plunging motion, at a reduced frequency $k = \pi fC/U = 1.0$ and amplitude $h = 0.25C$, were employed in order to clarify how the flow structure is affected by the type of motion, i.e. ramp-like motion with constant velocity and sinusoidal motion with accelerating/decelerating velocity. The time sequences of the

cross-flow images were interpreted with instantaneous and phase-averaged contours of spanwise velocity, streamwise vorticity, and velocity vectors. In order to gain a deeper understanding of the evolution of the three-dimensional flow structure, the circulation was calculated at various instants of time during the plunge cycle.

In summary, the timewise development of the patterns of dye shows the transformation from pronounced axial flow in the nascent leading-edge vortex to well-defined, streamwise-oriented vortical structures located near the plane of symmetry of the wing, clarified by quantitative images. Moreover, additional images emphasize that abrupt changes of the three-dimensional flow structure can occur over a small time scale, i.e., a fraction of the oscillation cycle. These findings indicate that the effect of the mid-plane vortices on the total circulation should be accounted for, even though the tip vortices yield the largest positive contribution to the total circulation. The time sequence of instantaneous and phase-averaged images shows that the principal features of the flow structure are preserved for two basic types of motion: successive positive-negative ramps; and sinusoidal motion. This type of three-dimensional vortex formation is expected to be a generic feature of wings undergoing unsteady maneuvers in various modes, where significant accelerations of the leading-edge lead to generation of a pronounced leading-edge vortex. Finally, for both types of plunging motion employed in this study, the overall flow features are found to be indistinguishable over the Reynolds number range from 5,000 to 20,000.

6.1.2 Time Evolution of Three-dimensional Flow Structure on a Low Aspect Ratio Wing Subjected to Sinusoidal Plunge Maneuver

The complex unsteady flow structure over a plunging low aspect ratio rectangular wing was investigated using techniques of stereoscopic particle image velocimetry. The wing was subjected to a sinusoidal plunging motion at a reduced frequency $k = \pi fC/U = 1.0$ and amplitude $h = 0.25C$. The time sequences of the volume images of the flow structure were interpreted in conjunction with three-dimensional streamline patterns, iso-Q surfaces, contours of vorticity projections in orthogonal directions, spanwise velocity, velocity vectors, and streamline topology on cross-sectional planes.

First of all, this investigation shows that the flow patterns on plunging low aspect ratio wings have complex, unsteady, highly three-dimensional characteristics, which sets them apart from the classical, quasi two-dimensional flows along wings of large aspect ratio. These unique characteristics of the time evolution of the flowfield involve:

1. Presence of a pronounced axial flow in the nascent leading-edge vortex during its initial stages of development (first half of the downstroke).

2. Evolution of the leading-edge vortex system into a Λ-shaped formation, whose legs are pinned at the front corners of the wing, observed at $\alpha_{eff} = 27.5°$ ($t/T = 0.125$).

3. Detachment of the Λ-shaped vortex from the corners of the tip, movement of its legs towards the plane of symmetry, and formation of the surface-parallel swirls

near the surface of the wing, which is evident at the end of downstroke α_{eff} = 8.1° (t/T = 0.25).

4. Evolution of the Λ-shaped formation into an arch-type vortex structure during the initial stages of the upstroke.

5. Downstream propagation of the arch vortex, and movement of its legs toward the wing centerline during the upstroke.

6. Reconnection of the legs of the arch vortex at the end of upstroke, and its shedding from the trailing-edge in a ring-like form as the next plunging cycle begins.

In addition to the flow structure described above, the wing tip vortices follow a process including formation, breakdown, total collapse, and reformation at various stages of the plunging cycle, which have been also observed in the computational results (Visbal, 2011).

Furthermore, the experimental flow visualizations are compared with the high resolution computational visualizations, performed by the US Air Force Research Laboratory. The patterns of the flow structure show very similar characteristics for both studies. In addition to flow visualizations, the relationship between the three-dimensional flow structure and lift coefficient is investigated. A smooth distribution of lift coefficient is observed, and no evidence of deep stall is found during the oscillation cycle. Moreover, the computations indicate that the Reynolds number has a limited effect on the lift coefficient.

6.1.3 Three-dimensional Representation of Time Evolution of Flow Structure on Various Low Aspect Ratio Wing Configurations Subjected to Pitch up Maneuver

Low aspect ratio wings undergoing pitch-up motion to high angle of attack give rise to the onset and development of three-dimensional vortical structures that converge to a well-defined state. The time evolution of these structures was characterized using techniques of stereoscopic particle image velocimetry and dye visualization. Evolution of the three-dimensional leading-edge vortex formation, effects of wing geometry and pitch rate on the flow structure were addressed via dye visualization. Time sequences of volume images provide interpretation of the three-dimensional flow structure in conjunction with three-dimensional streamline patterns, iso-Q surfaces, contours of vorticity projections in orthogonal directions, spanwise velocity, velocity vectors, and circulation as well as streamline topology on cross-sectional planes. The principal findings of this aspect of the investigation are described in the following.

A fully-evolved state of the flow structure is approached after attainment of the maximum angle of attack. The large-scale vortical structures on the wing take a form that is relatively independent of the wing planform. Near the surface of the wing, large-scale swirl patterns of opposite sense occur on either side of the plane of symmetry of the wing; each swirl occupies nearly the entire semispan. Correspondingly, volumes of surface-normal vorticity occur within each of these regions. Near and at the plane of symmetry, however, at elevations well above the surface of the wing, spanwise vorticity dominates.

In this fully-evolved state, the large-scale swirl near the surface of the wing, which is parallel to the wing surface, involves large magnitudes of spanwise velocity. Near the leading-edge of the wing, the spanwise velocity is away from the plane of symmetry and near the trailing edge of the wing, it is towards the plane of symmetry. These spanwise velocity magnitudes can be nearly as large as the freestream velocity. Moreover, the associated (surface parallel) streamline topology shows similar types and locations of critical points, i.e., foci, bifurcation lines and saddle points, at elevations above the wing surface, irrespective of which of the extreme planforms, rectangular versus elliptical, is considered. The large-scale swirl involves a well-defined focus at the center of the swirl streamline pattern, which may be either stable or unstable. At the surface of the planform, however, the streamline topology shows distinguishable differences, which are dependent upon planform geometry, as it adapts to the local wing configuration.

The initial stages of vortex development and distortion that eventually lead to the fully-evolved state described in the foregoing are, however, strongly dependent upon the occurrence or nonoccurrence of axial flow within the leading-edge vortex, and thereby are dependent on the planform of the wing. The initial stage of formation of the leading-edge vortex on the rectangular wing involves formation of opposing, small-scale vortices having axial and circumferential components, and emanating from the straight leading-edge of the wing, located at 28 percent of the semi-span on either side of the plane of symmetry of the wing; in contrast, formation of the leading-edge vortex from the elliptical wing does not involve a mechanism for generation of axial flow. When such axial flow occurs within the leading-edge vortex, as is the case on

the rectangular wing, it is oriented towards the plane of symmetry of the wing, and gives rise to rapid displacement of the central portion of the vortex (located near the plane of symmetry of the wing) away from the wing surface, thereby causing severe vortex distortion. A further, important consequence of axial flow within the leading-edge vortex is as follows. Due to interaction of opposing axial flows at the plane of symmetry, it leads, in that region, to the rapid onset of swirl oriented parallel to the surface of wing. This surface-parallel swirl is, in turn, associated with the rapid development of volumes of surface normal vorticity on either side of the plane of symmetry of the wing. The scale of these volumes increases with time, as they move away from the plane of symmetry. If, however, axial flow does not occur within the leading-edge vortex, the patterns of surface-parallel swirl and corresponding clusters of surface normal vorticity are first evident near the tips of the wing and, with increasing time, they increase in scale while moving towards the plane of symmetry. This case of insignificant axial flow within the leading-edge vortex is associated with a substantial time lag for onset of the fully-evolved state of the three-dimensional vortex system, relative to the case where substantial axial flow occurs.

The traditional interpretation of the flow structure on a wing of large span undergoing pitch up motion to high angle of attack involves the large-scale, quasi-two-dimensional leading-edge vortex, i.e., the dynamic stall vortex. For low aspect ratio wings, the foregoing observations indicate that the flow structure is highly three-dimensional, with pronounced regions of surface-normal vorticity and surface-parallel swirl that are orthogonal to the vorticity and swirl of the classical large-scale leading-edge vortex. This three-dimensionality has important consequences for the variation of

spanwise vorticity of the leading-edge vortex along the span of the wing. Sectional cuts of spanwise vorticity show, for the asymptotic state, remarkably similar spanwise variations; only near the plane of symmetry do large-scale regions of spanwise vorticity exist, with relatively large values of circulation. Moreover, these spanwise variations of sectional cuts of spanwise vorticity show a rapid approach to the fully-evolved state of the flow structure when pronounced spanwise velocity occurs in the leading-edge vortex, relative to the case where insignificant spanwise flow occurs.

The overall nature of the flow structure characterized in this investigation has broad similarities, or analogies, with recent investigations. Taira and Colonius (2009a) computed the evolution of the three-dimensional vortex structure on an impulsively-translated wing and observed the onset of a vortex loop, particularly in the vicinity and downstream of the trailing-edge of the wing. Visbal (2011) computed the flow structure on a plunging rectangular wing and characterized an arch vortex during the final stages of three-dimensional development; it is more compact than the analogous structure characterized herein. That is, in the investigation of Visbal (2011), the distance between the legs of the arch vortex and their characteristic diameter are much smaller than the analogous vortical structures characterized herein; a common feature, however, involves spanwise velocities of large magnitude oriented away from the plane of symmetry of the wing near the leading-edge and towards the plane of symmetry near the trailing-edge of the wing. For the limiting case of steady flow past a flat plate at sufficiently high angle of attack, Visbal (2011) reveals the onset of swirl parallel to the wing surface, where the centers of swirl are at the leading-corners of the wing. These previous investigations, taken together with the present study, suggest

generic features of the three-dimensional vortex structure on wings undergoing various types of motion.

6.2 RECOMMENDATIONS FOR FUTURE RESEARCH

The present study has led to understand the flow physics involved in various generic maneuvers of nature-inspired flight, i.e., pitch-up motion of a wing to high angle of attack, and periodic plunging motion. The results presented in this study provide a basis for future investigations involving in design and development of micro-aerial vehicles and small unmanned air vehicles.

In the present investigation, only pitch-up and plunging motion have been employed, and the three-dimensional flow structure arising from these motions has been extensively investigated. In order to gain further insight into the flow physics associated with the nature-inspired flight, other basic classes of motions including flapping, revolving (rotating), and combinations of pitching and plunging, should be considered, and the flow structure on finite-span wings subjected to these motions should be investigated using advanced global imaging techniques such as SPIV.

This study has focused on the characterization of the flow structure. However, in order to improve design and development of nature-inspired micro-aerial vehicles, the relationship between the flow structure and the associated aerodynamic forces needs to be clarified. Further experiments involving simultaneous force measurements, for different types of prescribed motion of the wing, can lead to an understanding of the associated aerodynamic forces.

The effect of aspect ratio on the flow structure and loading deserves further attention. While (Blondeaux et al, 2005) assert that the three-dimensional flow along

finite span wings having an aspect ratio greater than four can be successfully derived from two-dimensional considerations, this assumption is inadequate for a thorough understanding of the unsteady aerodynamics associated with the low aspect ratio wings operating at low Reynolds numbers (Kunihiko, 2009). The present study has also shown that the flow structure on maneuvering wings of finite-span has a complex and highly three-dimensional form, which makes it completely different from the corresponding two-dimensional case. In addition, (Taira and Colonius, 2009a) have shown that aspect-ratio and angle of attack have a large influence on the three-dimensional flow structure and the aerodynamic forces on finite-span wings. The aspect ratio of each wing configuration employed in the present study was $AR = 2$. However, the flow structure on the wings with different aspect ratio needs to be investigated in the future studies.

Recent studies have shown that the flow structure and the aerodynamic forces on a maneuvering wing are dependent upon the history of its motion. Therefore, the kinematic parameters of the motion, i.e. frequency and reduced ramp rate, become key factors that should be considered during further investigations of low aspect ratio wings.

REFERENCES

Alkislar, M. B., Lourenco, L. M. and Krothapalli, A. 2000 "Stereoscopic PIV Measurements of a Screeching Supersonic Jet", *Jounal of Visualization*, Vol. 3, No. 2, pp. 135-143.

Baik, Y. C., Rausch, J. M., Bernal, L. P. and Ol, M. V. 2009 "Experimental investigation of pitching and plunging airfoils at Reynolds number between $1x10^4$ and $6x10^4$", *AIAA Paper*, 2009-4030.

Baik, Y. C., Bernal, L. P., Shyy, W. and Ol, M. V. 2011 "Unsteady force generation and vortex dynamics of pitching and plunging flat plates at low Reynolds number", *AIAA Paper*, 2011-220.

Birch, J. M. and Dickinson, M. H., 2001 "Spanwise flow and the attachment of the leading-edge vortex on insect wings", *Nature*, Vol. 412, pp. 729-733.

Blondeaux, P., Fornarelli, F., Guglielmini, L, Triantafyllou, M. S., Verzicco, R., 2005 "Vortex structures generated by a finite-span oscillating foil", in *43rd AIAA Aerospace Sciences Meeting*, Reno, Nevada.

Bohl, D. G. and Koochesfahani, M. M. 2004 "MTV measurements of axial flow in a concentrated vortex core", *Physics of Fluids*, Vol. 16, pp. 4185-4191.

Brunton, S. L., Rowley, C. W., Taira, K., Colonius, T., Collins, J. and Williams, D. R. 2008 "Unsteady aerodynamic forces on small-scale wings: Experiments, simulations, and models", *AIAA Paper*, 2008-520.

Buchholz, J. H. J. and Smits, A. J. 2006 "On the evolution of the wake structure produced by a low-aspect-ratio pitching panel", *Journal of Fluid Mechanics*, Vol. 546, pp. 433–443.

Buchner, A. -J, Buchmann, N. A. and Soria, J. 2010 "Wake measurements of a pitching plate using multi-component, multi-dimensional PIV techniques", *AFMC Paper*, 2010-221.

Carr, L. W. 1988 “Progress in analysis and prediction of dynamics stall”, *Journal of Aircraft*, Vol. 25, pp. 6-17.

Cohn, R. K. and Koochesfahani, M. M. 1993 “Effect of boundary conditions on axial flow in a concentrated vortex core”, *Physics of Fluids*, Vol. 5, pp. 280-282.

Coudert, S. J. M. and Schon, J. P. 2001 “Back projection algorithm with misalignment corrections for 2D3C stereoscopic PIV”, *Measurement Science and Technology*, Vol. 12, pp. 1371-1381.

Dong, H., Mittal, R. and Najjar, F. M. 2006 “Wake topology and hydrodynamic performance of low-aspect-ratio flapping foils”, *Journal of Aircraft*, Vol. 566, pp. 309-343.

Eldredge, J. D., Wang, C. and Ol, M. V. 2009 “A computational study of a canonical pitch-up, pitch-down wing maneuver”, *AIAA Paper*, 2009-3687.

Ellenrieder, K. D., Parker, K., Soria, J. 2003 “*Flow structures behind a heaving and pitching finite-span wing*”, *Journal of Fluid Mechanics*, Vol. 490, pp. 129-138.

Freymuth, P. 1989 “Visualizing the Connectivity of Vortex Systems for Pitching Wings”, *Journal of Fluids Engineering*, Vol. 111, pp. 217-220.

Geers, L. F. G., Tummers, M. J. and Hanjalic, K. 2005 “Particle imaging velocimetry-based identification of coherent structures in normally impinging multiple jets”, *Physics of Fluids*, Vol. 17, pp. 1-13.

Giordano, R., Astarita, T. 2009 “Spatial resolution of the Stereo PIV technique”, *Experiments in Fluids*, Vol. 46, pp. 643-658.

Granlund, K., Ol, M. V. and Bernal, L. 2011 “Experiments on pitching plates: Force and flowfield measurements at low Reynolds numbers”, *AIAA Paper*, 2011-872.

Green, M. A., Rowley, C. W. and Haller, G. 2007 “Detection of Lagrangian coherent structures in three-dimensional turbulence”, *Journal of Fluids Engineering*, Vol. 572, pp. 111-120.

Hill, M. J. M. 1894 “On a spherical vortex”, *Philos. T. R. Soc. Lond.*,Vol. 185, pp. 213-245.

Hunt, J. C. R., Wray, A. A. and Moin, P. 1988 “Eddies, stream, and convergence zones in turbulent flows”, *Center for Turbulence Research Rep*. CTR-S88.

Jian, T. and Ke-Qin, Z., 2004 “Numerical and experimental study of flow structure of low-aspect-ratio wing”, *Journal of Aircraft*, Vol. 41, No. 5, pp. 1196-1201.

Kang, C., Baik, Y. S., Bernal, L., Ol, M. V. and Shyy, W., 2009 "Fluid dynamics of pitching and plunging airfoils of Reynolds number between $1x10^4$ and $6x10^4$", in *48th AIAA Aerospace Sciences Meeting*, Orlando, Florida.

Koochesfahani, M. M. 1989 "Vortical patterns in the wake of an oscillating airfoil", *AIAA Journal,* Vol. 27, pp. 1200-1205.

Lehmann, F. O. 2004 "The mechanisms of lift enhancement in insect flight", *Naturwissenschaften*, Vol 91, pp. 101-122.

Lentink, D. and Dickonson, M. H. 2009b "Rotational accelerations stabilize leading edge vortices on revolving fly wings", *Journal of Experimental Biol*ogy, Vol. 212, pp. 2705-2719.

Mccroskey, W. J., Carr, L. W. and Mcalister K. W. 1976 "Dynamic stall experiments on oscillating airfoils", *AIAA Journal,* Vol. 14, pp. 57-63.

Mccroskey, W. J. 1982 "Unsteady airfoils", *Annual Review of Fluid Mechanics,* Vol. 14, pp. 285–311.

Ohmi, K., Coutanceau, M., Daube, O. and Ta Phuoc Loc 1991 "Further experiments on vortex formation around an oscillating and translating airfoil at large incidences", *Journal of Fluid Mechanics,* Vol. 225, pp. 607-630.

Ol, M. V., Bernal, L., Kang, C. K. and Shyy, W. 2009 "Shallow and deep dynamic stall for flapping low Reynolds number airfoils", *Experiments in Fluids*, Vol. 46, pp. 883–901.

Ol, M. V., Altman, A., Eldredge, J. D., Garmann, D. J. and Lian, Y. 2010 "Résumé of the AIAA FDTC low Reynolds number discussion group's canonical cases", *AIAA Paper*, 2010-1085.

Parker, K., Von Ellenrieder, K. D. and Soria, J. 2007 "Morphology of the forced oscillatory flow past a finite-span wing at low Reynolds number", *Journal of Fluid Mechanics*, Vol. 571, pp. 327–357.

Parker, K., Von Ellenrieder, K. D. and Soria, J. 2005 "Using stereo multi-grid DPIV measurements to investigate the vertical skeleton behind a finite-span flapping wing", *Experiments in Fluids*, Vol. 39, pp. 281–298.

Prasad, A.K. 2000 "Stereoscopic Particle Image Velocimetry", *Experiments in Fluids*, Vol. 29, pp. 103-116.

Prasad, A. K. and Kirk, J. 1995 “Scheimpflug stereocamera for particle image velocimetry in liquid flows”, *Applied Optics*, Vol. 34, No. 30, pp. 7092-7099.

Prasad, A. K. and Adrian, R. J. 1993 “Stereoscopic particle image velocimetry applied to liquid flows”, *Experiments in Fluids*, Vol. 15, pp. 49-60.

Raffel, M., Willert, C.E. and Kompenhans, J. 2008 “Particle Image Velocimetry: A Practical Guide”, Springer, Berlin.

Robinson, O. and Rockwell, D. 1993 “Construction of three-dimensional images of flow structure via particle tracking techniques”, *Experiments in Fluids*, Vol. 14, pp. 257–270.

Sane, S. P. 2003 “The aerodynamics of insect flight”, *Journal of Experimental Biology*, Vol. 206, pp. 4191-4208.

Scarano, F., David, L., Bsibsi, M. and Calluaud, D. 2005 “S-PIV comparative assessment: image dewarping+misalignment correction and pinhole+geometric back projection”, *Experiments in Fluids*, Vol. 39, pp. 257-266.

Shyy, W., Lian, Y., Tang, J., Liu, H., Trizila, P., Stanford, B., Bernal, L., Cesnik, C., Friedmann, P. and Ifju, P. 2008 “Computational aerodynamics of low Reynolds number plunging, pitching and flexible wings for MAV applications”, *Acta Mechanica Sinica*, Vol. 24, pp. 351-373.

Shyy, W., Aona, H., Chimakurthi, S. K., Trizila, P., Kang, C. -K., Cesnik, C. E. S. and Liu, H. 2010 “Recent progress in flapping wing aerodynamics and aeroelasticity”, *Prog. Aero. Sci.*,Vol. 46, pp. 284-327.

Soloff, S. M., Adrian, R. J., Liu, Z. C. 1997 “Distortion compensation for generalized stereoscopic particle image velocimetry”, *Measurement Science and Technology*, Vol. 8, pp. 1441-1454.

Taira, K. and Colonius, T. 2009a “Three-dimensional flows around low-aspect-ratio flat-plate wings at low Reynolds numbers”, *Journal of Fluid Mechanics*, Vol. 623, pp. 187-207.

Taira, K. and Colonius, T. 2009b “Effect of tip vortices in low-Reynolds number post stall flow control”, *AIAA Journal*, Vol. 47, pp. 749-756.

Trizila, P., Kang, C.-K., Aono, H., Shyy, W. and Visbal, M. 2011 “Low Reynolds aerodynamics of a flapping rigid flat plate”, *AIAA Journal*, Vol. 49, No. 4, pp. 806-823.

Visbal, M. 2010 “Numerical investigation of deep dynamic stall of a plunging airfoil”, *AIAA Paper*, 2010-4458.

Visbal, M. R. and Shang, J. S. 1989 “Investigation of the flow structure around a rapidly pitching airfoil”, *AIAA Journal*, Vol. 27, pp. 1044–1051.

Visbal, M. R. 2011 “Three-dimensional flow structure on a heaving low-aspect-ratio wing”, *AIAA Paper*, 2011-219.

Visbal, M., Gogineni, S. and Gaitonde, D. 1998 “Direct numerical simulation of a forced transitional plane wall jet”, *AIAA Paper*, 1998-2643.

Von Ellenrieder, K. D., Parker, K. and Soria, J. 2003 “Flow structures behind a heaving and pitching finite-span wing”, *Journal of Fluid Mechanics*, Vol. 490, pp. 129–138.

Wang, Z. J. 2005 “Dissecting insect flight”, *Annual Review of Fluid Mechanics*, Vol. 37, pp. 183-210.

Willert, C. 1997 “Stereoscopic digital particle image velocimetry for application in wind tunnel flows”, *Measurement Science and Technology*, Vol. 8, pp. 1465-1479.

Yilmaz, T. O. and Rockwell, D. 2009 “Three-dimensional flow structure on a maneuvering wing”, *Experiments in Fluids*, Vol. 48, pp. 539–544.

Yilmaz, T. O., Ol, M. and Rockwell, D. 2010 “Scaling of flow separation on a pitching low aspect ratio plate”, *Journal of Fluids and Structures*, Vol. 26, pp. 1034–1041.

Zang, W. and Prasad, A. K. 1997. “Performance evaluation of a Scheimpflug stereocamera for particele image velocimetry”, *Applied Optics*, Vol. 36, No. 33, pp. 8738-8744.

APPENDIX

SCALING OF FLOW SEPARATION ON A PITCHING LOW ASPECT RATIO PLATE

In the previous sections, the focus was the investigation and the characterization of the flow structure due to periodic pure plunging and linear pitch-up ramp motions. In addition to these motions, a wide range of dye visualization experiments was performed in order to reveal the formation and subsequent evolution of leading-edge vortices and related vortical structures for the other type of motions given in section 2.2.2 including linear plunge-up ramp, linear pitch-up - hold - return, and equivalent pitch and plunge motions. Moreover, the effects of wing geometry, Reynolds number, pitch-axis location, and ramp rate on the flow structure were investigated using dye visualization. The major results attained from these experiments are given in the following figures. Details of these results are given by Yilmaz et al. (2010).

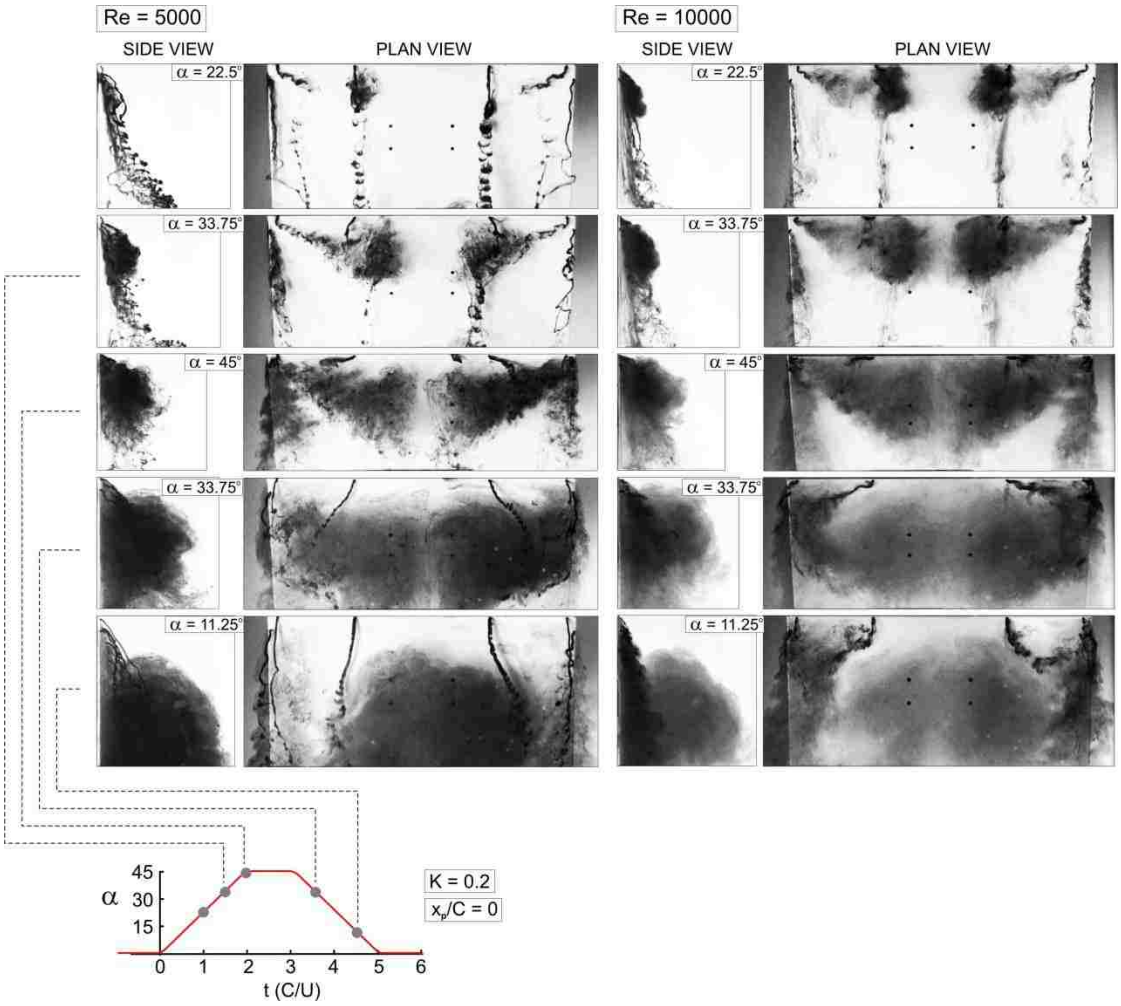

Figure A.1: Side and plan views of onset and development of vortex structure during pitch-up-hold-return motion at Re = 5,000 (left column), and Re = 10,000 (right column). Pitch point $x_p/C = 0$ and $K = 0.2$.

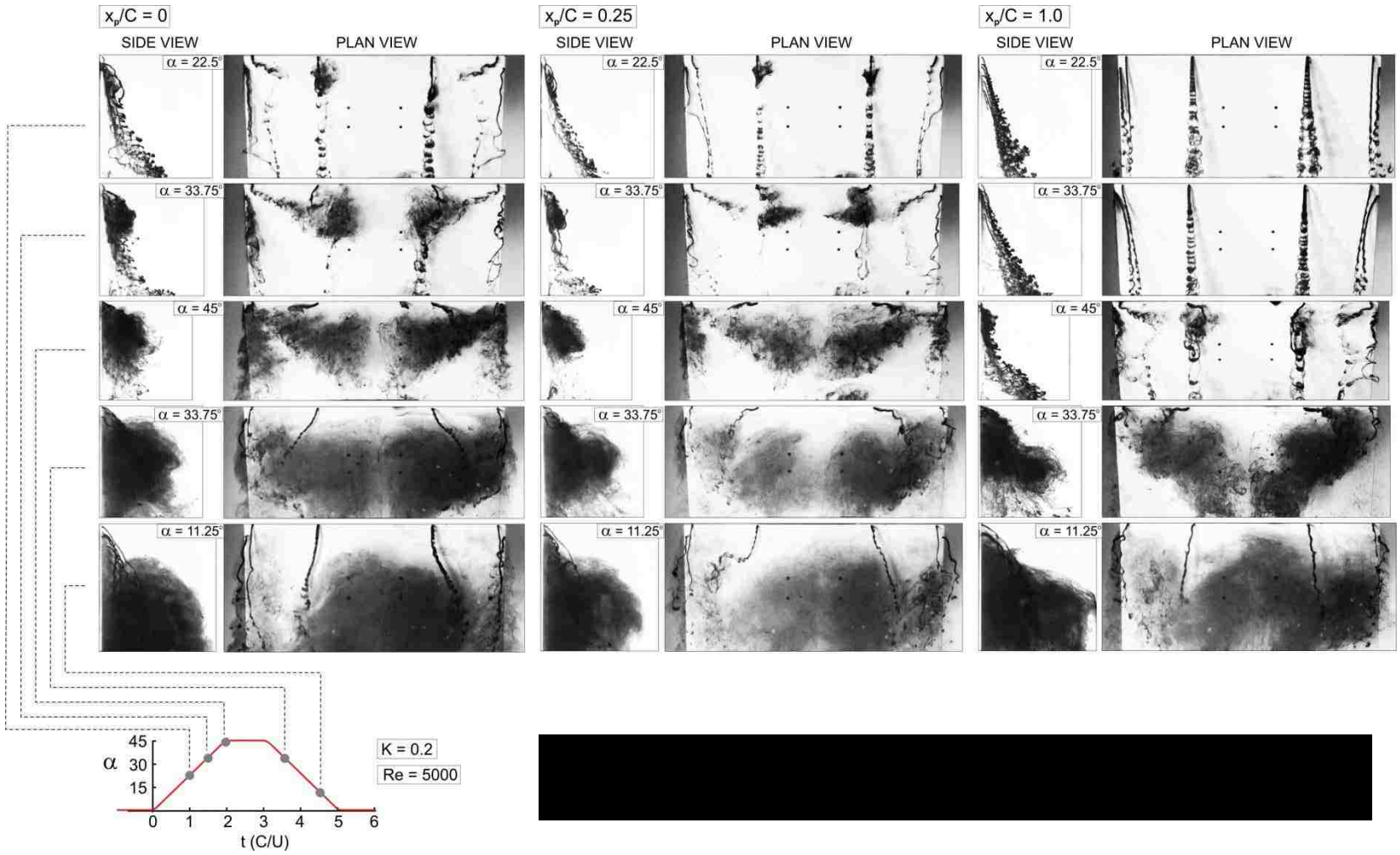
$x_p/C = 0$
$x_p/C = 0.25$
$x_p/C = 1.0$
SIDE VIEW
PLAN VIEW
α = 22.5°
α = 33.75°
α = 45°
α = 33.75°
α = 11.25°
45
30
15
α
0
1
2
3
4
5
6
t (C/U)
K = 0.2
Re = 5000

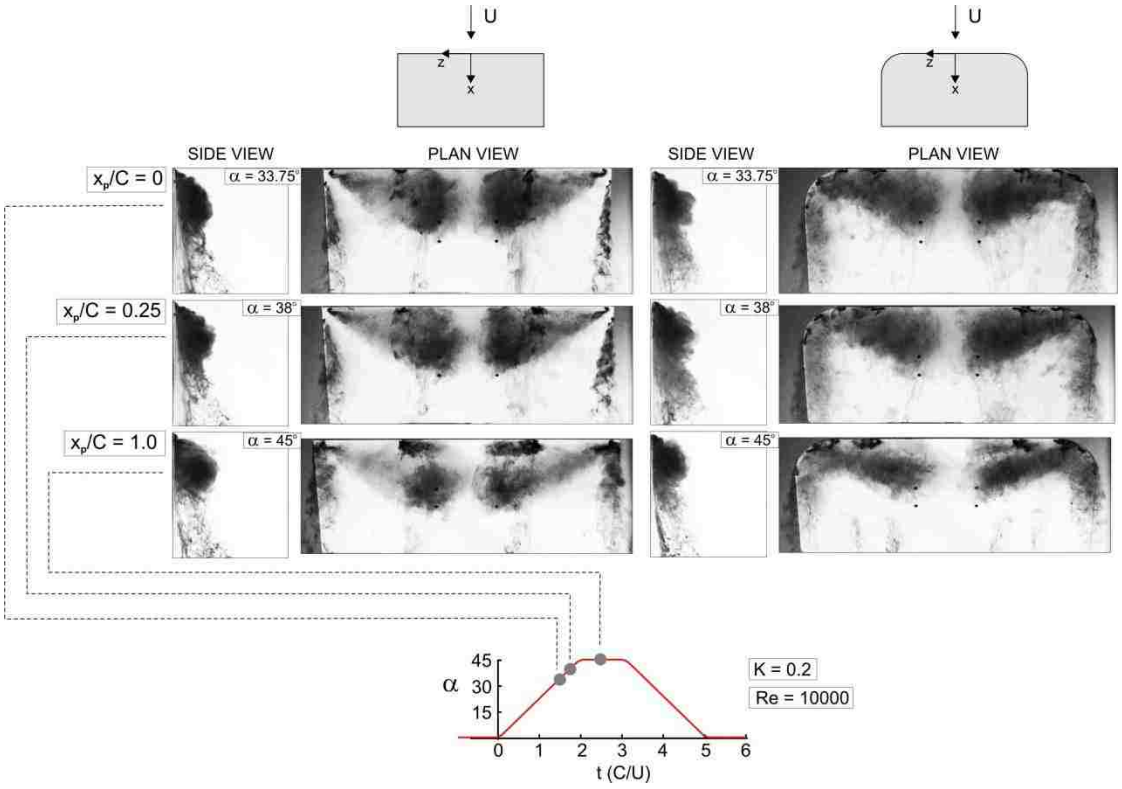

Figure A.3: Side and plan views of similar patterns of flow structure, observed for different values of pitch point; x_p/C = 0 (leading-edge), 0.25, and 1.0 (trailing-edge).

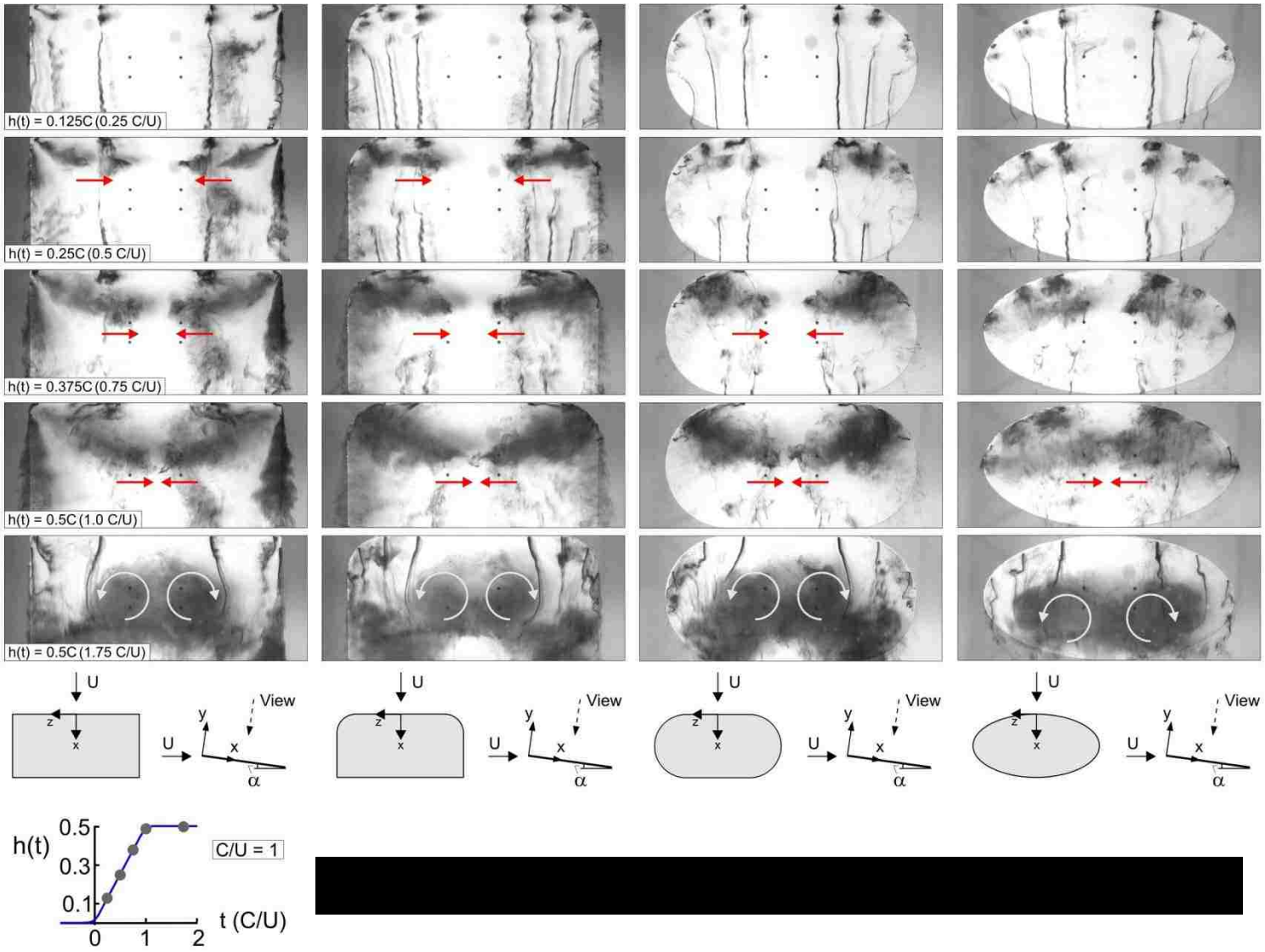
h(t) = 0.125C (0.25 C/U)
h(t) = 0.25C (0.5 C/U)
h(t) = 0.375C (0.75 C/U)
h(t) = 0.5C (1.0 C/U)
h(t) = 0.5C (1.75 C/U)
U
View
z
x
y
α
h(t)
0.5
0.3
0.1
0
1
2
t (C/U)
C/U = 1

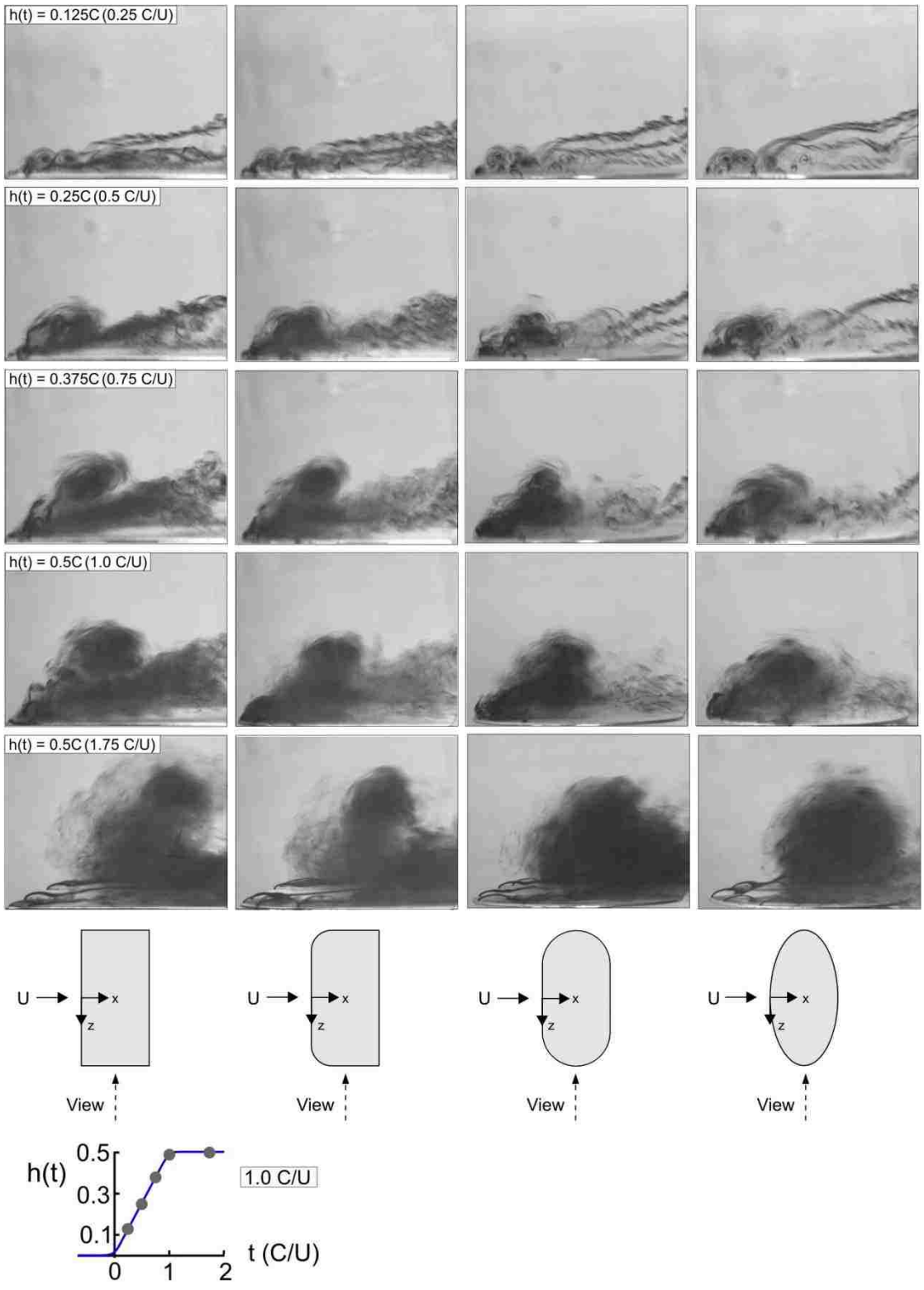

Figure A.5: Side views of onset and development of vortex structure during plunge-up ramp maneuver on various wing configurations at Re = 10,000.

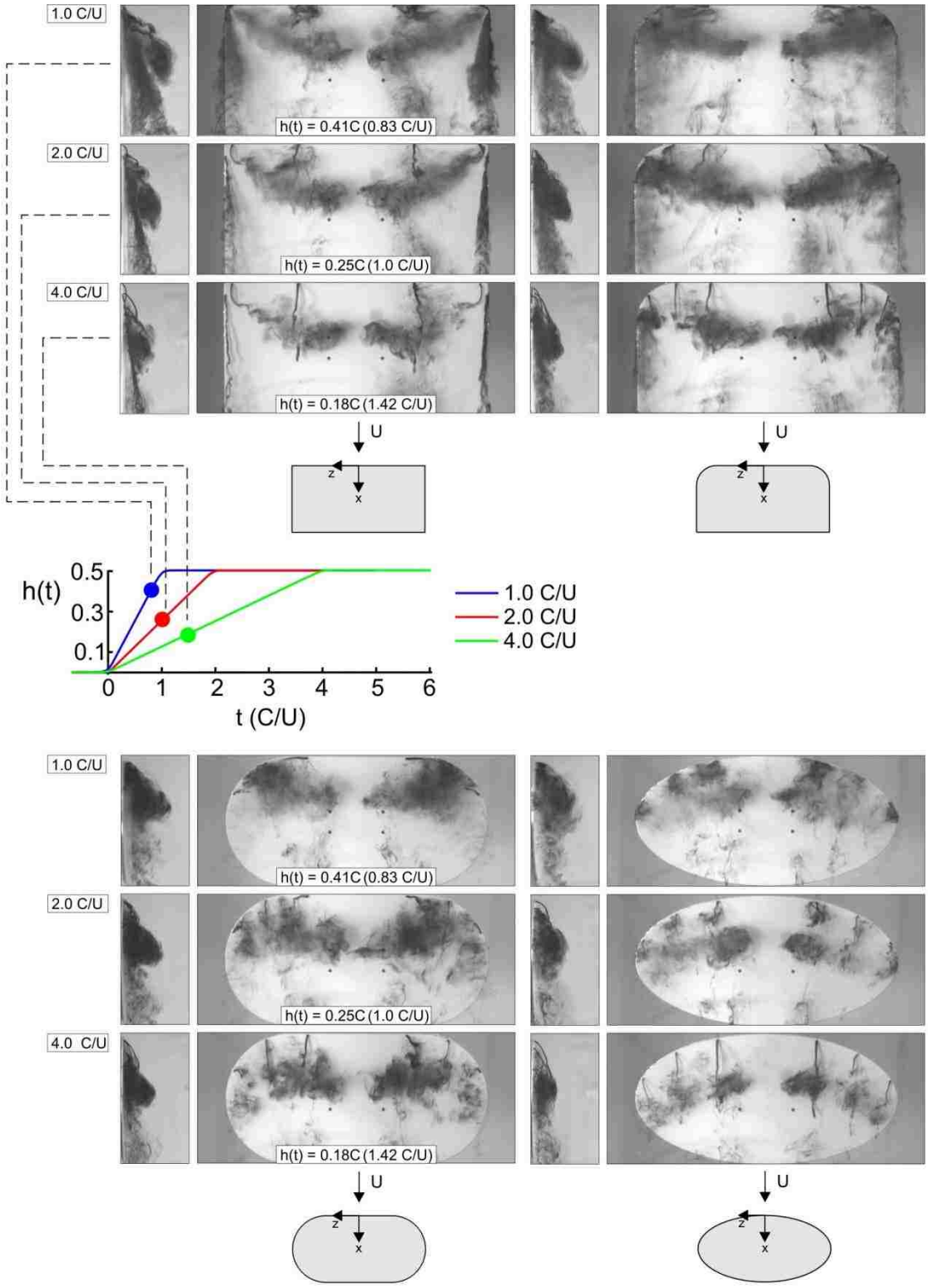

Figure A.6: Side and plan views of similar patterns of flow structure, observed on various wing configurations during plunge-up ramp maneuver at Re = 10,000.

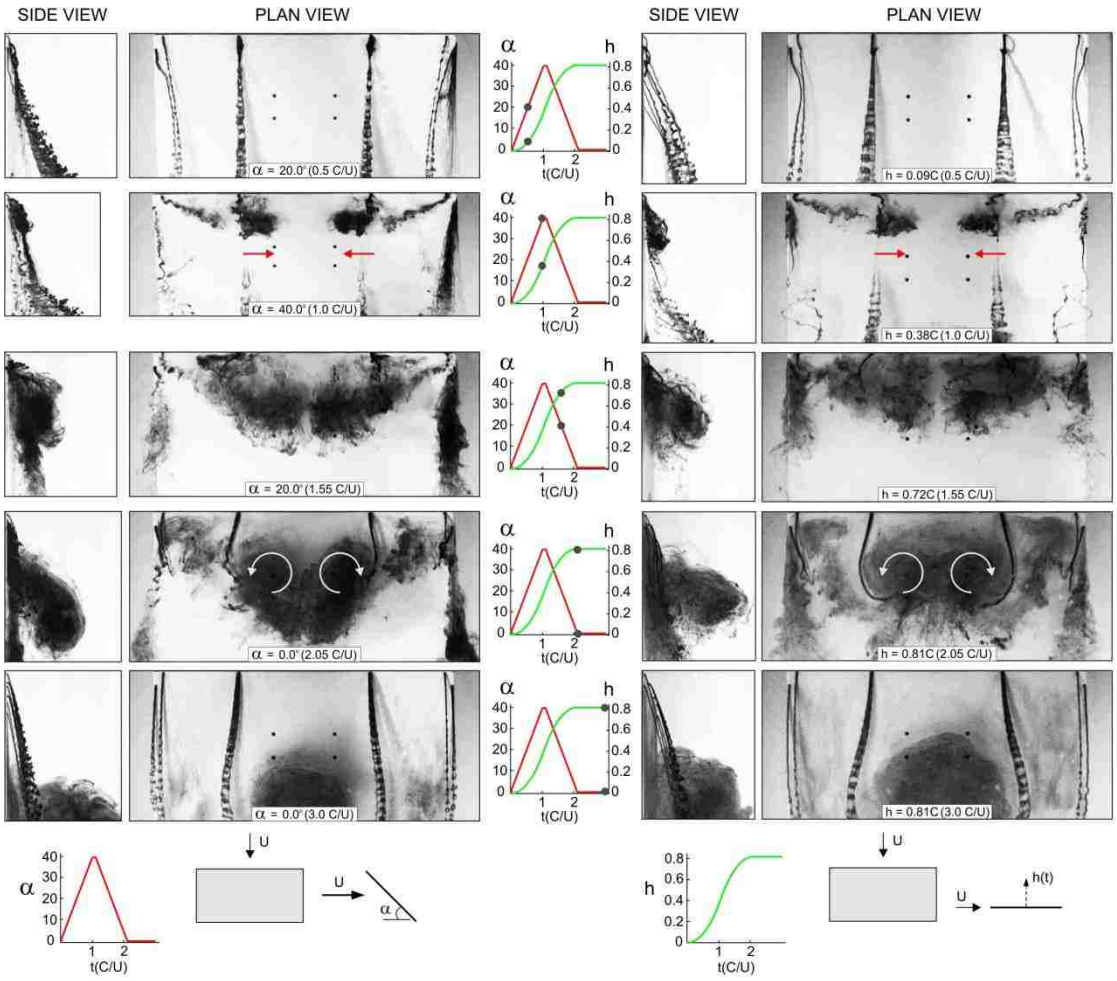

Figure A.7: Side and plan views of onset and development of vortex structure during pitch-up- pitch down motion (on the left), and "equivalent" plunge motion (on the right). Pitch point x_p/C = 0.25 and K = 0.35. Re = 5,000.

VITA

The author was born to Turan and Emine Yilmaz in Izmit, Turkey on March 02, 1980. He received his Bachelor of Science degree in both Mechanical Engineering and Physics from Koc University in May 2006. Then, he joined the Mechanical Engineering and Mechanics Department at Lehigh University. He received his Master of Science degree in Mechanical Engineering in January 2009. During his graduate study at Lehigh University, he worked under the supervision of Professor Donald Rockwell. He is currently enrolled in Ph.D. in Mechanical Engineering program in the P. C. Rossin College of Engineering at Lehigh University.